

# Modular Multilevel Converters with Embedded Storage: Simulation, Analysis, and Use for Frequency Support

by

Nuwan Madushanka Herath Herath Mudiyansele

A thesis submitted to the Faculty of Graduate Studies of

The University of Manitoba

in partial fulfilment of the requirements of the degree of

Doctor of Philosophy

Department of Electrical and Computer Engineering

University of Manitoba

Winnipeg, Canada

Copyright © 2022 Nuwan Madushanka Herath Herath Mudiyansele

# Abstract

Modular multilevel converters with embedded storage (MMC-ES) have attracted the attention of researchers as a flexible converter of integrating energy storage to ac and dc networks using a single converter. Conventional EMT simulation methods are highly inefficient in simulating MMC-ES due to the large number of switching elements in the converter. Detailed equivalent model (DEM) have been developed in previous research that could efficiently simulate the MMC-ES, but are ineffective in mathematically analysing the converter. This thesis proposes a novel averaged-value model (AVM) to the MMC-ES multivalve, which simulates the converter based on multivalve averaged quantities. The model is capable of conducting general EMT simulations, and analytically estimating circulating currents and capacitor voltage ripple. The AVM is validated against detailed EMT simulation results, mathematical analysis, and laboratory prototype observations. The thesis also improves the AVM and DEM to simulate converter's blocking state and validates the models against detailed simulation model. A novel MMC-ES HVDC link startup procedure is also developed and verified. Two case studies are conducted to study the use of MMC-ES in providing extensive ancillary services and it is concluded that MMC-ES supported by dedicated measurement communication lines and conventional fast frequency response controllers could greatly improve network frequency response.

# Copyright Forms

I would like to acknowledge the use of the following IEEE papers in preparation of this thesis.

Chapter 3 ©2021 IEEE. Reprinted, with permission, from N. Herath and S. Filizadeh, “Average-Value Model for a Modular Multilevel Converter With Embedded Storage,” in *IEEE Transactions on Energy Conversion*, June 2021.

Chapter 4 ©2022 IEEE. Reprinted, with permission, from N. Herath and S. Filizadeh, “Improved Average-Value and Detailed Equivalent Models for Modular Multilevel Converters with Embedded Storage,” in *IEEE Transactions on Energy Conversion*, Jan. 2022.

In reference to IEEE copyrighted material which is used with permission in this thesis, the IEEE does not endorse any of University of Manitoba’s products or services. Internal or personal use of this material is permitted. If interested in reprinting/republishing IEEE copyrighted material for advertising or promotional purposes or for creating new collective works for resale or redistribution, please go to [http://www.ieee.org/publications\\_standards/publications/rights/rights\\_link.html](http://www.ieee.org/publications_standards/publications/rights/rights_link.html) to learn how to obtain a License from RightsLink.

Section 5.1 “Increasing Dispatchability of a PV Power Plant through Modular Multilevel Converter-Based Embedded Battery Energy Storage (MMC-EBES)” reprinted with permission from CIGRE, Colloquium - Toronto 2020, ©2020.

# Acknowledgements

This thesis has become a reality with the support of many individuals and organizations. I would like to pay my sincere gratitude to all of them.

First and foremost, I would like to express my gratitude to my academic advisor, Prof. Shaahin Filizadeh for the continuous guidance, encouragement, and advice given throughout my research. I would also like to convey my gratitude to my industrial supervisor, Dr. Vajira Pathirana, for the valuable advice, suggestions and industry support and experience given for my research.

A special thank you must be conveyed to Mr. Shrimal Koruwage, Mr. Cory Smit, and Mr. Zoran Trajkoski, for helping me with technical details in developing the MMC-ES prototype.

Special thanks go to the University of Manitoba Graduate Fellowship (UMGF), HATCH, MITACS, and NSERC for providing financial support to carry out my research.

Finally, I would like to thank my family, my colleagues at the University of Manitoba, and friends who were there to support me in numerous ways throughout my research.

# Dedications

*To my loving parents and sisters.*

# Table of Contents

Abstract . . . . .	ii
Copyright Forms . . . . .	iii
Acknowledgements . . . . .	iv
Dedications . . . . .	v
List of Figures . . . . .	xi
List of Tables . . . . .	xv
<b>1 Introduction</b>	<b>1</b>
1.1 Background and Motivation . . . . .	1
1.2 Problem Definition and Conventional Solutions . . . . .	3
1.3 Research Objectives and Contributions . . . . .	4
1.3.1 Objectives . . . . .	4
1.3.2 Contributions . . . . .	5
1.4 List of Publications . . . . .	6
1.5 Thesis Outline . . . . .	6
<b>2 Overview and Application of the MMC-ES</b>	<b>8</b>
2.1 Overview and Operation of MMC-ES . . . . .	9

2.1.1	Construction of the Converter . . . . .	10
2.1.2	Operation of the Converter . . . . .	14
2.1.3	SM DC-DC Converter . . . . .	17
2.2	Control Systems of MMC-ES . . . . .	17
2.2.1	AC Current Control . . . . .	18
2.2.2	Negative Sequence Control . . . . .	21
2.2.3	Circulating Current Control . . . . .	22
2.2.4	DC-DC Converter Control . . . . .	25
2.2.5	State-of-Charge (SOC) Balancing Control . . . . .	26
2.3	MMC-ES Modeling Techniques . . . . .	27
2.3.1	Detailed IGBT-Diode Based Model . . . . .	28
2.3.2	Detailed EMT Model . . . . .	29
2.3.3	Detailed Equivalent EMT model . . . . .	31
2.3.4	Switching Function-Based AVM . . . . .	31
2.3.5	Converter-Level AVM . . . . .	34
2.4	Use of MMCs with Energy Storage in Frequency Support . . . . .	35
2.4.1	Wind Power . . . . .	36
2.4.2	Solar PV Power . . . . .	37
2.4.3	Control Systems Associated with Providing Frequency Support . . . . .	39
2.5	Summary . . . . .	42
<b>3</b>	<b>Analysis of the Converter with an Averaged-Value Model</b>	<b>43</b>
3.1	Averaged-Value Model . . . . .	45
3.1.1	Averaged-Value Model of the DC-DC Converter . . . . .	45
3.1.2	SM Capacitor Voltage Ripple . . . . .	47

3.1.3	EMT-Type Averaged-Value Model . . . . .	49
3.2	Analysis of Circulating Currents and Capacitor Voltage Ripple . . . . .	50
3.2.1	Circulating Currents in MMC-ES . . . . .	51
3.2.2	Second Harmonic Circulating Current . . . . .	53
3.2.3	Circulating Current Suppression Control (CCSC) . . . . .	56
3.3	Evaluation of the Averaged-Value Model . . . . .	57
3.3.1	Evaluation against Detailed EMT Simulation Models . . . . .	57
3.3.2	Evaluation of Behaviour under AC System faults . . . . .	62
3.3.3	Verification against Experimental Results . . . . .	63
3.3.4	Limitations of the AVM . . . . .	64
3.4	Modelling and Balancing SOC . . . . .	66
3.5	Selection of Converter Parameters . . . . .	68
3.6	Summary . . . . .	72
<b>4</b>	<b>Improvements on EMT Simulation Models of MMC-ES</b>	<b>73</b>
4.1	Introduction . . . . .	73
4.2	Control Systems Associated with MMC-ES . . . . .	76
4.2.1	Basic Control Systems . . . . .	76
4.2.2	Startup Sequence for MMC-ES DC Transmission System . . . . .	76
4.2.3	Control Objectives of MMC-ES in an HVDC System . . . . .	78
4.3	Development of Blocking-Enabled DEM and AVM Models . . . . .	78
4.3.1	Switching States of a MMC-ES Multivalve . . . . .	79
4.3.2	Developing Computationally Efficient EMT Models . . . . .	81
4.3.3	Inclusion of the Blocked State in DEM and AVM . . . . .	82
4.3.4	Numerical Chatter Elimination in Upgraded Models . . . . .	85



4.4	Simulation Validation . . . . .	88
4.4.1	Description of the Test System . . . . .	88
4.4.2	Power Set Point Change . . . . .	89
4.4.3	AC Three-phase Fault . . . . .	90
4.4.4	DC Line-to-Ground Fault . . . . .	92
4.4.5	DC Line-to-Line Fault . . . . .	93
4.4.6	Startup Sequence . . . . .	97
4.4.7	Impact of Simulation Time-Step . . . . .	97
4.4.8	Computational Efficiency . . . . .	98
4.5	Summary . . . . .	100
<b>5</b>	<b>Frequency Support and other Ancillary Services Using MMC-ES</b>	<b>102</b>
5.1	Case Study 1: Increas. Dispatch. of a PV Power Plant . . . . .	102
5.1.1	Introduction . . . . .	102
5.1.2	PV Plant Power Smoothing with Moving Average Window . . . . .	104
5.1.3	Verification of Controller . . . . .	105
5.1.4	Summary of Case Study 1 . . . . .	109
5.2	Case Study 2: Use of MMC-ES in HVDC Bi-pole . . . . .	110
5.2.1	Solar PV Plant . . . . .	110
5.2.2	DC System . . . . .	117
5.2.3	MMC-ES Ancillary Services Control System . . . . .	119
5.2.4	MMC-ES Protection System . . . . .	119
5.2.5	Simulation Experiments . . . . .	122
5.2.6	Summary on Case Study 2 . . . . .	131
5.3	Summary . . . . .	132

<b>6 Contributions, Conclusions, and Future work</b>	<b>133</b>
6.1 Contributions and Conclusions . . . . .	133
6.2 Recommendations for Future Work . . . . .	136
<b>References</b>	<b>138</b>

# List of Figures

2.1	Schematic diagram of an MMC-ES . . . . .	10
2.2	Construction of an MMC-ES SM . . . . .	11
2.3	DC fault current conduction paths of an MMC . . . . .	13
2.4	Average schematic diagram of an MMC. . . . .	14
2.5	A single phase MMC-ES connected to an ac network. . . . .	18
2.6	AC current controller . . . . .	20
2.7	Block diagram of a closed loop system . . . . .	21
2.8	Negative-sequence current controller. . . . .	23
2.9	Frequency response of a resonance controller. . . . .	24
2.10	Block diagram of dc circulating current control and dc power control. . . . .	25
2.11	Unified controller for bi-directional dc-dc converter. . . . .	26
2.12	SOC balancing controllers. . . . .	28
2.13	Regular MMC . . . . .	29
2.14	Nonlinear characteristics of semiconductors. . . . .	30
2.15	Representing an IGBT in an EMT environment. . . . .	30
2.16	Development of the DEM for regular MMC . . . . .	32
2.17	Switching function-based AVM . . . . .	33

2.18 Converter-level AVM . . . . .	35
2.19 System frequency and response following a generation loss. . . . .	40
2.20 Derivative power controller . . . . .	41
2.21 Droop power controller . . . . .	41
3.1 MMC-ES and used SM schematic. . . . .	44
3.2 States of the dc-dc converter . . . . .	45
3.3 Averaged-value model of a multi-valve embedded in an EMT environment. . . . .	50
3.4 Power flow within the MMC-ES . . . . .	59
3.5 AC current from the converter. . . . .	59
3.6 AC voltage at converter terminal. . . . .	59
3.7 Phase-a, upper arm current. . . . .	60
3.8 Average capacitor voltage of phase-a, upper arm. . . . .	60
3.9 Average battery current of phase-a, upper arm. . . . .	60
3.10 AC-side rms voltage. . . . .	61
3.11 Effect of simulation time step for AVM . . . . .	61
3.12 AC current waveform during remote fault test. . . . .	62
3.13 Average capacitor voltage during remote fault test. . . . .	63
3.14 Average battery current during remote fault test. . . . .	63
3.15 Prototype setup. . . . .	65
3.16 Capacitor voltage ripple . . . . .	65
3.17 Capacitor voltage ripple variations with different parameters . . . . .	66
3.18 Block diagram for battery voltage evaluation. . . . .	67
3.19 SOC balancing controller. . . . .	68
3.20 Variation of converter SOC. . . . .	68

3.21	Capacitor voltage ripple . . . . .	69
3.22	Second-order circulating current . . . . .	70
3.23	Variation of capacitor voltage ripple versus . . . . .	71
4.1	Startup sequence for MMC-ES HVDC link. . . . .	77
4.2	Arm current conduction paths in MMC-ES . . . . .	80
4.3	Development of DEM . . . . .	82
4.4	Overview of AVM. . . . .	83
4.5	Upgraded DEM model to simulate blocking. . . . .	84
4.6	Upgrade to the AVM modulation scheme to simulate blocked state . . . . .	85
4.7	Upgraded AVM model to simulate blocking. . . . .	86
4.8	Mechanisms of interpolation to avoid numerical chatter. . . . .	87
4.9	Schematic diagram of the test system. . . . .	89
4.10	Responses to power set-point changes at inverter and rectifier end. . . . .	91
4.11	Power distribution within the two converters. . . . .	93
4.12	AC three phase fault at inverter's PCC. . . . .	94
4.13	Response to a dc line-to-ground fault . . . . .	95
4.14	Response to a dc line-to-line fault . . . . .	96
4.15	MMC-ES during startup. . . . .	99
4.16	Effect of simulation time-step. . . . .	100
5.1	Power smoothing controller. . . . .	105
5.2	Schematic diagram of the studied system. . . . .	106
5.3	Considered irradiance profile - Case study 1. . . . .	108
5.4	Power distribution in MMC-ES - Case study 1 . . . . .	108

5.5	Frequency under different control systems - Case study 1. . . . .	109
5.6	Schematic diagram of studied HVDC with MMC-ES system . . . . .	111
5.7	Schematic diagram of the PV plant. . . . .	114
5.8	PV inverter controller and synchronizer - Case Study 2. . . . .	115
5.9	Simulation results of PV inverter synchronizing - Case Study 2 . . . . .	116
5.10	Ancillary support controllers - Case Study 2 . . . . .	120
5.11	LVRT guideline developed by FERC. . . . .	121
5.12	Response of the system to a fault on the ac transmission line followed by line tripping - Case Study 2. . . . .	124
5.13	Rectifier end active and reactive power variation following the loss of generation - Case Study 2. . . . .	125
5.14	Power set point calculators with the communication link . . . . .	125
5.15	Comparison of simulation data with and without a communication line - Case Study 2. . . . .	127
5.16	MMC-ES power distribution with and without a communication line - Case Study 2. . . . .	128
5.17	Power distribution in busses in rectifier end - Case Study 2. . . . .	128
5.18	System response to a irradiance profile - Case Study 2 . . . . .	129

# List of Tables

3.1	Parameters of the simulated MMC-ES . . . . .	57
3.2	Parameters of the MMC-ES prototype . . . . .	64
4.1	Simulated System Data . . . . .	90
4.2	Power set point change with time . . . . .	92
4.3	Startup sequence timing parameters . . . . .	98
4.4	Simulation time for different models . . . . .	101
5.1	System parameters - Case study 1. . . . .	106
5.2	System parameters - Case study 2. . . . .	112
5.3	Control objectives of different parameters of MMC-ES. . . . .	117
5.4	XLPE cable parameters. . . . .	118

# Chapter 1

## Introduction

### 1.1 Background and Motivation

Renewables have become a popular source of energy in the modern power system. Freely available energy resources, government incentives, and the decreasing price of associated technologies have helped to promote renewables in the energy market. Solar PV, solar thermal, wind, geothermal, and tidal power are key renewable energy sources, while solar PV and wind have won the spotlight [1] due to their global availability; they are becoming increasingly more affordable to integrate into the power system.

Although renewable energy sources are attractive, they present unique problems as well. Their power outputs are highly variable in solar PV and wind applications, as they vary depending on solar irradiance and wind speed, respectively. Additionally, they are interfaced to the power system via power electronic converters, which do not introduce any spinning mass into the power system. This reduces the overall system's inertia and causes the system frequency to experience large fluctuations [2]. Solutions have been proposed to integrate



energy storage into the power system to remedy these issues. Storage methods such as pumped hydro plants, hydrogen fuel cells, compressed air energy, flywheels, and batteries have caught the attention of many engineers and researchers [3,4]. The type of energy storage varies with the application, usage, cost, and many other factors. However, battery energy storage systems have been popular as a means of providing high amounts of power rapidly with a potential to store considerable amounts of energy [5].

The dc power available in the batteries needs to be inverted to ac before connecting to the power system. The basic method to do so has been to incorporate a two-stage converter topology where a dc-dc converter and a two-level or three-level inverter interface the battery to the power system [6]. This topology provides a simple solution, but is quite poor in harmonic performance and redundancy, and is often to be implemented in considerably low voltages. As an alternative solution, modular multilevel converters with embedded storage (MMC-ES) are introduced. The MMC-ES allows to distribute battery units among its submodules (SMs) while producing low-harmonic ac high voltages at the output. High controllability over each battery unit is also achieved with the use of MMC-ES. An added advantage of providing power to both ac and dc grids is also available with the use of this converter.

Due to these advantages, the MMC-ES can be considered a highly attractive converter to interface battery energy storage to the power system. Specialized tools are required to study and analyze such converter's behaviour. Use of energy storage for frequency support is also a key application of the MMC-ES, which has attracted the attention of researchers.

## 1.2 Problem Definition and Conventional Solutions

Modular Multilevel Converter topology provides high controllability to the user in the sense of controlling dc power, ac power and individual submodule voltages. MMC-ES topology allows the individual control of battery units to be distributed throughout the converter. However, to achieve these goals, the converter is constructed using a large number of power electronic switches (IGBTs and diodes) and passive elements (inductors and capacitors), of which a detailed overview is given in section 2.1. The large number of components in an MMC-ES easily exhaust conventional converter simulation techniques that are used to study the operation of such converters. Thus it is essential to develop new simulation models for accurate and computationally efficient simulation of MMC-ES converters. These models should be able to accurately simulate all operating conditions that this type of converter experiences including converter blocking and operating during ac and dc faults.

Converter models are also required for analyzing the converter in an averaged sense to study converter parameters and internal currents. This thesis concentrates on using averaged value models to analyze converter currents and design converter parameters.

Energy storage in the power system has become an attractive solution for providing frequency support and energy support in grids with high renewable penetration. Highly efficient converters are actively sought by engineers and researchers. MMC-ES, being an efficient converter with flexible power management, has caught the attention of engineers for providing power for frequency support objectives. The ability of the MMC-ES to operate when connected to an HVDC scheme also allows to explore the usage of energy storage within HVDC schemes.

## 1.3 Research Objectives and Contributions

### 1.3.1 Objectives

The objectives of this research are as follows:

- **To develop MMC-ES models to study and analyze the converter under steady state, and design converter parameters.** Suitable mathematical models are required to analyze the behaviour of the converter. This allows to determine different converter variables such as SM capacitor voltage ripple, circulating current magnitudes, etc. The analysis allows to design converters with suitable converter parameters (arm inductance, SM capacitance) without conducting time-consuming computer simulations.
- **To develop efficient EMT simulation models to study high frequency transients and control systems concerning MMC-ES.** Analytical models are not adequate for the studies of high-frequency transients. Highly efficient, accurate EMT simulation models are required to study the full operation of the converter with regards to controller design and response to faults.
- **To use the developed EMT models to study the applicability of MMC-ES in providing ancillary services to power systems with high renewable integration.** A key envisioned use of MMC-ES is to provide ancillary services to the power system using its embedded storage. Unavailability of efficient, highly detailed EMT simulation models has created a gap in studying the ancillary services provided by MMC-ES with high penetration of renewable generation. This thesis provides novel control structures for MMC-ES for providing ancillary support to systems with high

renewable penetration levels.

### 1.3.2 Contributions

- **Developed an averaged value model (AVM) for the MMC-ES multivalve to be used with converter analysis and EMT simulations.** This is a multi-valve level averaged value model for the MMC-ES multivalve, which can be effectively used for MMC-ES simulation under steady state and to design control systems. The model allows estimation of the circulating currents and retains average quantities of multivalves.
- **Developed a single phase MMC-ES prototype and validated the AVM.** A low power single-phase MMC-ES was developed and was used to validate the AVM and the analytical equations in verifying the capacitor voltage ripple.
- **Enhanced the AVM and detailed equivalent model (DEM) in EMT environment to simulate MMC-ES converter blocking and accurately simulate dc faults.** The original AVM and DEM developed for MMC-ES lack the ability to simulate converter blocking and dc faults. An improvement to these models are presented here to resolve this problem.
- **Developed MMC-ES converter HVDC link startup sequence to start the converter with minimum inrush currents.** MMC-ES is a highly capacitive converter and a startup sequence is required to smoothly start the converter avoiding any destructive inrush currents. The thesis presents a startup sequence for a bipole system formed with two MMC-ES that allows gradual startup of the converters.

- **Used the MMC-ES topology in high renewable-penetrated systems to provide ancillary services such as fast frequency response, power output smoothing, etc.** The developed models are used in studying the ability of the MMC-ES in providing ancillary services.

## 1.4 List of Publications

1. **N. Herath** and S. Filizadeh, “Improved Average-Value and Detailed Equivalent Models for Modular Multilevel Converters with Embedded Storage,” in IEEE Transactions on Energy Conversion, 2022 (Early Access)
2. **N. Herath** and S. Filizadeh, “Average-Value Model for a Modular Multilevel Converter with Embedded Storage,” in IEEE Transactions on Energy Conversion, vol. 36, no. 2, pp. 789-799, June 2021, doi: 10.1109/TEC.2020.3014793.
3. **N. Herath**, V. Pathirana and S. Filizadeh, “Increasing Dispatchability of a PV Power Plant through Modular Multilevel Converter-Based Embedded Battery Energy Storage (MMC-EBES),” presented at CIGRE Canada Conference 2020, Toronto, Canada, 2020.

## 1.5 Thesis Outline

This thesis is divided into six chapters as described below:

**Chapter 1:** Includes background information, problem definition and existing solutions, motivation, objectives, and contributions.

**Chapter 2:** Provides a detailed overview on the MMC-ES, its controls and operation, previous modeling techniques used by the researchers and a study on the usage of energy

storage in power systems to provide ancillary services.

**Chapter 3:** Conducts an analysis of the MMC-ES by developing an averaged value model (AVM). This model is capable of conducting steady state and low frequency EMT simulations of the converter.

**Chapter 4:** Enhances the AVM and DEM to simulate blocking of the converter and equips the model to accurately simulate dc faults in the EMT environment. Detailed comparisons of simulation models are presented.

**Chapter 5:** Presents control techniques to be adapted by energy storage systems in providing ancillary services to the power system. The applicability of these methods are studied using two case studies conducted in PSCAD.

**Chapter 6:** Presents the conclusions drawn from the results of this thesis, and suggests topics for further research.

## Chapter 2

# Preliminary Overview and State-of-the-Art of the Operation and Applications of MMC-ES

The MMC-ES has become a popular technology in the research community as a means of integrating energy storage. Its large number of degrees of freedom allows the converter to be flexibly operated to interface with an ac network and a dc network while integrating energy storage into the mix. To fully understand the operation of the converter, it is essential to have a thorough knowledge of the topology, operating principles, and control of the converter. This chapter provides a detailed description of these topics based on existing literature so that the reader has a clear understanding. As a prologue to the simulation models developed in Chapters 3 and 4, current simulation models developed for conventional MMC are discussed as well. Finally the chapter provides an account on the use of energy storage in providing ancillary services to the power system with renewable generation, with particular attention

to the applications with MMC-ES.

## 2.1 Overview and Operation of MMC-ES

The line commutated converter (LCC) built with thyristors was the converter of choice for many HVDC projects [7]. The LCC is highly efficient due to the line-frequency switching, but has disadvantages such as [8]:

- large reactive power requirements;
- poor harmonic performance, requiring large and expensive filters; and
- difficulty to use in multi-terminal configurations.

Voltage Source Converters (VSC) are capable of overcoming these issues thanks to their inherent characteristics. However, conventional two-level and three-level VSC schemes cannot be used in most HVDC applications due to the high voltage stress observed by IGBTs, heavy filtering requirements and the high power losses caused by high switching frequencies. Modular Multilevel Converter (MMC) [9] topologies have been developed as a solution to fulfill the requirements of a VSC in HVDC applications. The converter distributes the dc link voltage over a large number of capacitors and creates the output ac voltage by inserting and bypassing the capacitors. A switching arrangement made with IGBTs and diodes is placed for each capacitor to insert or bypass the capacitor. This arrangement reduces the voltage stress observed by each IGBT and allows to create an output voltage with low harmonics. The MMC-ES employs the same converter topology, but also includes an energy storage (ES) module (battery, supercapacitor, superconducting magnet, etc) via a filter.



### 2.1.1 Construction of the Converter

Figure 2.1 shows the schematic diagram of a general MMC-ES.

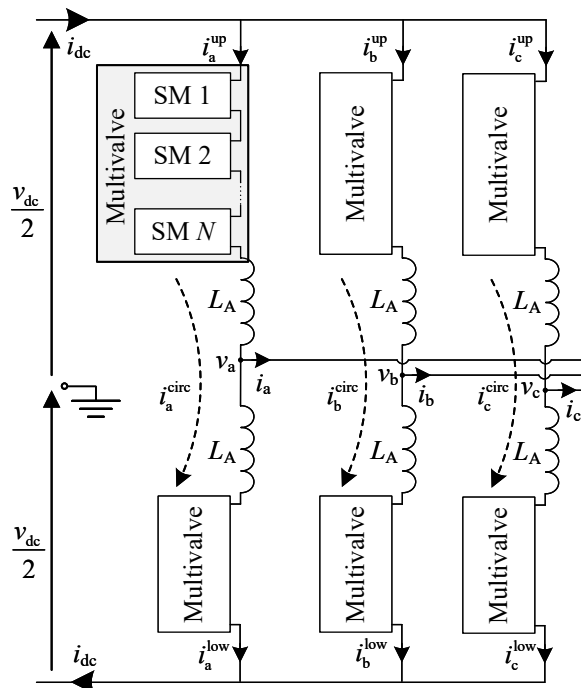


**Figure 2.1:** Schematic diagram of an MMC-ES

The converter's dc link voltage is  $v_{dc}$ , and its ac voltage output and current are  $v_x$  and  $i_x$   $x \in \{a, b, c\}$ , respectively. Upper arm and lower arm currents are  $i_x^{up}$  and  $i_x^{low}$ , respectively.  $L_A$  is the arm inductance. Due to mismatches between the dc link and SM capacitor voltages, circulating currents are generated inside the MMC-ES and they are denoted as  $i_x^{circ}$ . The multivalve is a series connection of SMs; typical SM schematics are shown in Figure 2.2.

The energy storage element of the SM can be selected as required. Researchers have used batteries [10,11], supercapacitors [12], and superconductor magnets [13,14] as energy storage elements to provide active power ancillary services. Batteries [15] and supercapacitors [16]

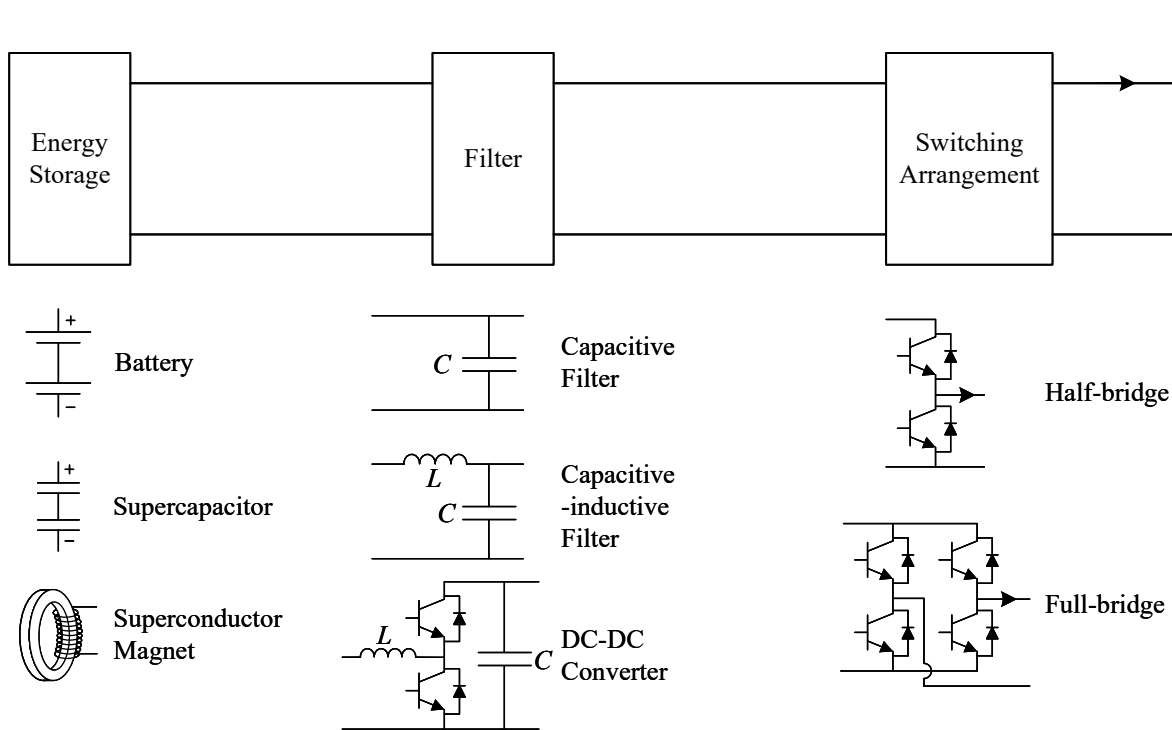


**Figure 2.2:** Construction of an MMC-ES SM

have been actively used in research along with MMC-ES topologies. Apart from energy storage, energy generation integration to MMC-ES SM has been also researched by connecting solar PV panels to the MMC-ES SM [17]. Different energy storage elements can be used in a single MMC-ES [18] thus enabling the use of different qualities available in each energy storage element (e.g., high energy output of batteries and high power handling capability of supercapacitors).

A filter is generally used between the energy storage/generation element and the switching arrangement of the SM in an MMC-ES. The filter could be built by a simple capacitor ( $C$ ), an inductor-capacitor ( $LC$ ) arrangement, or an active filter, which is a bi-directional dc-dc converter. The capacitor in the filter in Figure 2.2 acts as the SM capacitor, which holds a fraction of the dc link voltage of the MMC. The passive filters are quite inexpen-

sive, highly efficient, and simple to use, but cannot offer high controllability over the energy storage element current as given by a dc-dc converter. The dc-dc converter could be further upgraded to provide galvanic isolation between the energy storage element and the MMC using high frequency transformers albeit with added losses to the converter.

The switching arrangement in the SM inserts/bypasses the SM capacitor from the rest of the multivalve. The SM's output voltage can be either 0 or  $+v_C$  for half-bridge SMs and 0,  $+v_C$ , and  $-v_C$  for full-bridge SMs. During converter startup and fault conditions, the converter may be blocked (firing pulses set to low on all IGBTs). Both SM topologies can stop the converter during an ac fault by blocking the converter, but half-bridge SMs are not capable of handling dc-faults. Full-bridge SMs are capable to do so. Figure 2.3 shows the current conduction path during a dc fault.

As mentioned above, different SMs with energy storage could be developed for use with MMC-ES. Hybrid MMC-ES with half-bridge and full-bridge SMs could be used in a multivalve to achieve dc fault blocking capabilities with reduced losses by reducing the number of full-bridge SMs [19]. SMs with battery storage could be used along with SMs with supercapacitors to employ both high energy density of batteries and high power density of supercapacitors from a single converter [18]. In cases where continuous charging and discharging is required as for absorbing highly variable power variations, use of supercapacitors as energy storage is desired and battery storage is desired at instances with large scale energy support. Studies have been conducted to integrate PV power and battery storage in a single multivalve with a fraction of the SMs being connected to PV source while others are connected to batteries [17]. These converters are capable of reducing the power fluctuations of PV panels inherently, although the practical usage of such converters is yet to be seen. In this thesis, MMC-ES constructed with SMs using batteries as energy storage element, dc-dc

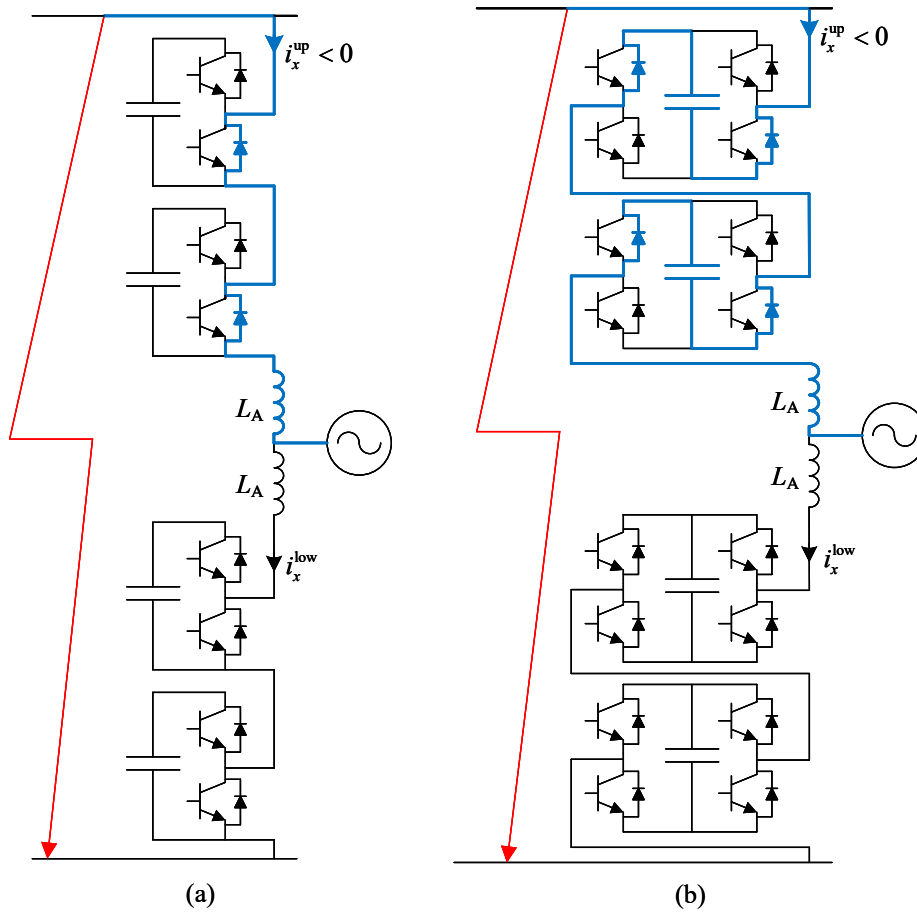


**Figure 2.3:** DC fault current conduction paths of an MMC with (a) half-bridge SMs, and (b) full-bridge SMs

converter as a filter, and a half-bridge switching arrangement is considered.

Although MMC-ES has been able to attract the attention of researchers and engineers, no large scale utility implementations have been completed yet. The work done in [20] has implemented a utility scale cascaded converter, which is a subclass of the MMC-ES converter. However, there are a number of experimental prototypes developed in laboratories [21, 22].

### 2.1.2 Operation of the Converter

Figure 2.4 shows a simplified diagram of an MMC-ES for phase  $x$  ( $x = a, b, c$ ). Suppose that the MMC-ES has  $N$  SMs per multivalve.

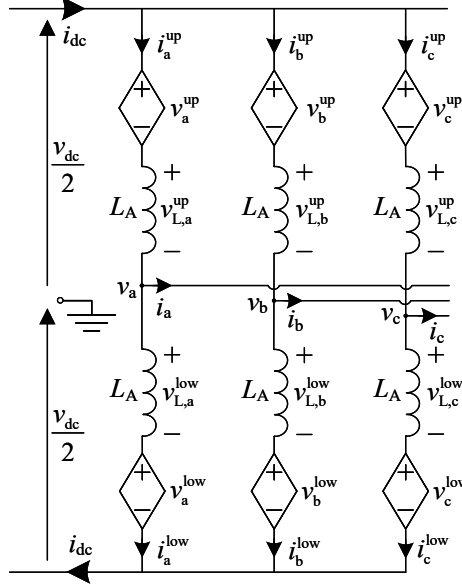


**Figure 2.4:** Average schematic diagram of an MMC.

Kirchhoff's voltage law can be applied to the MMC as follows for phase  $x$

$$\frac{v_{dc}}{2} - v_x^{up} - L_A \frac{di_x^{up}}{dt} = v_x \quad (2.1a)$$

$$-\frac{v_{dc}}{2} + v_x^{low} + L_A \frac{di_x^{low}}{dt} = v_x \quad (2.1b)$$

By adding and subtracting these two equations, one obtains:

$$\frac{L_A}{2} \frac{di_x}{dt} = \frac{-v_x^{up} + v_x^{low}}{2} - v_x \quad (2.2a)$$

$$L_A \frac{di_x^{\text{circ}}}{dt} = \frac{v_{\text{dc}}}{2} - \frac{v_x^{\text{up}} + v_x^{\text{low}}}{2} \quad (2.2b)$$

where

$$i_x = i_x^{\text{up}} - i_x^{\text{low}} \quad (2.3a)$$

$$i_x^{\text{circ}} = \frac{i_x^{\text{up}} + i_x^{\text{low}}}{2} \quad (2.3b)$$

$$v_x = \frac{-v_x^{\text{up}} + v_x^{\text{low}}}{2} \quad (2.3c)$$

$$v_x^{\text{comm}} = \frac{v_x^{\text{up}} + v_x^{\text{low}}}{2} \quad (2.3d)$$

The expression (2.2a) describes the dynamics of the ac line current and (2.2b) describes the dynamics of circulating currents in the converter. It can be observed that half the arm inductor participates in the power transfer. Circulating currents are developed due to the instantaneous mismatch between SM capacitor voltages against the dc link and manifest as part of the voltage ripple in the SM capacitors. From these expressions it is clear that the maximum voltage of the ac output is obtained when all the SMs in the lower arm are inserted and all SMs in upper arm are bypassed. Similarly the minimum ac output is obtained when all the SMs in lower arm are bypassed and all SMs in upper arm are inserted. Hence the maximum and minimum ac voltage outputs are

$$v_x^{\text{max}} = \frac{\sum v_{\text{cap},x}^{\text{low}}}{2} \quad (2.4a)$$

$$v_x^{\text{min}} = -\frac{\sum v_{\text{cap},x}^{\text{up}}}{2} \quad (2.4b)$$

where  $\sum v_{\text{cap},x}^y$  is the summation of capacitor voltages in phase  $x$  arm  $y$ .

For the output to have equal magnitude minimum and maximum, the condition in (2.5)

must be satisfied.

$$\sum v_{\text{cap},x}^{\text{up}} = \sum v_{\text{cap},x}^{\text{low}} \quad (2.5)$$

From (2.2b) and (2.3d) to maintain the circulating current ( $i_x^{\text{circ}}$ ) in the MMC to a minimum, one must have:

$$v_x^{\text{comm}} = \frac{v_{\text{dc}}}{2} \quad (2.6)$$

Thus in order to satisfy the minimum circulating currents at all converter operating conditions, including the maximum and minimum ac output voltage generation instances, the summation of capacitor voltage of the upper and lower arms must be equal to the dc link voltage ( $v_{\text{dc}}$ ). Thus;

$$\sum v_{\text{cap},x}^{\text{up}} = \sum v_{\text{cap},x}^{\text{low}} = v_{\text{dc}} \quad (2.7)$$

Sorting and balancing algorithms [23] balance the capacitor voltages in the multivalve. Thus the average capacitor voltage in the MMC is

$$v_{\text{cap, avg}} = \frac{v_{\text{dc}}}{N} \quad (2.8)$$

The control system creates a modulation waveform,  $m(t)$ , where  $-1 < m(t) < 1$  (in general a sinusoidal waveform, but could have other harmonic components in it due to control actions).

The control modulation waveform is used to create two modulation waveforms ( $m_x^{\text{up}}$  and  $m_x^{\text{low}}$  where  $x = a, b, c$ ) for upper and lower arms as shown in (2.9):

$$m_x^{\text{up}} = 0.5 * (1 - m_x(t)) \quad (2.9a)$$

and

$$m_x^{\text{low}} = 0.5 * (1 + m_x(t)) \quad (2.9b)$$

The SMs in the MMC-ES are inserted and bypassed according to the (2.9) signals. There are pulse width modulation (PWM) methods and staircase modulation techniques (nearest level control (NLC)) that determine the number of SMs switched at a given instance [24]. PWM techniques produce outputs with low harmonic distortion with additional switching losses, while NLC generate staircase waveforms with a low number of switching events and high harmonic distortion if the number of SMs is small. With a large number of SMs in practical MMCs, it is recommended to use NLC, while PWM techniques are preferred for converters with a low number of SMs.

### 2.1.3 SM DC-DC Converter

A dc-dc converter is used to interface the energy storage element to the MMC-ES SM capacitor. The ES element could charge and discharge, thus a bi-directional converter is used. The dc-dc converter can be used to control the power discharged from the ES element [25] or maintain the SM average capacitor voltage [15]. Section 2.2 provides a detailed account of the control systems associated with the converter.

## 2.2 Control Systems of MMC-ES

MMC-ES is a voltage source converter. Thus it can be controlled similarly to a regular two-level converter. However, as observed in (2.2b), circulating currents are generated inside the converter. Controllers can be used to manipulate these currents to achieve various control objectives [15, 25]. Since the converter has energy storage, it can work as a three port



converter (a converter that interfaces an ac network, a dc network, and battery storage) [19, 26]. Thus by manipulating circulating currents, dc power control independent of the other power sources can be achieved. The converter contains dc-dc converters in its SMs, and suitable controls need to be implemented for them. This section discusses basic MMC-ES control techniques including an overview of control systems used in literature as well.

### 2.2.1 AC Current Control

Consider the following MMC-ES connected to an ac bus. In this diagram, only one phase is considered (symbol for phase is omitted for simplicity). In Figure 2.5  $L_{tf}$  represents the converter transformer's leakage inductance.

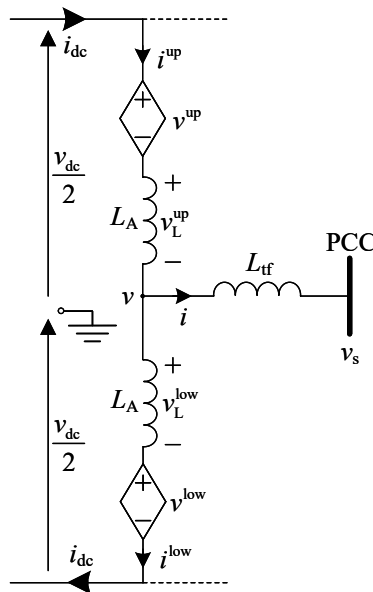


**Figure 2.5:** A single phase MMC-ES connected to an ac network.

Applying Kirchhoff's voltage law (KVL) to the circuit upto the point of common coupling

(PCC) yields:

$$\frac{v_{dc}}{2} - v^{up} - L_A \frac{di^{up}}{dt} - L_{tf} \frac{di}{dt} = v_s \quad (2.10a)$$

$$-\frac{v_{dc}}{2} + v^{low} + L_A \frac{di^{low}}{dt} - L_{tf} \frac{di}{dt} = v_s \quad (2.10b)$$

Adding and subtracting (2.10a) and (2.10b) yields:

$$\frac{(L_A + 2L_{tf})}{2} \frac{di}{dt} = \underbrace{\frac{-v^{low} + v^{up}}{2}}_{v \text{ as from (2.3c)}} - v_s \quad (2.11a)$$

$$L_A \frac{di^{circ}}{dt} = \frac{v_{dc}}{2} - \underbrace{\frac{v^{up} + v^{low}}{2}}_{v^{comm} \text{ as from (2.3d)}} \quad (2.11b)$$

Park's transformation [27] can be applied to (2.11a) to create a dynamic system in a rotating synchronous frame. This well-known method is not presented for brevity; the following dynamic equations are obtained after correctly transforming the equations. The equations are also per unitized. In these equations  $Z_{base}$  and  $\omega$  represent the base impedance and system frequency in rad/s, respectively. Subscripts d and q denote the d-axis and q-axis components of the respective current or voltage.

$$\left( \frac{L_A + 2L_{tf}}{2Z_{base}} \right) \frac{di_{d, pu}}{dt} = -\omega \left( \frac{L_A + 2L_{tf}}{2Z_{base}} \right) i_{q, pu} + v_{d, pu} - v_{sd, pu} \quad (2.12a)$$

$$\left( \frac{L_A + 2L_{tf}}{2Z_{base}} \right) \frac{di_{q, pu}}{dt} = \omega \left( \frac{L_A + 2L_{tf}}{2Z_{base}} \right) i_{d, pu} + v_{q, pu} - v_{sq, pu} \quad (2.12b)$$

Based on (2.12) the ac current's plant model can be developed. Figure 2.6 shows a decoupled current controller derived from the plant to control the d- and q-axis ac line current components, respectively. The controller and the plant are clearly marked on the

control block diagram. In this figure,  $L_{\text{comp, pu}}$  is defined as the pu value of the effective inductance of the MMC-ES and is defined as in (2.13).

$$L_{\text{comp, pu}} = \frac{L_{\Lambda} + 2L_{\text{tf}}}{2Z_{\text{base}}} \quad (2.13)$$

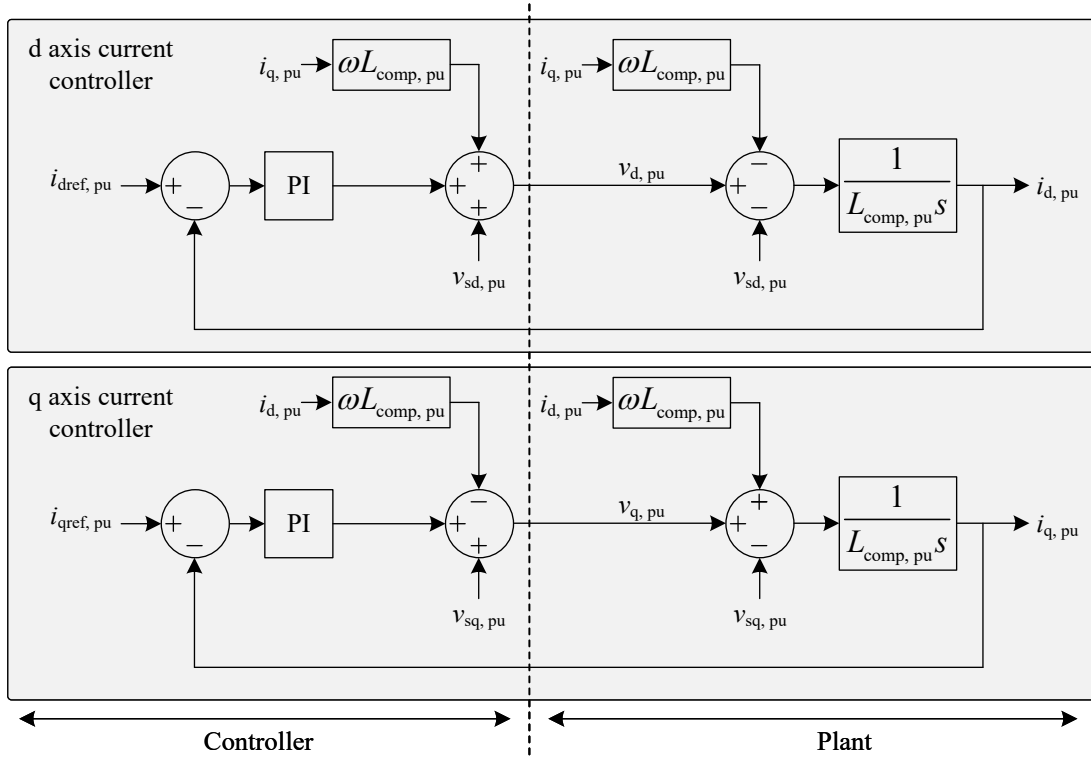


**Figure 2.6:** AC current controller

Decoupling allows one decoupled current component to align with the active power output of the converter ( $i_q$  in this thesis) and the other to align with the reactive power ( $i_d$  in this thesis). This allows to independently control the active power and reactive power (or ac voltage) of the MMC-ES and is referred as the “inverter” operation. The dc voltage of the MMC-ES is related to the active power transfer of the converter, and thus the active

power current component can be used for controlling dc link voltage. This type of operation is referred to as the “rectifier” operation.

The identification and modeling of the plant of the MMC-ES in ac current control allows to tune the PI controllers more efficiently by placing the poles of the closed loop system on the negative real axis or close to negative real axis in the  $s$ -plane. A block diagram representation of the closed loop system is depicted in Figure 2.7 and the closed loop transfer function is described in (2.14).

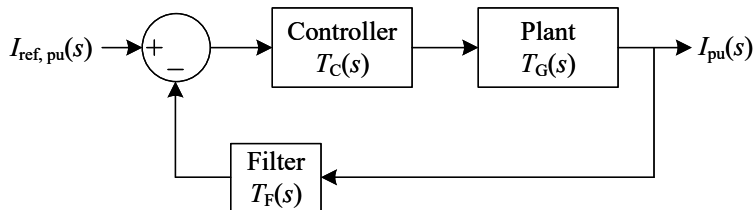


**Figure 2.7:** Block diagram of a closed loop system

$$T_{\text{closed}}(s) = \frac{T_C(s)T_G(s)}{1 + T_C(s)T_G(s)T_F(s)} \quad (2.14)$$

### 2.2.2 Negative Sequence Control

The above ac current control discussion was done for the positive sequence components of voltage and current, which are responsible for the main power transmission within the power system. The positive-sequence controller is sufficient for a balanced three-phase system to operate, but faces limitations when unbalanced loads and faults are present. The imbalances in the system cause power balancing issues in the MMC-ES, which could lead to state of charge (SOC) divergence in MMC-ES SMs. A negative-sequence controller could be used to suppress negative-sequence currents throughout the converter operation, leading to providing balanced ac currents at the output.

Modeling of the converter is quite similar to the positive-sequence controller developed above. The only change is to negate the voltage angle used in Park's transformation. The per-unitized decoupled dynamic equations are as shown in (2.15). The negative-sequence decoupled components derived by Park's transformation contain significant double line frequency ripples, due to the presence of considerable positive-sequence components in the measurement. Thus notch filters are typically used [28] to eliminate the impact of positive-sequence components. It can be observed that the plant is the same for both the positive- and negative-sequence controllers. The modulation waveforms generated by the negative-sequence controller are added to the positive-sequence controller output. Figure 2.8 shows the negative-sequence controller for completeness.

$$\left(\frac{L_A + 2L_{\text{tf}}}{2Z_{\text{base}}}\right) \frac{di_{\text{d, pu}}^{\text{neg}}}{dt} = \omega \left(\frac{L_A + 2L_{\text{tf}}}{2Z_{\text{base}}}\right) i_{\text{q, pu}}^{\text{neg}} + v_{\text{d, pu}}^{\text{neg}} - v_{\text{sd, pu}}^{\text{neg}} \quad (2.15\text{a})$$

$$\left(\frac{L_A + 2L_{\text{tf}}}{2Z_{\text{base}}}\right) \frac{di_{\text{q, pu}}^{\text{neg}}}{dt} = -\omega \left(\frac{L_A + 2L_{\text{tf}}}{2Z_{\text{base}}}\right) i_{\text{d, pu}}^{\text{neg}} + v_{\text{q, pu}}^{\text{neg}} - v_{\text{sq, pu}}^{\text{neg}} \quad (2.15\text{b})$$

Zero-sequence currents are also generated by the converter during faults and unbalanced load conditions. However, the delta-star configured converter transformer (delta on converter side) blocks the zero sequence currents entering the ac network.

### 2.2.3 Circulating Current Control

In normal operation, MMC-ES inserts  $N$  SMs between the dc poles. This insertion happens according to a modulation method and is based on sorting and balancing algorithms (discussed in section 2.1.2) to maintain the average SM voltage at  $v_{\text{dc}}/N$  (2.8). The instantaneous capacitor voltage has a ripple around the average voltage. This causes circulating currents to be generated within the MMC-ES. These currents do not pass to the ac network

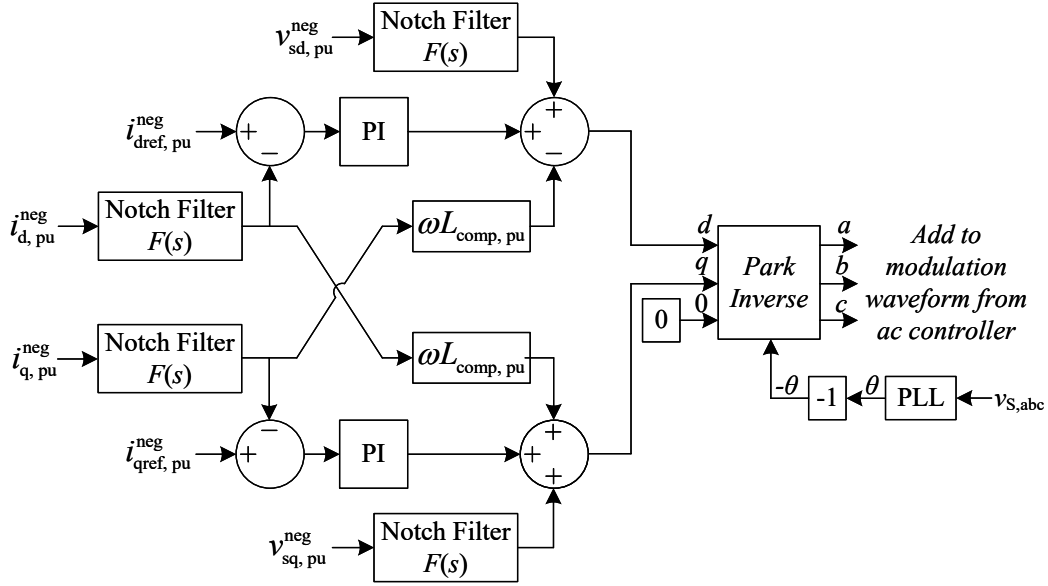


**Figure 2.8:** Negative-sequence current controller.

of the MMC-ES, but enter the dc network and are driven by  $v^{\text{circ}}$  (2.3d). The circulating currents cause resistive losses in the converter and result in larger capacitor voltage ripples. An analysis of circulating currents of MMC-ES is done in detail in Chapter 3 shows that they are a combination of a number of harmonics of the fundamental frequency including a dc component.

Circulating currents are controlled to reduce losses [29], manipulate capacitor voltage ripple [30], and transfer power between MMC-ES phase arms and phase legs [25]. Resonance controllers are used to control the circulating currents in literature [25]. Resonance controllers are second-order transfer functions in general (as in (2.16)) having a resonance point at the resonance frequency ( $\omega_r$ ) and a damping ratio of  $\zeta$ . The frequency response of a general resonance controller is shown in Figure 2.9.

$$T_{\text{res}}(s) = \frac{K_a s + K_b}{s^2 + 2\zeta\omega_r s + \omega_r^2} \quad (2.16)$$

The decoupled control strategy discussed in section 2.2.1 can be employed to control the

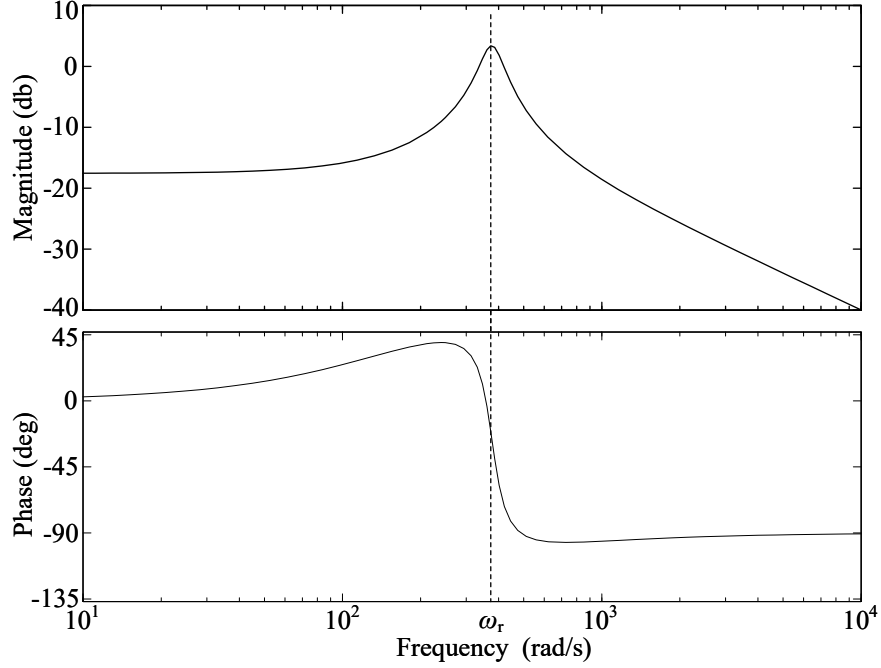


**Figure 2.9:** Frequency response of a resonance controller.

circulating current of any harmonic, positive or negative sequence. The dynamic equation derived for circulating currents in (2.11b) can be per unitized and decoupled in a rotating synchronous frame as shown in (2.17). In this equation,  $n$  ( $n \in \mathbb{Z}, n \neq 0$ ) is the harmonic number with the sign representing the sequence order (i.e., positive sequence, negative sequence).

$$\frac{L_A}{Z_{\text{base}}} \frac{di_{d, \text{pu}}^{\text{circ}}}{dt} = \frac{-n\omega L_A}{Z_{\text{base}}} i_{q, \text{pu}} - v_{d, \text{pu}}^{\text{comm}} \quad (2.17a)$$

$$\frac{L_A}{Z_{\text{base}}} \frac{di_{q, \text{pu}}^{\text{circ}}}{dt} = \frac{n\omega L_A}{Z_{\text{base}}} i_{d, \text{pu}} - v_{q, \text{pu}}^{\text{comm}} \quad (2.17b)$$

DC power sharing with the main dc link of the converter causes dc circulating currents in the MMC-ES. Since the MMC-ES has local generation, the dc power could be zero,

yet the converter may have power transmission with the ac network. Thus it is essential to have a dc power control capability within the MMC-ES. DC power control is done by controlling the dc component of the circulating currents, which is done using PI controllers. The low-pass nature of the PI controller attenuates the sinusoidal harmonics in the circulating currents. Figure 2.10 shows the control of dc power and circulating currents of phase  $x$ .  $P_{dc,x}$ ,  $P_{dc\ ref, x}$ ,  $i_{ref, x}^{circ}$  denote the dc power, dc power reference and circulating current reference of phase  $x$ , respectively.

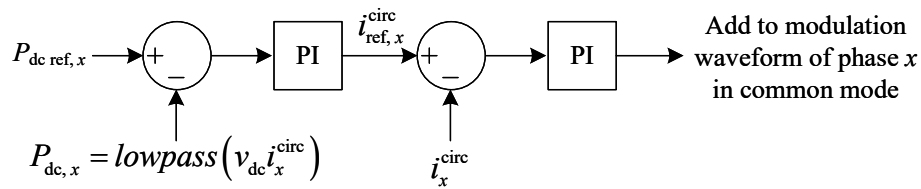


**Figure 2.10:** Block diagram of dc circulating current control and dc power control.

## 2.2.4 DC-DC Converter Control

The SMs of MMC-ES may include a dc-dc converter to control the charging/discharging of the energy storage element. A bidirectional dc-dc converter is employed for this purpose. Modelling of the bi-directional dc-dc converter and development of a unified controller is presented in [31]. This type of controller does not arrive at discontinuous conduction mode (DCM) and can smoothly transition between charging and discharging modes as shown in [31] as well as in this thesis. The small-signal analysis required to develop this controller is well known in power electronics community and can be found in [32]. Figure 2.11 shows the block diagram of the dc-dc controller. In this figure,  $v_C$ ,  $v_{bat}$ ,  $i_L$ ,  $d$ ,  $V_{C,o}$ ,  $D_o$  represent the SM capacitor voltage, SM battery voltage, SM dc-dc converter inductor current (discharging



current considered positive), dc-dc converter duty ratio, operating point average capacitor voltage and operating point average duty ratio, respectively.

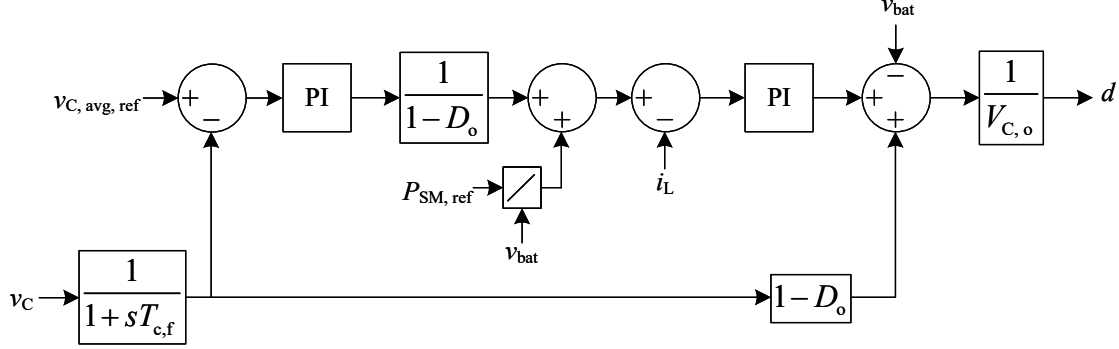


**Figure 2.11:** Unified controller for bi-directional dc-dc converter.

### 2.2.5 State-of-Charge (SOC) Balancing Control

Energy storage elements (batteries in this research) are distributed among the SMs of the MMC-ES. This allows the added flexibility of controlling the SOC of battery elements to uniformly charge and discharge the batteries within the MMC-ES. Based on the principle of the converter operation, SOC balancing can be viewed as three control objective, namely at the phase level, at the phase arm level, and at the SM level. The “phase level” control aims to equate the average SOC of a given phase ( $SOC_x$ ) to the average SOC of the MMC-ES ( $SOC_{BESS}$ ). The “arm level” controller aims in balancing the upper and lower phase arm average SOC ( $SOC_{x,y}$ ) with the average SOC of the phase ( $SOC_x$ ). The “SM level” SOC controller aims to balance the individual SM battery ( $SOC_{x,y,i}$ ) to the average SOC of the phase arm ( $SOC_{x,y}$ ). Here,  $x = a, b, c$  denotes the phase,  $y = \text{up, low}$  denotes the phase arm, and  $i = 1 : N$  denotes the SM number of a given phase arm. In order to balance the SOC over the given levels, active power needs to be transferred between phases, phase arms

and SMs. Circulating currents of the orders dc, positive sequence and negative sequence can be used to transfer power among phase legs and phase arms as proved in [25]. The SM SOC balancing is done by manipulating the power reference for the dc-dc converter ( $P_{SM, \text{ref}}$  in Figure 2.11). The power references to balance phase SOC in each level ( $\Delta P_{x,0}^{\text{circ}}$  to transfer power between phases and  $\Delta P_{x,1}^{\text{circ}}$  to transfer power between phase arms) are created by proportional controllers (PI controllers cannot be used as the total SOC change with time during the control process. The controller can only provide a trend of the SOC, which is done using the proportional controller) as shown in Figure 2.12. The power references could then be related to circulating current references by following the method in [25]. Different SOC terms used in Figure 2.12 is defined mathematically in (2.18)

$$SOC_{x,y} = \frac{\sum_{i=1}^N SOC_{x,y,i}}{N} \quad (2.18a)$$

$$SOC_x = \frac{SOC_{x,\text{up}} + SOC_{x,\text{low}}}{2} \quad (2.18b)$$

$$SOC_{\text{BESS}} = \frac{SOC_a + SOC_b + SOC_c}{3} \quad (2.18c)$$

## 2.3 MMC-ES Modeling Techniques

As described in previous sections, MMC-ES are quite complex converters with a large number of active and passive components. A conventional MMC used in HVDC applications contains hundreds of SMs in a single multivalve. Simulating the converter's electromagnetic transients is important to understand the behaviour of such converters. Literature has presented models

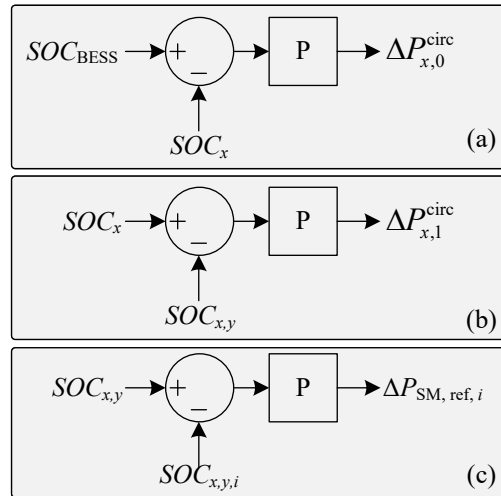


**Figure 2.12:** SOC balancing controllers: (a) phase level (b) arm level, (c) SM level

with various levels of complexity for regular MMCs. In this section, a review of models used to study regular MMCs is presented as a prologue to the models developed for MMC-ES. References [33, 34] provide comparison of different models discussed in this section.

Figure 2.13 shows a regular MMC and a half-bridge SM used in the converter. Both regular MMC and MMC-ES follow the same converter layout. The SM is simple in regular MMC with a small number of components. The SM contains an additional high-speed bypass switch (K1) and a press-pack thyristor (K2) to protect the SM during a fault. As discussed in the next section, various models of the regular MMC have been developed for the study of the converter.

### 2.3.1 Detailed IGBT-Diode Based Model

This model individually represents each component in the MMC with a fully detailed simulation model [35]. Any type of hybrid MMC topology could be modeled using this method due to its flexibility. Semiconductor devices such as IGBTs and diodes are modeled including

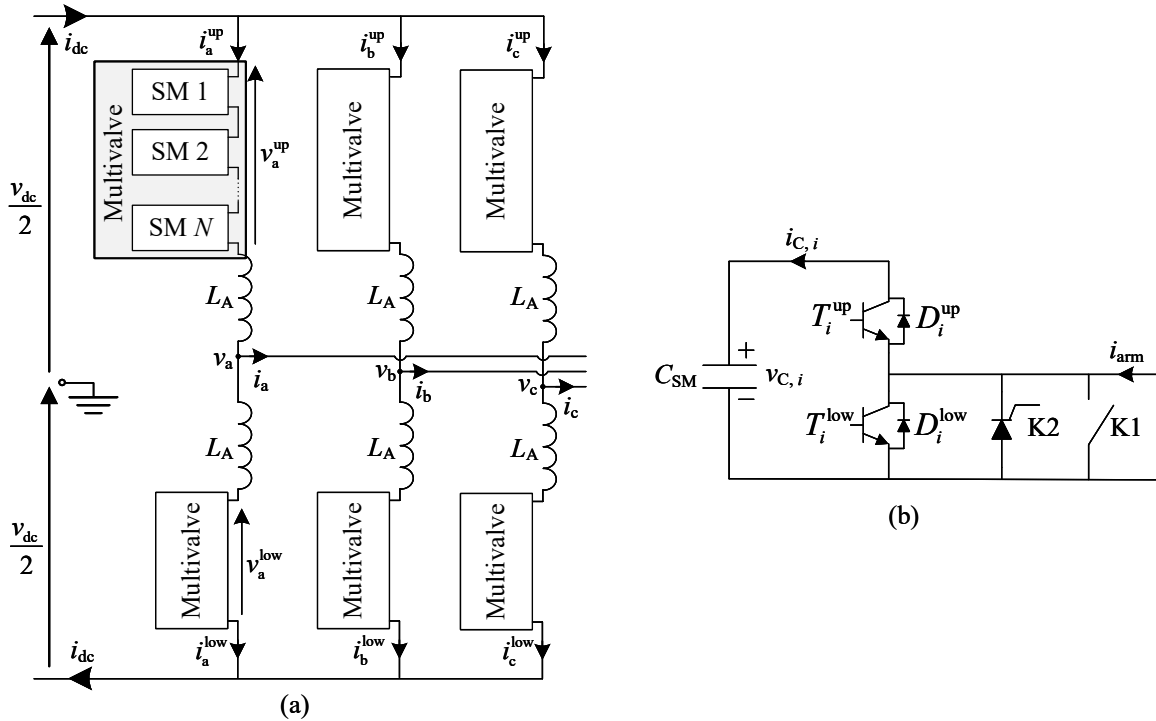


Figure 2.13: Regular MMC (a) converter schematic diagram (b) half-bridge SM

the non-linear nature of their voltage-current (V-I) characteristics (Figure 2.14). The high level of detail in this type of models allows to accurately model the switching and conduction losses of the converter. Although this model produces highly accurate results, its computation requirements are commensurately high. The primary application of this type of models is to study losses of the converter at specific operating points.

### 2.3.2 Detailed EMT Model

EMT simulation programs consider power electronic switches as variable resistances having a low on-state resistance ( $R_{on}$ ) and a large off-state resistance ( $R_{off}$ ) (Figure 2.15). Since power electronic switches operate in saturation (on state) or cut-off (off-state) modes, this

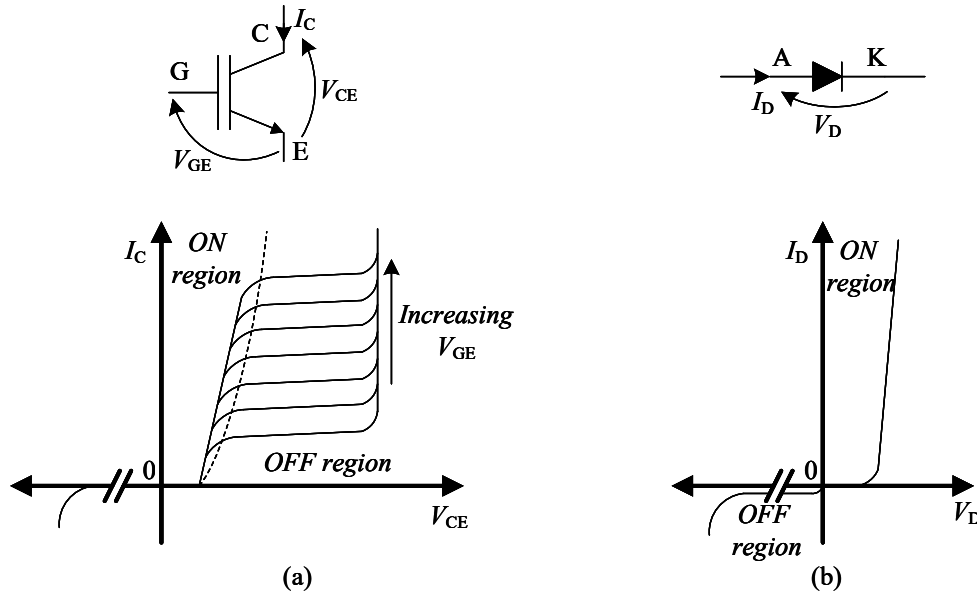


Figure 2.14: Nonlinear characteristics of semiconductors: (a) IGBT (b) diode

approximation is valid to a large extent. Although the accuracy of the resulting simulation models is not as high as the models in section 2.3.1, they produce reasonably accurate results compared to averaged-value models discussed in next sections. Since this model type uses individual components to form the simulation model, the converter topology could be flexibly changed. Due to the large number of components present in a network, the resulting admittance matrix [36] becomes quite large. This leads to requiring very high computational power to solve the network, which in turn translates to high cost for simulation equipment.

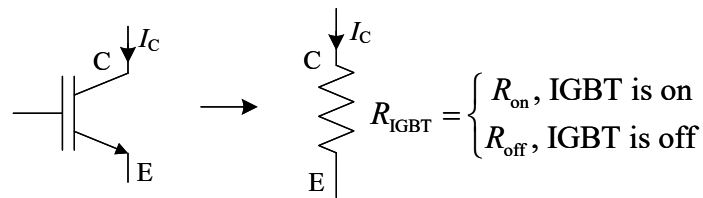


Figure 2.15: Representing an IGBT in an EMT environment.

### 2.3.3 Detailed Equivalent EMT model

To reduce the simulation complexity of the previous models without losing information at the SM level, detailed equivalent models (DEM) are developed [37]. This model type reduces the MMC multivalve into a single Thevenin voltage source. This is done by first simplifying each SM to a single Thevenin equivalent and then by adding each Thevenin equivalent to create an overall Thevenin equivalent for the multivalve. Each SM's Thevenin voltage and resistance depend on the firing pulses given to it, previous time-step SM capacitor voltage, and arm current. The procedure of developing the DEM is shown in Figure 2.16. In this figure,  $V_{C,h}$  and  $R_C$  denote the equivalent voltage source of the capacitor and the EMT equivalent resistor, which are parts of the capacitor representation in the EMT environment. Full details of this derivations are found in [37]. This model markedly reduces the number of nodes appearing in the admittance matrix, thus making the simulation faster. The Thevenin equivalent calculation algorithm saves the information for each SM capacitor voltage and current; therefore, no information is lost. However, for different MMC topologies, the DEM has to be rebuilt and validated.

### 2.3.4 Switching Function-Based AVM

Averaged-value models (AVM) for MMCs are developed to simulate the converter with computational efficiency. The model type uses controlled voltage and current sources to model the ac side and dc side separately. The model assumes perfectly balanced internal variables such as SM capacitor voltages. Second-order circulating currents are also assumed to be suppressed. The modulation waveform generated by the controller ( $m_x$ ) is used to create the upper- and lower-arm voltages ( $v_x^{\text{up}}$  and  $v_x^{\text{low}}$ ) as in (2.19). Subscript  $x$  represents the phase.

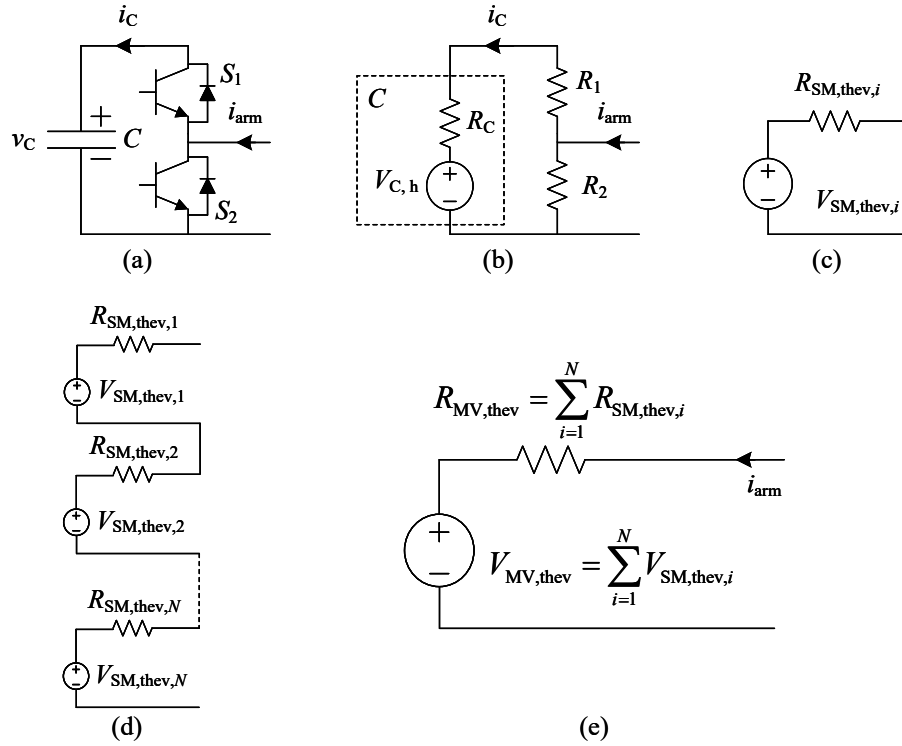


**Figure 2.16:** Development of the DEM for regular MMC (a) SM of a regular MMC (b) EMT equivalent of the SM (c) Thevenin equivalent of the SM (d) multivalve presented as a series collection of SM Thevenin sources (e) multivalve simplified to a Thevenin source

$$v_x^{\text{up}} = v_{\text{dc}} \frac{1 - m_x}{2} \quad (2.19a)$$

$$v_x^{\text{low}} = v_{\text{dc}} \frac{1 + m_x}{2} \quad (2.19b)$$

The dc side is developed based on power balance principles. A current source along with an equivalent capacitor ( $C_{\text{eq}}$ ) is used to represent the dc side. The current source magnitude is determined by the ac power output and the losses occurring in the MMC. With  $v_x$ ,  $i_x$ , and  $R_{\text{loss}}$  representing the MMC's ac voltage output, ac current output (Figure 2.13), and

converter resistance, the current source magnitude ( $I_{dc}$ ) is calculated as in (2.20)-(2.22). Equivalent capacitance is found as in (2.23) where  $C$  is the SM capacitance. Figure 2.17 shows the schematic views of the AVM.

$$I'_{dc} = \frac{\sum_{x=a,b,c} v_x i_x}{v_{dc}} \quad (2.20)$$

$$I_{loss} = \frac{P_{loss}}{v_{loss}} = \frac{R_{loss}(I'_{dc})^2}{v_{dc}} \quad (2.21)$$

$$I_{dc} = I'_{dc} - I_{loss} \quad (2.22)$$

$$C_{eq} = \frac{6C}{N} \quad (2.23)$$

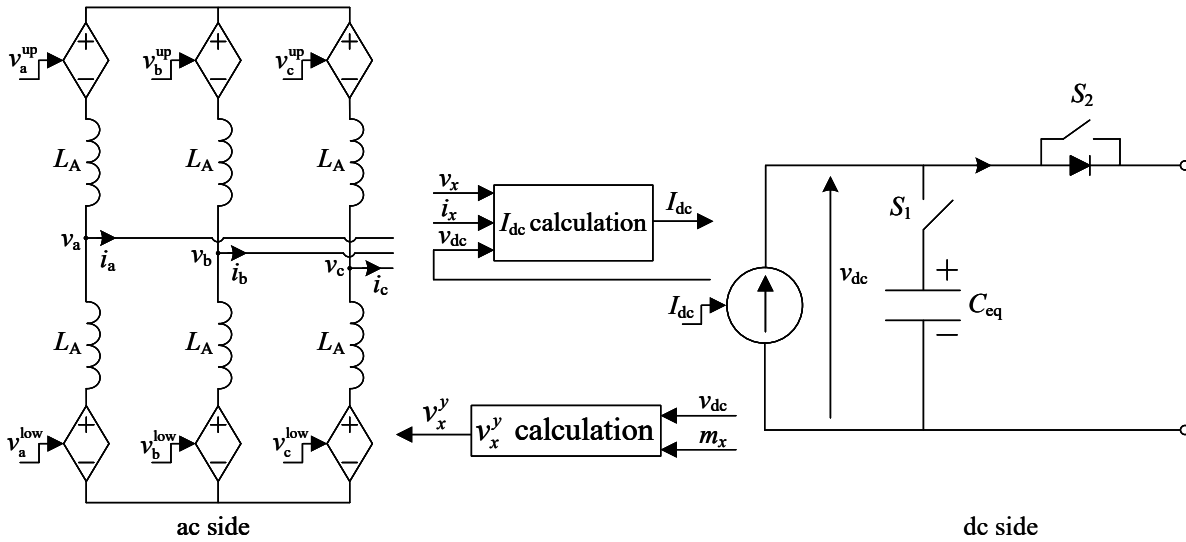


Figure 2.17: Switching function-based AVM

The model is introduced in [35], which compares this model with other models for dynamic performance in [34]. The authors of [38] further analysed this model and provided



conclusions that this AVM is only effective as long as the SM capacitor is large enough and that it cannot accurately model dc faults. The authors of [38] further improved this model to accurately simulate dc faults.

Although this AVM provides good simulation efficiency, it has some limitations. The model assumes perfectly balanced SM capacitors throughout the converter. This leads to the assumption of suppressed second-order harmonics in circulating currents. Thus, this model cannot be used to study the impact of circulating current controllers, which are an integral part of MMC technology. Additionally, the topology of the circuit needs to be altered when simulating dc faults (open  $S_1$  and  $S_2$  in Figure 2.17).

### 2.3.5 Converter-Level AVM

This model type reduces the AVM presented in section 2.3.4 further to represent the ac side by three voltage sources. The dc side is maintained the same as in section 2.3.4 [39]. This model is similar to the average models commonly developed for 2- and 3-level converters [33]. Unlike 2- and 3-level converters, an inductance ( $L_{A,ac}$ ) is placed in series with the ac side to mimic the effect of the arm inductor ( $L_A$ ). Due to this inductor's inclusion, an equivalent inductor ( $L_{A,dc}$ ) should be placed on the dc side as well to represent the dynamics of the arm inductor on the dc side. It should be noted that one third of dc current flows in each phase of the MMC and flows via two arm inductors that are in series. The values of  $L_{A,ac}$  and  $L_{A,dc}$  are calculated in (2.24) and (2.25), respectively. The schematic diagram of this model is shown in Figure 2.18.

$$L_{A,ac} = \frac{L_A}{2} \quad (2.24)$$

$$L_{A,dc} = \frac{2L_A}{3} \quad (2.25)$$

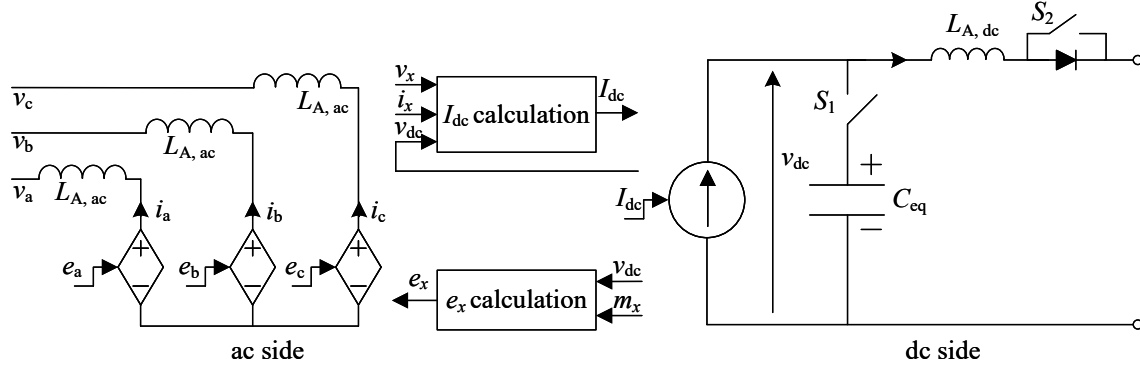


Figure 2.18: Converter-level AVM

## 2.4 Use of MMCs with Energy Storage in Frequency Support

The need for energy storage in power systems started to emerge with the increasing penetration of non-conventional renewable energy sources. Until then, power generation was dominated by conventional generation schemes such as coal, natural gas, nuclear, and large hydro generators that can provide constant power output and are highly predictable. Wind power and solar PV power have become the most popular non-conventional renewable energy sources although they are highly unpredictable sources. This was not an issue with high percentage of conventional generation in the system; however, with the rapid increase of utilization of wind and solar PV power, several concerns have been raised. Reduction of power system inertia, fluctuations of generation, unpredictable nature of power, unavailability of power (low wind season for wind power and night time and cloudy days for solar PV) are some of the issues associated with the above mentioned non-conventional renewable

sources. In order to minimize or eliminate these issues, energy storage has been considered. Most industry implementations have been commissioned using conventional two-level inverter topologies, but much research has been done to find out the feasibility of MMC-ES for energy storage applications.

### 2.4.1 Wind Power

Large scale wind generation has emerged in the form of offshore installations due to the favourable conditions for wind generation [40]. Wind power plants in certain applications are connected to the on-shore power network via HVDC submarine cables to overcome various issues associated with HVAC cables. VSC topologies must be used at the offshore HVDC terminal as no strong grid exists. MMCs are typically used as the VSC of choice. Offshore wind farms are typically rated from several hundreds of MWs to several GWs and such large amounts of power penetration into the onshore power network could cause issues if the injection is fluctuating and unreliable. Authors of [41] have used MMC-ES at each offshore wind turbine to improve the power output of the wind turbine. However, this arrangement causes issues since placing MMC-ES that requires a larger foot print offshore could increase the capital cost of the project as well as the maintenance cost.

Research on wind farms associated with MMC-ES is quite limited, although wind power plants and energy storage have been a key topic of research. Energy storage sizing for wind farms to act as energy buffers have been studied in [42–44]. Different control strategies with energy storage to provide frequency support for the system have been studied in [45–47]. A case study has been presented in [48], which presents a proposal to overcome issues related to installation of wind power on the Swedish island of Gotland. The island is connected to Sweden via two HVDC cables and high penetration of wind power on Gotland system

has caused stability issues where the authors try to overcome the problems by using central energy storage. Authors of [13] propose an unconventional solution to level the wind farm output by storing energy in an offshore wind farm using a series superconducting magnetic coil in HVDC link.

### 2.4.2 Solar PV Power

Solar power is being used as solar thermal and solar PV in the power system. Solar thermal stations work by melting sodium chloride with the sun's energy using concentrated mirrors and driving a steam turbine by transferring the heat in the salt [49]. This process is quite stable and variations in solar irradiance take effect slowly with large time constants, so that they do not have any drastic impacts on the power network. However, this technology is quite expensive and limited to certain geographic locations [50]. Solar photovoltaic (PV) technology works using semiconductors, which directly convert the energy of photons in sunlight to a dc current. Decreasing prices, flexibility, availability to use in most parts of the planet have made solar PV technology quite popular. However, the power output is directly proportional to the solar irradiance and the temperature at the solar panel, and can fluctuate due to cloud movement. With hundreds of megawatts (MWs) to several gigawatts (GWs) range solar PV installations in large solar PV power plants, the power fluctuations may amplify to an extent that may make the power system unstable.

MMC topologies have been able to attract the attention of many researchers as a means of integrating solar PV panels to the power system. The works presented in [17, 51] have integrated PV panels to the MMC SM via a dc-dc converters. Multiple PV panel injections takes place in a single SM. The authors have used the internal power flow control capability of the MMC-ES [25] to integrate SMs with energy storage to balance any power mismatches

occurring in each SM, phase arm and/or phase of the converter. Applicability of using full-bridge SMs to integrate multiple PV modules per SM via dc-dc converters have been researched in [52]. The authors of [53] have integrated energy storage to the main high voltage dc link of the MMC and have introduced solar PV panels via dc-dc converters to each SM. In [54] the PV modules are directly connected across the MMC SM capacitor.

Although much research has been done with the use of MMC to integrate solar PV panels, there are some concerns that need attention. Solar PV panels are placed on ground and the metal framing of the panel must be solidly grounded [55,56]. The MMC SM capacitor voltage relative to the ground vary in a large range and can reach a very high value. Therefore, isolated dc-dc converters must be used in the dc-dc conversion stage that is used to couple the PV module to the SM. This raises a concern of the work done in [54]. For a large number of PV panels connecting to the MMC, the converter footprint is a probable concern. High number of cables will enter the converter hall from each solar module, and could cause issues in heat management, protection, etc. When batteries are used in the main high voltage dc link as in [53], special concern regarding the series connection limit of batteries will arise, as high voltage dc polarization could damage the individual battery cells.

Due to the intrinsic nature of solar irradiance, energy storage has proved essential with the use with solar PV panels. Utilities tend to request energy storage with large scale solar PV installations in order to make the system more dispatchable as well as reliable. This has made technologies to integrate energy storage and solar PV panels an attractive research area.

### 2.4.3 Control Systems Associated with Providing Frequency Support

The loss of generation in an interconnected power system will cause a decline in the overall system frequency. The rate of change of frequency (ROCOF) drop is determined by the available rotating system inertia. The inertia is fundamentally not determined by a control system, but rather depends on the rotating synchronous mass in the power system. If there is no further controls in generation, the unbalanced generation and load could gradually reduce the system frequency, causing the system to lose stability. Droop controllers are implemented at the generation units with upper and lower headroom to increase the power output as the local frequency reduces. This causes an increase in generation and the system reaches a minimum frequency (frequency nadir) and settles at a new temporary steady state. This operates within 1-2 s after the disturbance. The automatic generation control (AGC), which is centrally located, sends out power set-points to the controllable generators to recover the system frequency to the nominal value. This is activated after several tens of seconds to several minutes following an event. The frequency has typically reached a temporary steady state when the AGC is activated. This control is typically referred to as secondary frequency control (SFC). Finally, tertiary frequency control (TFC) is activated after several minutes following a disturbance, to bring back the generators to pre-disturbance loading values by bringing in or retiring generation to allow headroom for the next transient. Figure 2.19 shows the different control actions discussed above following a disturbance [5].

Frequency support control systems are developed based on the principles of conventional generation for the inverter-based generation schemes as well. The main control systems can be viewed as the fast frequency response (FFR) and the primary frequency response (PFR). The secondary control and the tertiary control can be implemented similar to conventional

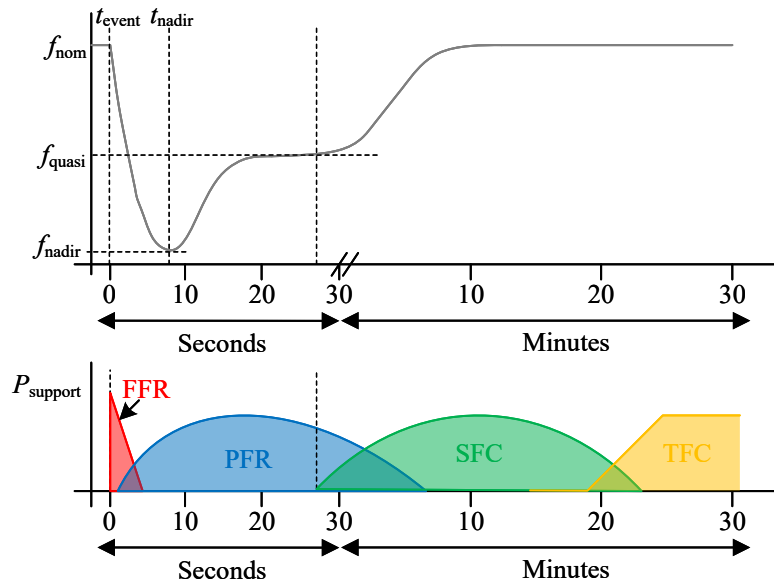


**Figure 2.19:** System frequency and response following a generation loss.

generation.

FFR is implemented in inverter-based technologies by injecting active power proportional to the ROCOF of the system. Most inverter controllers are associated with phase locked loops (PLL) to get information on the phase and the frequency information at the point of the common coupling. The frequency captured from the PLL can be used to calculate the ROCOF and create an additional power reference ( $P_{\text{ref, deriv}}$ ) to inject a proportional power element to reduce the rate of change of frequency (Figure 2.20). It should be noted that the derivative calculation of the frequency tends to have sudden variations and a filter function is required to eliminate any unnecessary noise. This filtering can be achieved by a moving window that captures the frequency change over time.

PFR is implemented as a droop controller as in Figure 2.21. A deadband is typically used to avoid unnecessary action to be taken by the controller. This controller creates a power reference ( $P_{\text{ref, droop}}$ ) proportional to the frequency difference.

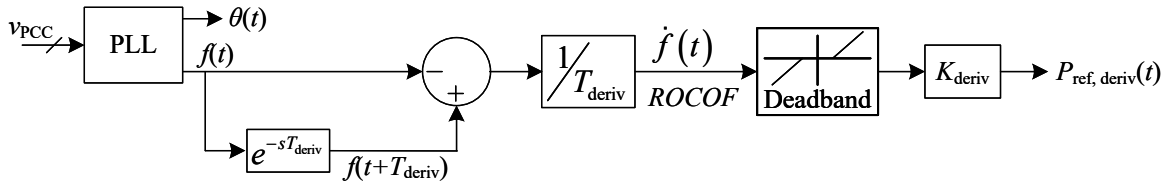


**Figure 2.20:** Derivative power controller

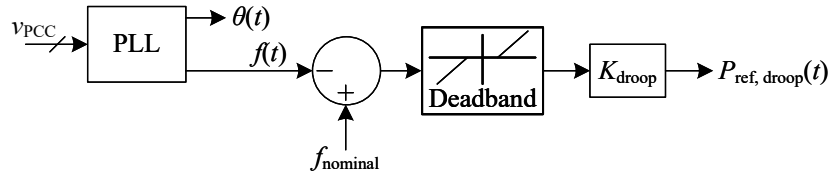


**Figure 2.21:** Droop power controller

These types of controllers heavily depend on the capability of the PLL to provide an accurate response. Faults around interconnections with high network impedance could lead to PLL being out of phase while incorrectly estimating network frequency. This could lead to erroneous response from ancillary service controllers.

As a solution for the issues risen from the PLL, grid-forming converter technologies have been developed. In such schemes the inverter is operated as a voltage source behind a reactance, and the self synchronizing feature of synchronous machines is used to find the phase angle of the inverter. These converters provide an inherent damping to the system and good response in weak, high-impedance connection points [57]. However, controlling the currents of grid-forming converters during faults is not as direct as in grid-following converters, which use PLLs.

Providing frequency support actions discussed above requires the ability to absorb or provide active power to the power system as needed. This requirement is viewed differently for each technology. Solar PV units typically operate at the maximum power point to increase



the efficiency of the system. During an over-frequency transient, the inverter could reduce the power output, but is not able to ramp up the power in a situation where an active power injection is required to arrest a frequency drop. This requires the solar PV unit to keep a reserve power portion to be used when required.

Wind farms also operate at the maximum power point similar to solar farms, but have an added advantage. The rotating blades of the wind turbine store a considerable amount of energy, which could be extracted to provide frequency support actions when required. The controller should only use this function to reduce the speed and only within the operating capability of the wind turbine.

Battery storage systems store energy to be provided to the network on demand. The battery unit may be required to absorb some power from the system in an over-frequency event. Thus the battery management system should maintain the battery at an optimal state-of-charge to allow maximum usage of stored energy as well as providing ability to absorb power.

## 2.5 Summary

This chapter presented an overview of the MMC-ES converter, its operation, and control. Fundamental control systems associated with the MMC-ES were presented. A prologue for MMC-ES simulation models was presented with a detailed literature review on the available models to simulate conventional MMCs used in HVDC transmission. The chapter also discussed the use of energy storage in frequency support, along with renewable sources.

## Chapter 3

# Analysis of the Converter with Averaged-Value Model

A preliminary analysis of MMC-ES is possible via simplified models such as the one in [19], in which the concept of the multivalve is lost. Alternatives such as electromagnetic transient (EMT) simulation models as in section 2.3.1 and 2.3.2 can provide detailed representations of the converter at the expense of a massive computational burden. A detailed equivalent model (DEM) [58] is able to alleviate the computational burden of EMT-type simulations without loss of accuracy. However, both conventional EMT and DEM models are numerical in nature and do not readily lend themselves to analytical studies such as controller tuning, small-signal analysis, and investigation of circulating currents, capacitor voltage ripple, and component sizing. Clearly there is need for an explicit, computationally affordable model with consideration of the multi-valve dynamics to enable these studies via formal methods. This section fills this gap by developing an averaged-value model (AVM) of the multivalve in an MMC-ES. The applicability of the model is demonstrated in several scenarios. The

AVM may be readily integrated into an existing EMT simulator for system-level studies of the converter, or be used independently as an analytical representation of the converter.

The AVM discussed in this section concentrates on SMs formed with a battery as the energy storage, bi-directional dc-dc converter as a filter and a half-bridge switching arrangement (see Figure 2.2). A schematic diagram of the MMC-ES and the SM is repeated in Figure 3.1 for reference in the derivations in following sections.

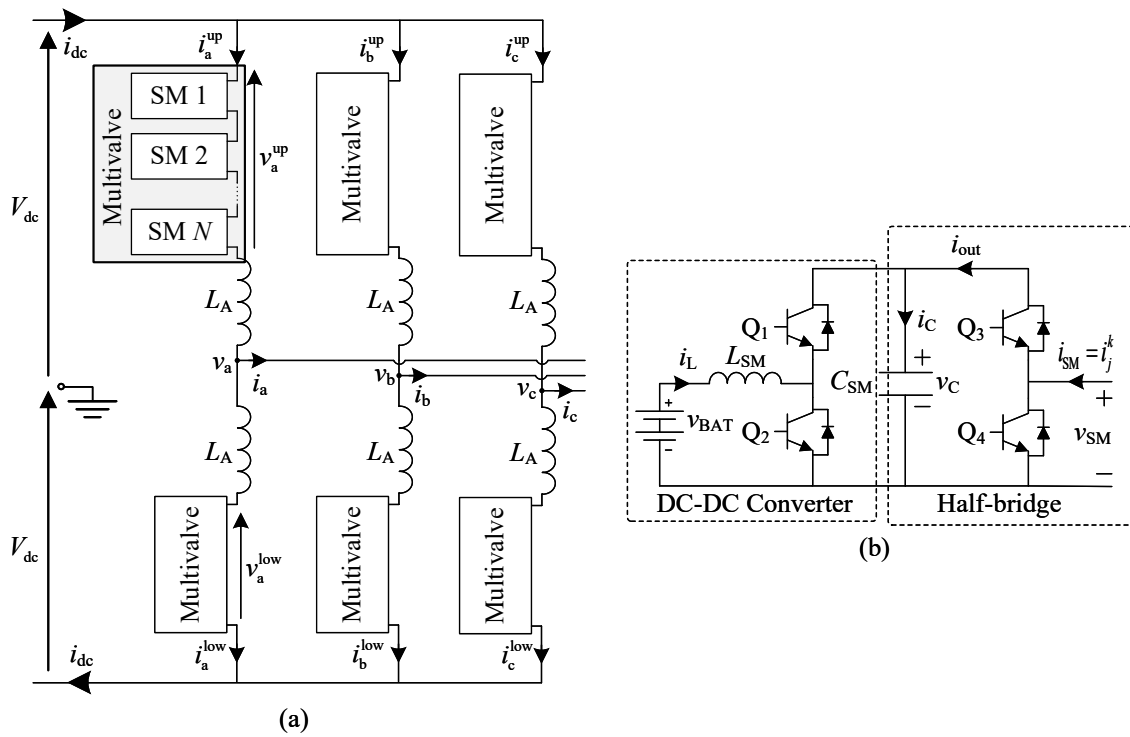


**Figure 3.1:** MMC-ES and used SM schematic. (a) MMC-ES (b) SM

## 3.1 Averaged-Value Model

### 3.1.1 Averaged-Value Model of the DC-DC Converter

The dc-dc converter formed using  $Q_1$  and  $Q_2$  displays two states during its operation. State 1 applies to  $0 < t < dT_s$  and state 2 to  $dT_s < t < T_s$ , where  $d$  is the duty ratio and  $T_s$  is the switching period of the dc-dc converter. Figure 3.2 shows the equivalent circuits of the dc-dc converter in these two states. Note that there are  $N$  such dc-dc converters in each arm; however, their individual quantities are not shown for clarity.

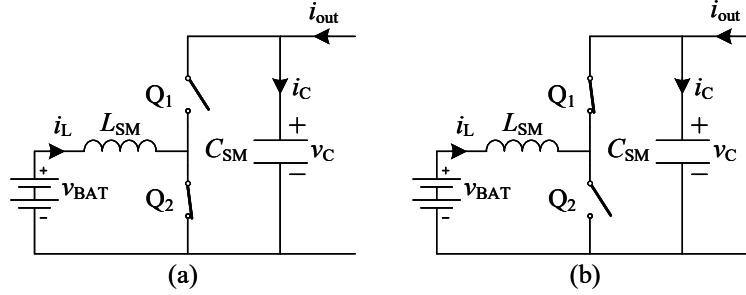


**Figure 3.2:** States of the dc-dc converter (a) state 1 (b) state 2

The converter's governing equations are as follows.

For state 1:

$$\frac{di_L}{dt} = \frac{1}{L_{SM}} v_{BAT} \quad (3.1)$$

$$\frac{dv_C}{dt} = \frac{1}{C_{SM}} i_{out} \quad (3.2)$$

For state 2:

$$\frac{di_L}{dt} = \frac{1}{L_{SM}} v_{BAT} - \frac{1}{L_{SM}} v_C \quad (3.3)$$

$$\frac{dv_C}{dt} = \frac{1}{C_{SM}} i_L + \frac{1}{C_{SM}} i_{out} \quad (3.4)$$

Equations (3.1)-(3.4) may be combined into two weighted averaged equations as shown in (3.5) and (3.6). In these equations, the horizontal line above variables indicates their average values over a switching period.

$$\frac{d\bar{i}_L}{dt} = \frac{1}{L_{SM}}v_{BAT} - \frac{1}{L_{SM}}(1-d)\bar{v}_C \quad (3.5)$$

$$\frac{d\bar{v}_C}{dt} = \frac{1}{C_{SM}}(1-d)\bar{i}_L + \frac{1}{C_{SM}}i_{out} \quad (3.6)$$

The SMs in the top and bottom arms are inserted in a sinusoidal manner. The participation of each arm can be expressed using arm modulating waveform,  $m^{up}$  and  $m^{low}$  (see (3.7) and (3.8)), that are obtained from the normalized reference waveform to be generated at the converter's ac terminals. The normalized reference waveform ( $m_{ref}$ ) is sinusoidal with a magnitude of  $m$  (the modulation index of the converter).

$$m^{up} = \frac{1}{2}(1 - m_{ref}) \quad (3.7)$$

$$m^{low} = \frac{1}{2}(1 + m_{ref}) \quad (3.8)$$

$$m_{ref} = m \cos(\omega t) \quad (3.9)$$

Viewed over the dc-dc converter's switching frequency,  $i_{out}$  can be considered as a slowly varying value. Using (3.7) and (3.8) the current  $i_{out}$  can be represented as follows:

$$i_{out} = m_j^k i_j^k \quad (3.10)$$

where  $j \in \{a, b, c\}$  denotes the phase, and  $k \in \{up, low\}$  denotes the arm. Based on (3.6) and (3.10), the following equation can be developed for the average capacitor voltage of arm

$k$  in phase  $j$ .

$$\bar{v}_{C,j}^k = \frac{1}{C_{SM}} \int \left[ (1 - d_j^k) \bar{i}_{L,j}^k + m_j^k i_j^k \right] dt \quad (3.11)$$

### 3.1.2 SM Capacitor Voltage Ripple

For brevity of presentation, the following derivations are shown for one phase of the converter.

In general, the arm currents ( $i^{\text{up}}$  and  $i^{\text{low}}$ ) may be represented in terms of their harmonic contents as in (3.12) and (3.13).

$$i^{\text{up}} = \sum_{n=0}^{\infty} i_n^{\text{up}} \quad (3.12)$$

$$i^{\text{low}} = \sum_{n=0}^{\infty} i_n^{\text{low}} \quad (3.13)$$

Substituting (3.12) and (3.13) in (3.11) with (3.7), (3.8), and (3.9) yields:

$$\bar{v}_C^{\text{up}} = \frac{1}{C_{SM}} \int \left[ (1 - d^{\text{up}}) \bar{i}_{L^{\text{up}}} + \frac{1}{2} (1 - m \cos(\omega t)) \left( \sum_{n=0}^{\infty} i_n^{\text{up}} \right) \right] dt \quad (3.14)$$

$$\bar{v}_C^{\text{low}} = \frac{1}{C_{SM}} \int \left[ (1 - d^{\text{low}}) \bar{i}_{L^{\text{low}}} + \frac{1}{2} (1 + m \cos(\omega t)) \left( \sum_{n=0}^{\infty} i_n^{\text{low}} \right) \right] dt \quad (3.15)$$

Integrating these over a fundamental frequency cycle yields:

$$\bar{v}_C^{\text{up}} = \frac{1}{C_{SM}} \int_0^T \left[ (1 - d^{\text{up}}) \bar{i}_{L^{\text{up}}} + \frac{1}{2} i_0^{\text{up}} - \frac{1}{2} \hat{i}_1^{\text{up}} m \cos(\omega t) \cos(\omega t + \phi_1^{\text{up}}) \right] dt \quad (3.16)$$

$$\bar{v}_C^{\text{low}} = \frac{1}{C_{SM}} \int_0^T \left[ (1 - d^{\text{low}}) \bar{i}_{L^{\text{low}}} + \frac{1}{2} i_0^{\text{low}} + \frac{1}{2} \hat{i}_1^{\text{low}} m \cos(\omega t) \cos(\omega t + \phi_1^{\text{low}}) \right] dt \quad (3.17)$$

The sign  $\wedge$  denotes the magnitudes. Since the average voltage of capacitors must be constant in periodic steady state, the dc component of each integrand must be equal to zero; thus:

$$(1 - d^{\text{up}})\bar{i}_L^{\text{up}} + \frac{1}{2}i_0^{\text{up}} - \frac{1}{4}\hat{i}_1^{\text{up}}m \cos(\phi_1^{\text{up}}) = 0 \quad (3.18)$$

$$(1 - d^{\text{low}})\bar{i}_L^{\text{low}} + \frac{1}{2}i_0^{\text{low}} + \frac{1}{4}\hat{i}_1^{\text{low}}m \cos(\phi_1^{\text{low}}) = 0 \quad (3.19)$$

When zero average power is drawn from the dc link, the dc component of the arm current is zero (i.e.,  $i_0^{\text{up}} = i_0^{\text{low}} = 0$ ). Hence from (3.18) and (3.19) it is concluded that the power supplied by the batteries is transferred to the fundamental component of the arm current. With the assumption of a purely sinusoidal output ac current, the fundamental component of the arm current is a combination of half of the ac line current and fundamental frequency circulating current denoted as  $i_1^{\text{circ}}$  and the ac output line current as denoted by  $i_s$ :

$$i_1^{\text{up}} = \frac{i_s}{2} + i_1^{\text{circ}} \quad (3.20)$$

$$i_1^{\text{low}} = -\frac{i_s}{2} + i_1^{\text{circ}} \quad (3.21)$$

As the output current is purely sinusoidal, any other harmonic component in the arm currents does not enter the ac line; they circulate within the MMC causing losses. The  $n^{\text{th}}$  order circulating current is represented as  $i_n^{\text{circ}}$ . Therefore, the arm currents can be represented in general as follows:

$$i^{\text{up}} = \frac{i_s}{2} + \sum_{n=1}^{\infty} i_n^{\text{circ}} \quad (3.22)$$

$$i^{\text{low}} = -\frac{i_s}{2} + \sum_{n=1}^{\infty} i_n^{\text{circ}} \quad (3.23)$$

$$i_n^{\text{circ}} = \hat{i}_n^{\text{circ}} \cos(n\omega t + \phi_n^{\text{circ}}) \quad (3.24)$$

With the knowledge of the capacitor voltages from (3.14) and (3.15), the voltage developed by each arm can be expressed as:

$$v^{\text{up}} = Nm^{\text{up}} \frac{1}{C_{\text{SM}}} \int [(1 - d^{\text{up}}) \bar{i}_{\text{L}}^{\text{up}} + m^{\text{up}} i^{\text{up}}] dt \quad (3.25)$$

$$v^{\text{low}} = Nm^{\text{low}} \frac{1}{C_{\text{SM}}} \int [(1 - d^{\text{low}}) \bar{i}_{\text{L}}^{\text{low}} + m^{\text{low}} i^{\text{low}}] dt \quad (3.26)$$

### 3.1.3 EMT-Type Averaged-Value Model

Based on (3.25) and (3.26), the multivalve of the MMC-ES can be represented as a controlled voltage source (see Figure 3.3) and be directly embedded in an EMT simulator wherein ac and dc subsystems are modeled as well. The hybrid model shown in Figure 3.3 represents the MMC-ES multivalve with an averaged-value model that captures the low-frequency behavior of the converter without showing switching details.  $R_{\text{MV}}$  is the equivalent multivalve resistance from the conducting semiconductors. At a given instant,  $N$  switches (diode or IGBT) conduct in series for the multivalve; hence, with the assumption of nearly equal on-state resistance for diodes and IGBTs,  $R_{\text{MV}}$  is  $NR_{\text{on}}$  where  $R_{\text{on}}$  is the on-state resistance of the semiconductors.

The model in Figure 3.3 is computationally meritorious and combines the benefits of an AVM with the ability of an EMT simulator to model the external circuitry of the converter (i.e., ac- and dc-side networks and converter-level controls); it is suitable for system-level studies in which switching transients may be ignored. Moreover (3.5) and (3.11) (with respective modifications for considered phase and arm) can be used to evaluate the average battery current of the multivalve and the average capacitor voltage of the multivalve.



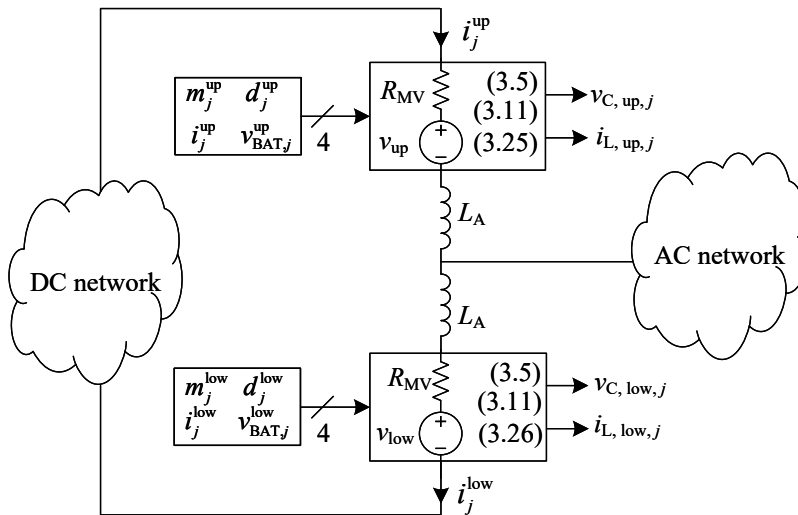


**Figure 3.3:** Averaged-value model of a multi-valve embedded in an EMT environment (single-phase view shown for brevity).

## 3.2 Analysis of Circulating Currents and Capacitor Voltage Ripple

The averaged-value model developed in section 3.1 is a low-order representative of the multi-valve in which switching-frequency details are ignored. When embedded in an EMT simulator as shown in Figure 3.3 it will create a voltage that is a function of the arm current as well as other variables shown in Figure 3.3. With simplifying assumptions about the nature of arm currents (in terms of harmonic components present in them), the AVM may be used as an entirely analytical model to describe the steady state operation of the converter without need for an EMT simulator. Such an explicit model readily enables analysis of circulating currents and average capacitor voltage ripple. The analysis can be done to include all harmonics of the circulating current or only its dominant components. This section presents a general model; then cases considering dominant second-order harmonic circulating current

and when the circulating current is suppressed are analyzed.

### 3.2.1 Circulating Currents in MMC-ES

Adding (3.25) and (3.26), and substituting for  $m_{\text{up}}$  and  $m_{\text{low}}$  from (3.7) and (3.8) yields (3.27).

$$\begin{aligned} \frac{2C_{\text{SM}}}{N}(v^{\text{up}} + v^{\text{low}}) &= \int [(1 - d^{\text{up}})\bar{i}_{\text{L}}^{\text{up}} + (1 - d^{\text{low}})\bar{i}_{\text{L}}^{\text{low}}] dt \\ &\quad - m \cos(\omega t) \int [(1 - d^{\text{up}})\bar{i}_{\text{L}}^{\text{up}} - (1 - d^{\text{low}})\bar{i}_{\text{L}}^{\text{low}}] dt \\ &\quad + \int (m^{\text{up}}i^{\text{up}} + m^{\text{low}}i^{\text{low}})dt - m \cos(\omega t) \int (m^{\text{up}}i^{\text{up}} - m^{\text{low}}i^{\text{low}})dt \end{aligned} \quad (3.27)$$

In steady state, the dc components of the integrands in (3.25) and (3.26) should separately be equal to zero:

$$\begin{aligned} \frac{1}{T} \int_0^T [(1 - d^{\text{up}})\bar{i}_{\text{L}}^{\text{up}} + m^{\text{up}}i^{\text{up}}] dt &= \frac{1}{T} \int_0^T \left[ (1 - d^{\text{up}})\bar{i}_{\text{L}}^{\text{up}} + \frac{(1 - m \cos(\omega t))}{2} \left( \frac{i_{\text{s}}}{2} + \sum_{n=1}^{\infty} i_n^{\text{circ}} \right) \right] dt \\ &= \frac{1}{T} \int_0^T \left[ (1 - d^{\text{up}})\bar{i}_{\text{L}}^{\text{up}} - \frac{mi_{\text{s}} \cos(\omega t)}{4} - \frac{mi_1^{\text{circ}} \cos(\omega t)}{2} \right] dt \\ &= (1 - d^{\text{up}})\bar{i}_{\text{L}}^{\text{up}} - \frac{m\hat{i}_{\text{s}} \cos \alpha}{8} - \frac{m\hat{i}_1^{\text{circ}} \cos \phi_1^{\text{circ}}}{4} = 0 \end{aligned} \quad (3.28)$$

Similarly for the lower arm:

$$\begin{aligned} \frac{1}{T} \int_0^T [(1 - d^{\text{low}})\bar{i}_{\text{L}}^{\text{low}} + m^{\text{low}}i^{\text{low}}] dt &= (1 - d^{\text{low}})\bar{i}_{\text{L}}^{\text{low}} - \frac{m\hat{i}_{\text{s}} \cos \alpha}{8} + \frac{m\hat{i}_1^{\text{circ}} \cos \phi_1^{\text{circ}}}{4} \\ &= 0 \end{aligned} \quad (3.29)$$

Subtracting (3.29) from (3.28) yields:

$$(1 - d^{\text{up}})\bar{i}_{\text{L}}^{\text{up}} - (1 - d^{\text{low}})\bar{i}_{\text{L}}^{\text{low}} = \frac{m\hat{i}_1^{\text{circ}} \cos \phi_1^{\text{circ}}}{2} \quad (3.30)$$

Equation (3.30) indicates that the unbalanced power from the upper and lower arms are balanced by the fundamental frequency circulating current. The fundamental frequency component exists without exchanging any active power when the phase angle  $\phi_1^{\text{circ}}$  is  $\pm 90^\circ$ . At this operating point, only reactive power is interchanged between arms. For evaluation of (3.27), the following simplifications are made using (3.7), (3.8), (3.22), (3.23), (3.29) and (3.30):

$$m^{\text{up}}i^{\text{up}} + m^{\text{low}}i^{\text{low}} = \sum_{n=1}^{\infty} i_n^{\text{circ}} - \frac{mi_s \cos(\omega t)}{2} \quad (3.31)$$

$$m^{\text{up}}i^{\text{up}} - m^{\text{low}}i^{\text{low}} = \frac{i_s}{2} - m \cos(\omega t) \sum_{n=1}^{\infty} i_n^{\text{circ}} \quad (3.32)$$

$$(1 - d^{\text{up}})\bar{i}_{\text{L}}^{\text{up}} + (1 - d^{\text{low}})\bar{i}_{\text{L}}^{\text{low}} = \frac{m\hat{i}_s \cos \alpha}{4} \quad (3.33)$$

Substituting (3.30), (3.31), (3.32), and (3.33) in (3.27) yields:

$$\begin{aligned} \frac{2C_{\text{SM}}}{N}(v^{\text{up}} + v^{\text{low}}) &= \int \frac{m\hat{i}_s}{4} \cos \alpha dt - m \cos(\omega t) \int \frac{m\hat{i}_1^{\text{circ}}}{2} \cos \phi_1^{\text{circ}} dt \\ &+ \int \left( \sum_{n=1}^{\infty} i_n^{\text{circ}} - \frac{mi_s \cos(\omega t)}{2} \right) dt - m \cos(\omega t) \int \left( \frac{i_s}{2} - m \cos(\omega t) \sum_{n=1}^{\infty} i_n^{\text{circ}} \right) dt \end{aligned} \quad (3.34)$$

An extended evaluation of the harmonic contents of the phase voltage is done in [59] for a regular MMC, i.e., one with no battery energy storage in the SMs. The same procedure can be extended to MMC-ES using (3.34). This process shows that including only the second-order harmonic in the circulating current of the MMC is sufficient, as higher order

harmonics often have much smaller magnitudes. Existence of the fundamental frequency circulating current can also be ignored due to the balanced operation of battery modules in steady state.

### 3.2.2 Second Harmonic Circulating Current

With the assumption of only second-order circulating current in the arms, (3.22) and (3.23) may be written as:

$$i^{\text{up}} = \frac{1}{2} \cos(\omega t + \alpha) + \hat{i}_2^{\text{circ}} \cos(2\omega t + \phi_2^{\text{circ}}) \quad (3.35)$$

$$i^{\text{low}} = -\frac{1}{2} \cos(\omega t + \alpha) + \hat{i}_2^{\text{circ}} \cos(2\omega t + \phi_2^{\text{circ}}) \quad (3.36)$$

Evaluating (3.11) for the upper arm yields:

$$\begin{aligned} v_C^{\text{up}} &= \frac{1}{C_{\text{SM}}} \int \left[ \begin{aligned} &(1 - d^{\text{up}}) \bar{i}_L^{\text{up}} \\ &+ 0.5(1 - m \cos(\omega t))(-0.5 \hat{i}_s \cos(\omega t + \alpha) + \hat{i}_2^{\text{circ}} \cos(2\omega t + \phi_2^{\text{circ}})) \end{aligned} \right] dt \\ &= \frac{1}{C_{\text{SM}}} \int \left[ \begin{aligned} &(1 - d^{\text{up}}) \bar{i}_L^{\text{up}} + \frac{\hat{i}_s}{4} \cos(\omega t + \alpha) + \frac{\hat{i}_2^{\text{circ}}}{2} \cos(2\omega t + \phi_2^{\text{circ}}) \\ & - \frac{m \hat{i}_s}{8} [\cos(2\omega t + \alpha) + \cos \alpha] - \frac{m \hat{i}_2^{\text{circ}}}{4} [\cos(3\omega t + \phi_2^{\text{circ}}) + \cos(\omega t + \phi_2^{\text{circ}})] \end{aligned} \right] dt \end{aligned} \quad (3.37)$$

For steady state operation, the dc terms cancel out. Thus:

$$(1 - d^{\text{up}}) \bar{i}_L^{\text{up}} = \frac{m \hat{i}_s \cos \alpha}{8} \quad (3.38)$$

Considering the ripple component of (3.37) and evaluating the integral with zero initial conditions yields:

$$\Delta v_C^{\text{up}} = \frac{1}{C_{\text{SM}}} \left[ \begin{aligned} & \frac{\hat{i}_s}{4\omega} \sin(\omega t + \alpha) + \frac{\hat{i}_2^{\text{circ}}}{4\omega} \sin(2\omega t + \phi_2^{\text{circ}}) - \frac{m\hat{i}_s}{16\omega} \sin(2\omega t + \alpha) \\ & - \frac{m\hat{i}_2^{\text{circ}}}{12\omega} \sin(3\omega t + \phi_2^{\text{circ}}) - \frac{m\hat{i}_2^{\text{circ}}}{4\omega} \sin(\omega t + \phi_2^{\text{circ}}) \end{aligned} \right] \quad (3.39)$$

Similarly

$$\Delta v_C^{\text{low}} = \frac{1}{C_{\text{SM}}} \left[ \begin{aligned} & -\frac{\hat{i}_s}{4\omega} \sin(\omega t + \alpha) + \frac{\hat{i}_2^{\text{circ}}}{4\omega} \sin(2\omega t + \phi_2^{\text{circ}}) - \frac{m\hat{i}_s}{16\omega} \sin(2\omega t + \alpha) \\ & + \frac{m\hat{i}_2^{\text{circ}}}{12\omega} \sin(3\omega t + \phi_2^{\text{circ}}) + \frac{m\hat{i}_2^{\text{circ}}}{4\omega} \sin(\omega t + \phi_2^{\text{circ}}) \end{aligned} \right] \quad (3.40)$$

From (3.39) and (3.40), it is seen that the capacitor voltage ripple waveforms contain fundamental frequency ( $v_1$ ), second-order ( $v_2$ ), and third-order ( $v_3$ ) harmonics with only the second-order circulating currents present in the converter arms. An equation for the dc link voltage can be written with these expressions:

$$2V_{\text{dc}} = Nm^{\text{up}}\bar{v}_C^{\text{up}} + Nm^{\text{low}}\bar{v}_C^{\text{low}} + v_{2L} \quad (3.41)$$

$$2V_{\text{dc}} = N \frac{(1 - m \cos(\omega t))}{2} (V_{\text{dc}} + v_1 + v_2 + v_3) + N \frac{(1 + m \cos(\omega t))}{2} (V_{\text{dc}} - v_1 + v_2 - v_3) + v_{2L} \quad (3.42)$$

where

$$v_1 = \frac{\hat{i}_s}{4\omega C_{\text{SM}}} \sin(\omega t + \alpha) - \frac{m\hat{i}_2^{\text{circ}}}{4\omega C_{\text{SM}}} \sin(\omega t + \phi_2^{\text{circ}}) \quad (3.43)$$

$$v_2 = \frac{\hat{i}_2^{\text{circ}}}{4\omega C_{\text{SM}}} \sin(2\omega t + \phi_2^{\text{circ}}) - \frac{m\hat{i}_s}{16\omega C_{\text{SM}}} \sin(2\omega t + \alpha) \quad (3.44)$$

$$v_3 = -\frac{m\hat{i}_2^{\text{circ}}}{12\omega C_{\text{SM}}} \sin(3\omega t + \phi_2^{\text{circ}}) \quad (3.45)$$

In (3.41)  $v_{2L}$  is the voltage drop across the arm inductors due to the second-order circulating current. Simplifying (3.42) yields:

$$v_{2L} = Nm \cos(\omega t)(v_1 + v_3) - Nv_2 \quad (3.46)$$

Considering only the 2<sup>nd</sup> harmonic component:

$$v_{2L} = \frac{3Nm\hat{i}_s}{16\omega C_{SM}} \sin(2\omega t + \alpha) - \left( \frac{2Nm^2 + 3N}{12\omega C_{SM}} \right) \hat{i}_2^{\text{circ}} \sin(2\omega t + \phi_2^{\text{circ}}) \quad (3.47)$$

The second harmonic voltage across the arm inductors is:

$$v_{2L} = 2L_A \frac{d}{dt} \hat{i}_2^{\text{circ}} \cos(2\omega t + \phi_2^{\text{circ}}) = -4L_A \omega \hat{i}_2^{\text{circ}} \sin(2\omega t + \phi_2^{\text{circ}}) \quad (3.48)$$

Equating (3.47) and (3.48) yields:

$$\hat{i}_2^{\text{circ}} \sin(2\omega t + \phi_2^{\text{circ}}) = \frac{\frac{9}{4}Nm\hat{i}_s}{(2Nm^2 + 3N - 48L_A\omega^2 C_{SM})} \sin(2\omega t + \alpha) \quad (3.49)$$

Therefore, the second harmonic circulating current component can be expressed as follows:

$$\hat{i}_2^{\text{circ}} = \frac{\frac{9}{4}Nm\hat{i}_s}{(2Nm^2 + 3N - 48L_A\omega^2 C_{SM})} \quad (3.50)$$

$$\phi_2^{\text{circ}} = \alpha \quad (3.51)$$

Note that when the denominator of (3.50) is zero, a resonant condition may occur resulting in excessively large 2<sup>nd</sup> harmonic circulating currents. To avoid this undesirable condition, the MMC-ES parameters must satisfy:

$$(2m^2 + 3)N > 48L_A\omega^2C_{SM} \quad (3.52)$$

### 3.2.3 Circulating Current Suppression Control (CCSC)

When the second harmonic circulating current in the arm is suppressed the arm currents only contain half of the ac current.

$$i^{\text{up}} = 0.5\hat{i}_s \cos(\omega t + \alpha) \quad (3.53)$$

$$i^{\text{low}} = -0.5\hat{i}_s \cos(\omega t + \alpha) \quad (3.54)$$

For elimination of the second harmonic component, the arm modulation waveforms are augmented with a signal  $m_z(t)$ , which is generated by the circulating current suppression controller:

$$m^{\text{up}} = \frac{1}{2}(1 - m_{\text{ref}} - m_z) \quad (3.55)$$

$$m^{\text{low}} = \frac{1}{2}(1 + m_{\text{ref}} - m_z) \quad (3.56)$$

Substituting (3.53)-(3.56) in (3.11) yields:

$$\Delta\bar{v}_C^{\text{up}} = \frac{1}{C_{SM}} \left[ \frac{\hat{i}_s}{4\omega} \sin(\omega t + \alpha) - \frac{m\hat{i}_s}{16\omega} \sin(2\omega t + \alpha) \right] \quad (3.57)$$

$$\Delta\bar{v}_C^{\text{low}} = \frac{1}{C_{SM}} \left[ -\frac{\hat{i}_s}{4\omega} \sin(\omega t + \alpha) - \frac{m\hat{i}_s}{16\omega} \sin(2\omega t + \alpha) \right] \quad (3.58)$$

Note that fundamental and 2<sup>nd</sup> harmonic components are generated in the capacitor ripple voltage. Since  $0 \leq m \leq 1$  the fundamental component of the capacitor voltage ripple

is at least four times larger than the 2<sup>nd</sup> harmonic component.

### 3.3 Evaluation of the Averaged-Value Model

#### 3.3.1 Evaluation against Detailed EMT Simulation Models

To validate the developed AVM, a switching model of a three-phase MMC-ES along with its full control circuitry is constructed in PSCAD/EMTDC simulator. Another EMT model is also built with the AVM replacing the multivalves (similar to Figure 3.3). The results of detailed model (DM) are used as the benchmark for validation of the AVM. Converter parameters are shown in Table 3.1. Simulation time-steps for both the detailed and averaged-value models are 10  $\mu$ s.

**Table 3.1:** Parameters of the simulated MMC-ES

Description	Value	Description	Value
Power rating	0.5 MW	SM inductance ( $L_{SM}$ )	7.815 mH
Converter ac voltage (line-to-line)	2.75 kV	Battery voltage ( $v_{BAT}$ )	292 V
Grid voltage (line-to-line)	24.9 kV	Arm inductance ( $L_A$ )	5.031 mH
DC link voltage	5 kV	SM capacitance ( $C_{SM}$ )	4840 $\mu$ F
Number of SMs per arm	10	Grid short circuit ratio (SCR)	4/75°
Grid-side transformer: 0.6 MVA, 2.75 kV : 24.9 kV, 18%			

In both simulations the converter is operated to steady state with a power reference of 0.5 pu and without CCSC. The power set-point is raised to 1.0 pu at  $t = 0.25$  s, followed by activation of the CCSC at  $t = 0.5$  s. The power reference is reduced to 0.5 pu at  $t = 0.75$  s. Simulation results are shown in Figures 3.4 - 3.10.



The results clearly show that the AVM conforms well with the fully-detailed EMT model except for the very fast transients and switching details that are both ignored in the development of the AVM. Figure 3.4 shows the power distribution in the converter. The power outputs are perfectly captured by the two models. Slight differences between the two models are seen at the onset of CCSC at  $t = 0.5$  s. Figures 3.5 and 3.6 also show well-conforming results for ac current and voltage. Figure 3.7 shows that when the CCSC is activated, the arm current becomes essentially sinusoidal, thus validating the assumptions in section 3.2.3. Capacitor voltage waveforms in Figure 3.8 show that with the increase in the power set-point, the ripple increases as expected. With CCSC the ripple reduces due to the removal of the second-order circulating current. Figure 3.9 shows that the battery current increases sharply when the power command is changed. This is due to the power command feedforward applied to the dc-dc converter control system. As a result, even with large power command increments, capacitor voltages are marginally affected. This effect can be clearly seen in Figure 3.10 in the ac voltage at PCC, which shows small variations as the power command changes.

Figure 3.11 shows the effect of simulation time-step on the capacitor voltage. It is seen that considerably larger time-steps could be used to simulate the steady state characteristics of the MMC-ES with the AVM. The transients due to controller command change (at  $t = 0.75$  s) are perfectly captured even with time-steps as large as  $70 \mu\text{s}$ ; some deviations are observed when CCSC is turned on at  $t = 0.5$  s. Thus the AVM is computationally efficient in controller tuning and optimization studies [60] that need a large number of simulation.

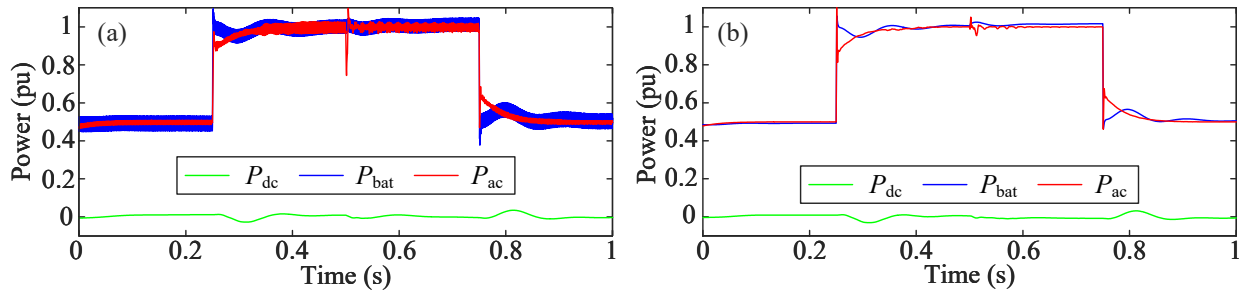


Figure 3.4: Power flow within the MMC-ES (a) detailed model (b) AVM.

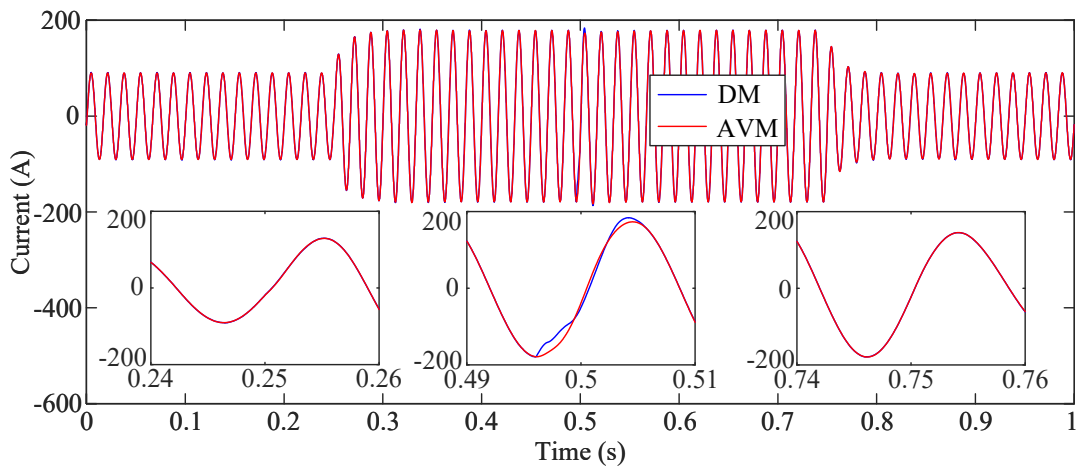


Figure 3.5: AC current from the converter.

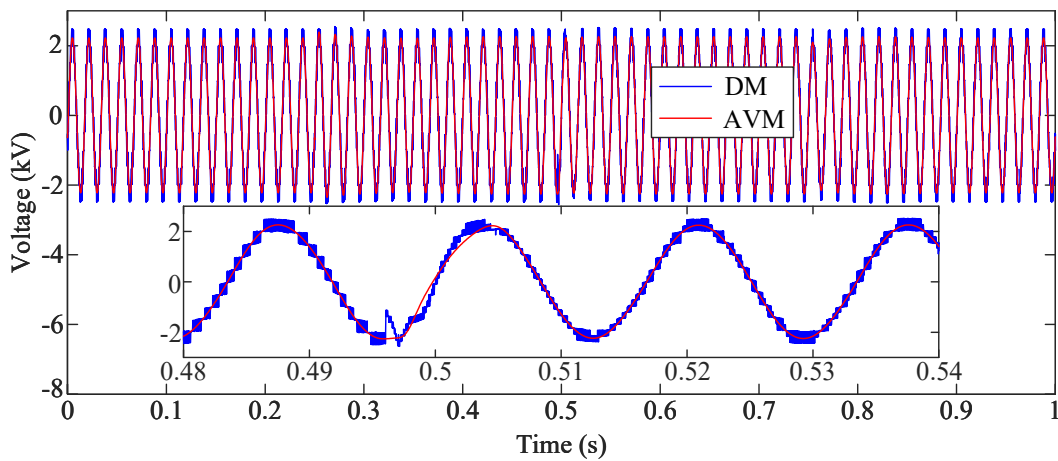
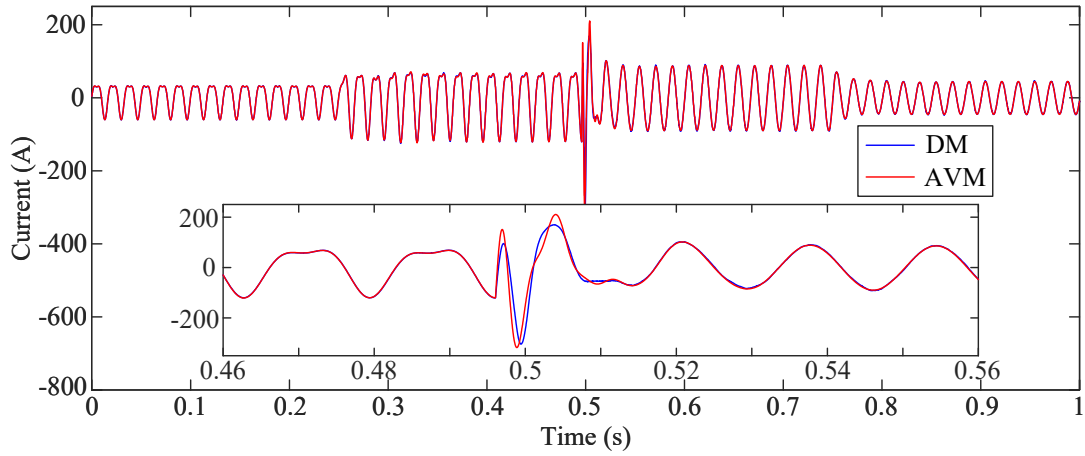
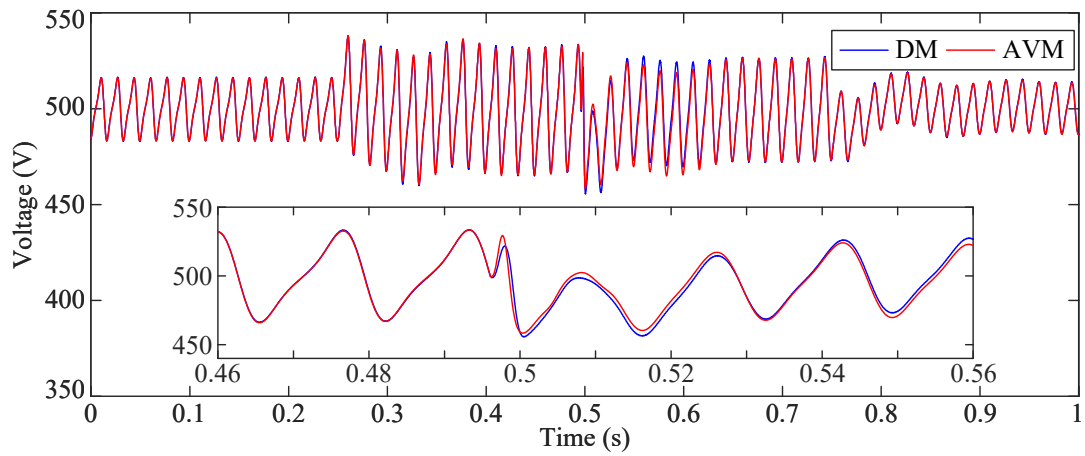


Figure 3.6: AC voltage at converter terminal.



**Figure 3.7:** Phase-a, upper arm current.



**Figure 3.8:** Average capacitor voltage of phase-a, upper arm.

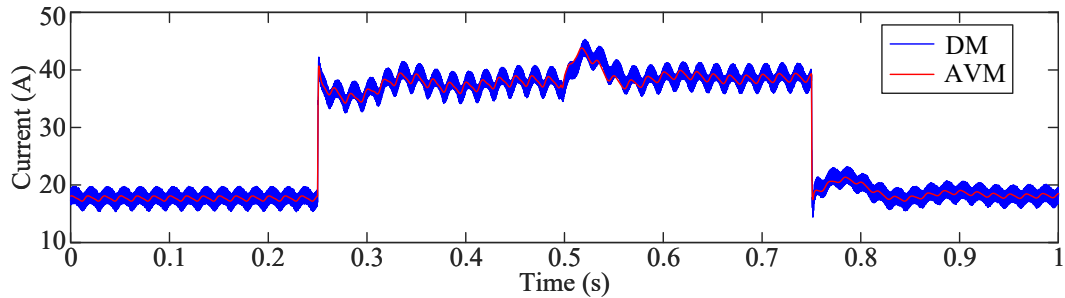


**Figure 3.9:** Average battery current of phase-a, upper arm.

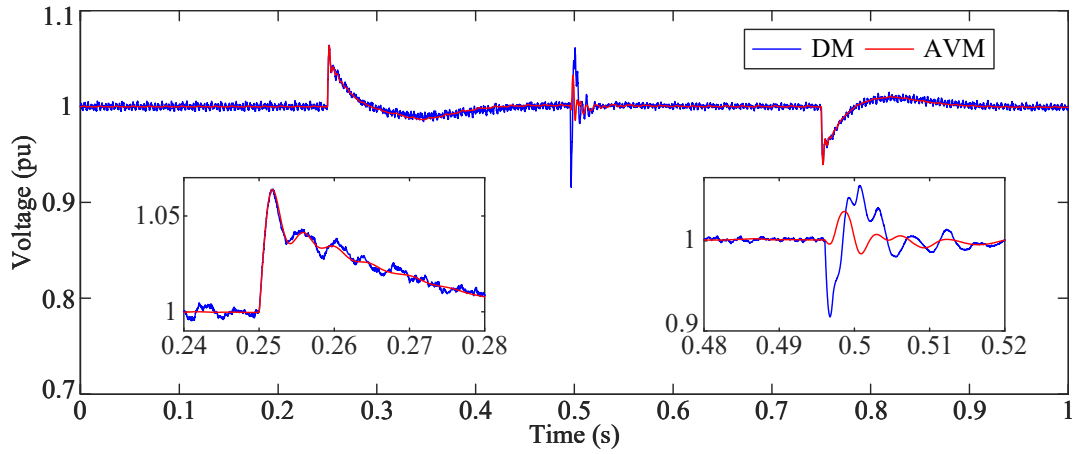


**Figure 3.10:** AC-side rms voltage.

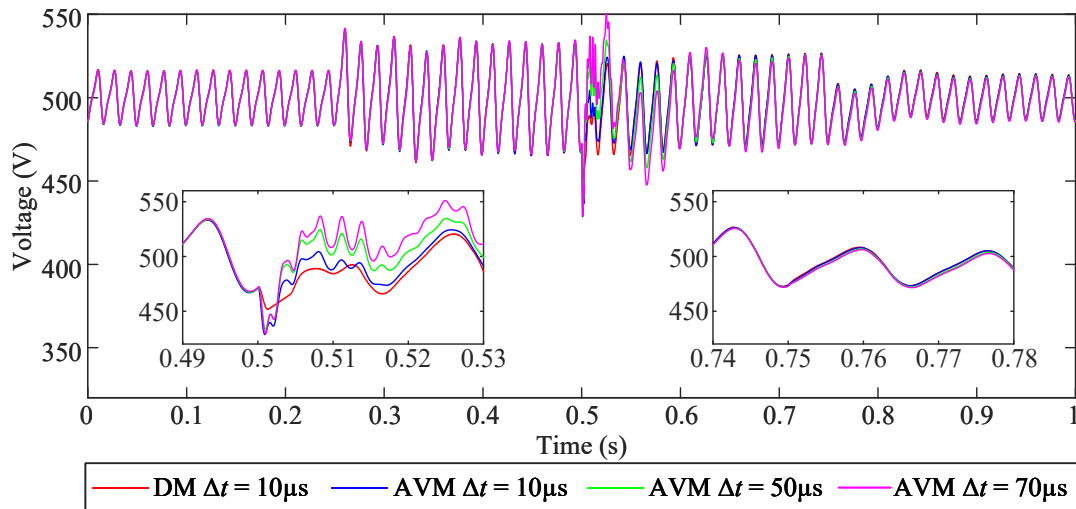


**Figure 3.11:** Effect of simulation time step for AVM (for average capacitor voltage).

The developed AVM ignores PWM details and individual SM information. It is useful for controller tuning, and large-scale system simulation with a focus on the average behavior of the converter. The AVM has a considerable simulation time efficiency compared to the detailed model. To simulate the considered three-phase MMC-ES for 5 s with a 10  $\mu$ s time

step, the detailed EMT model takes 1125.5 s while the AVM only needs 34.14 s, showing a gain of more than 30 times.

### 3.3.2 Evaluation of Behaviour under AC System faults

A remote fault is simulated using both the DM and AVM. The fault is emulated with a reduction of the magnitude of the ac grid voltage by 25% for 50 ms at  $t = 0.1$  s and changing its phase  $10^\circ$  for 50 ms at  $t = 0.6$  s. In Figures 3.12 - 3.14 the converter's ac current, average capacitor voltage, and average battery current are shown. It is seen that dynamics in the waveforms are well captured during both the ac voltage magnitude and phase angle changes of the ac voltage.

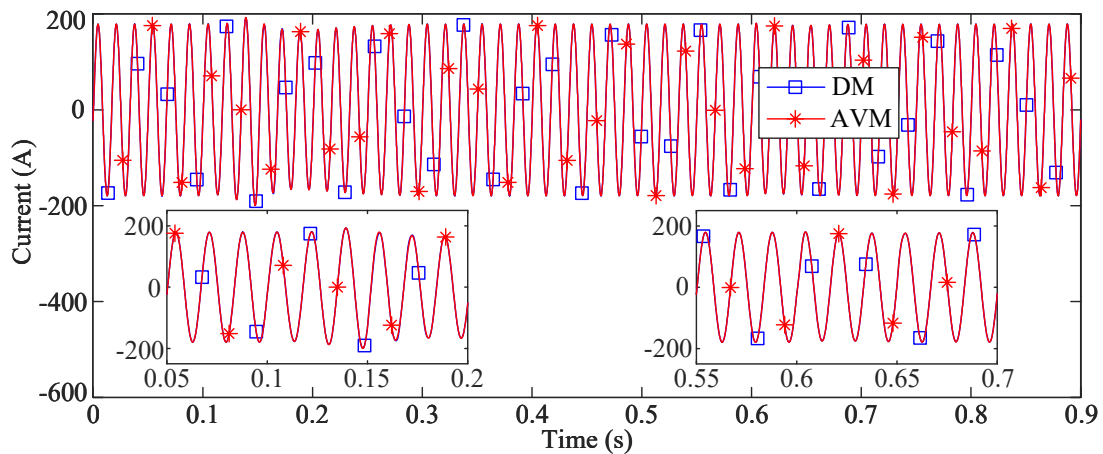


**Figure 3.12:** AC current waveform during remote fault test.

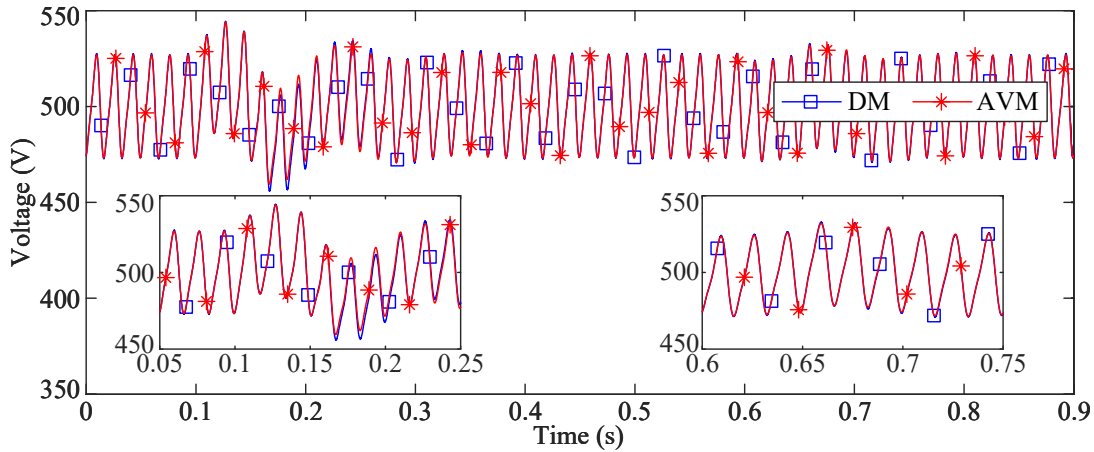


**Figure 3.13:** Average capacitor voltage during remote fault test.

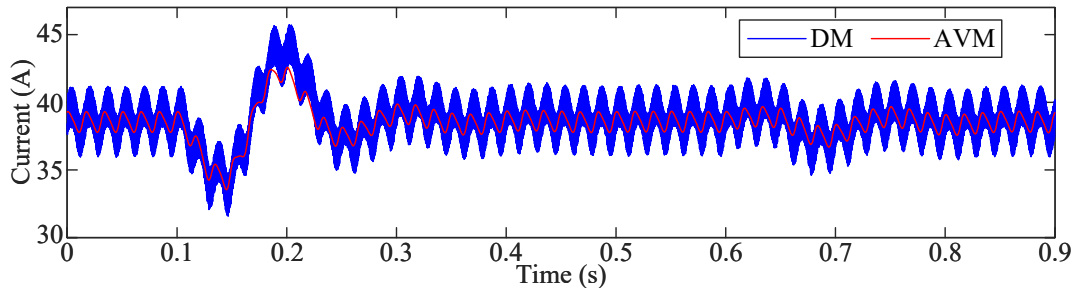


**Figure 3.14:** Average battery current during remote fault test.

### 3.3.3 Verification against Experimental Results

The AVM is also evaluated against experimental results on a prototype single-phase MMC-ES [22], shown in Figure 3.15, with parameters given in Table 3.2. The control system is implemented in the RTDS real time simulator and firing pulses are issued using the digital output modules available in RTDS. Capacitor voltage ripple is evaluated using (3.39) and (3.40) for operation with  $m = 0.9$  and a load resistance of  $15.4\Omega$ . Figure 3.16 shows a comparison of the average capacitor voltages from the AVM and those measured experimentally. The experimental ripple agrees well with the AVM predictions.

**Table 3.2:** Parameters of the MMC-ES prototype

Description	Value	Description	Value
Power rating	300 W	SM inductance	700 $\mu$ H
Converter ac voltage	25 V	Battery voltage	12 V
DC link voltage	80 V	Arm inductance	3.37 mH
Number of SMs per arm	4	Load resistance	10.1 $\Omega$ /15.4 $\Omega$
SM capacitance	4700 $\mu$ F	Load inductance	6.71 mH
DC-DC switching frequency	15 kHz	RTDS time step	5 $\mu$ s

Capacitor ripple is analyzed with varying modulation index and load resistance, as shown in Figure 3.17. The AVM generally agrees well with both EMT simulations and experimental measurements. The small discrepancies observed are chiefly due to the high-frequency circulating current components that are not included in the AVM but exist in the prototype and are accounted for in the detailed EMT model. Figure 3.17 shows two sets of results from the AVM: one labelled ‘AVM simulation’, in which the AVM is used in a simulation model of the prototype converter, and one labelled ‘calculation’ using analytical calculations with the AVM with the assumption of only second-order circulating currents (see section 3.2).

### 3.3.4 Limitations of the AVM

From the simulation and analytical calculations presented in this section, it is observed that the AVM is able to predict steady state behavior and low-frequency variations, such as power reference command changes, accurately. Due to the averaging process, information such as individual SM capacitor voltages and battery currents are lost. Using AVM in long-run simulations such as SOC balancing are advantageous due to its simplicity and low computational

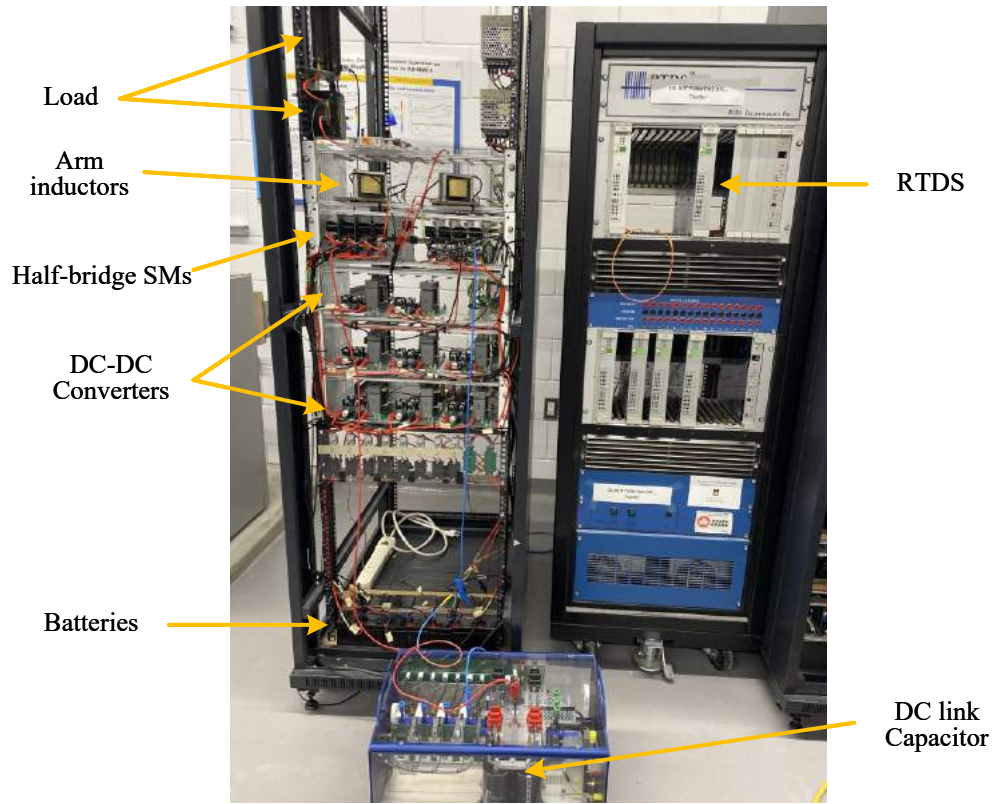


Figure 3.15: Prototype setup.

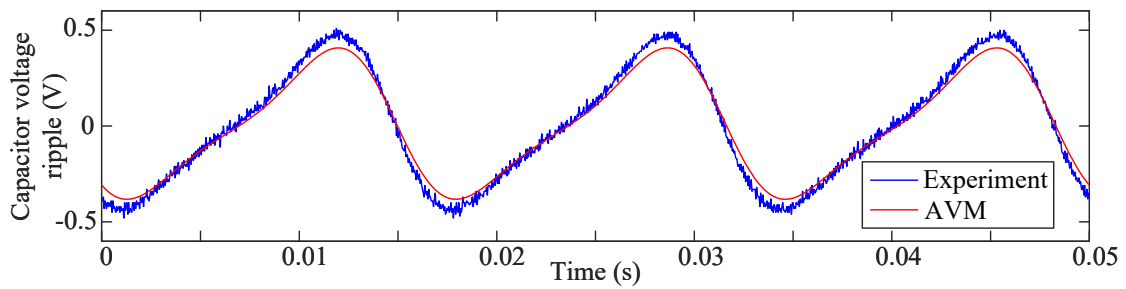
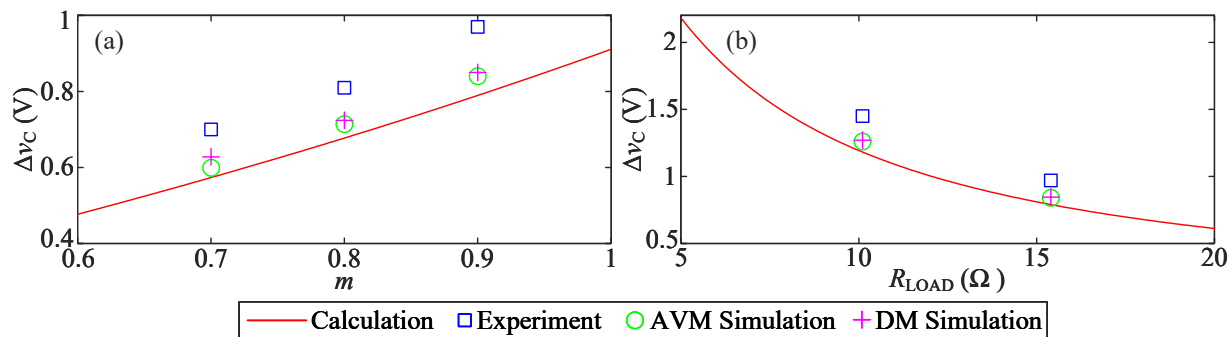


Figure 3.16: Capacitor voltage ripple (dc offset removed for clarity).





**Figure 3.17:** Capacitor voltage ripple variations with different parameters (a) modulation index, and (b) load resistance.

load. The AVM has the capability of simulating some faults with reasonable accuracy, but has limitations in simulating solid faults, startup sequence, blocking and controller starting transients, and other transients that may cause discontinuous conduction operation of the SM dc-dc converters. However, such transients are small in duration and need to be implemented in detailed simulations to observe individual quantities.

### 3.4 Modelling and Balancing SOC

The battery voltage is used in evaluating the SM inductor current (battery current) in (3.5) as a variable. The battery voltage can be modeled as a function of the SOC based on different battery models [61]. In this work, the Shepherd's model is used, and implemented as outlined in [58] in an EMT environment. Figure 3.18 shows a functional block diagram of the battery voltage evaluation based on battery current. In this figure,  $Q$  is the used charge of the battery. Since an average SM capacitor voltage and SM inductor current are simulated in AVM, the SOC is also evaluated for the average SOC of a multivalve of the MMC-ES.

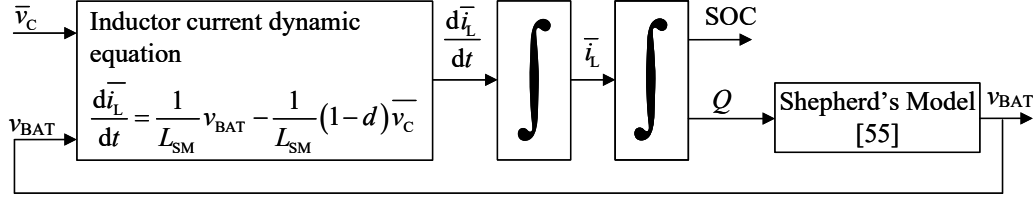


**Figure 3.18:** Block diagram for battery voltage evaluation.

During normal operation, the batteries need to be charged/discharged uniformly. Power can be transferred within phases and among phase arms by introducing small dc and fundamental-frequency circulating currents [25]. Figure 3.19 shows a block diagram of the SOC balancing controller for the MMC-ES. In this diagram,  $SOC_{\text{BESS}}$  is the average SOC of MMC-ES,  $SOC_j$  is the average SOC of phase,  $SOC_j^k$  is the average SOC of a phase arm and  $SOC_{j,i}^k$  is the individual SM battery SOC where  $j \in \{a, b, c\}$ ,  $k \in \{\text{up, low}\}$ , and  $i \in \{1 \dots N\}$  represents SM number.  $i_j^{\text{circ}}$  is the circulating current in phase  $k$ , and  $\alpha, \beta, \gamma$  are constant gains.

The effect of the SOC controller is depicted in Figure 3.20. The ac power command is changed as indicated. It can be observed that both AVM and DEM produce identical results in estimating the SOC. It should be noted that the energy capacity in the MMC-ES is chosen to be low so that considerable SOC drop happens within a reasonable time. When the power reference is higher, faster variations in SOC can be observed as expected. After the discharging and charging process, the SOC does not return to 100% as some resistive power losses occur.

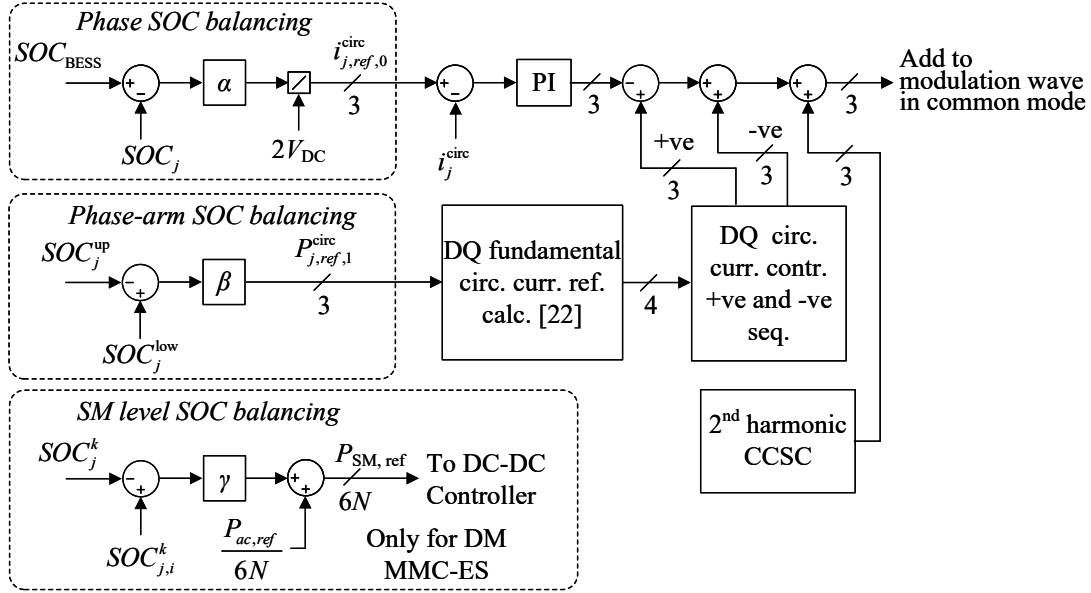


Figure 3.19: SOC balancing controller.

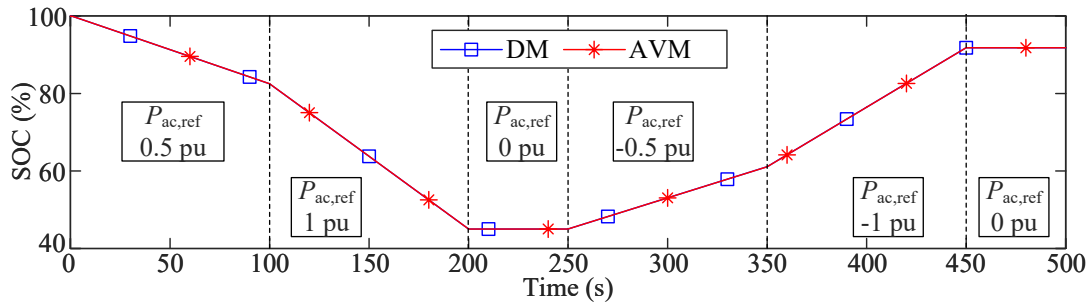
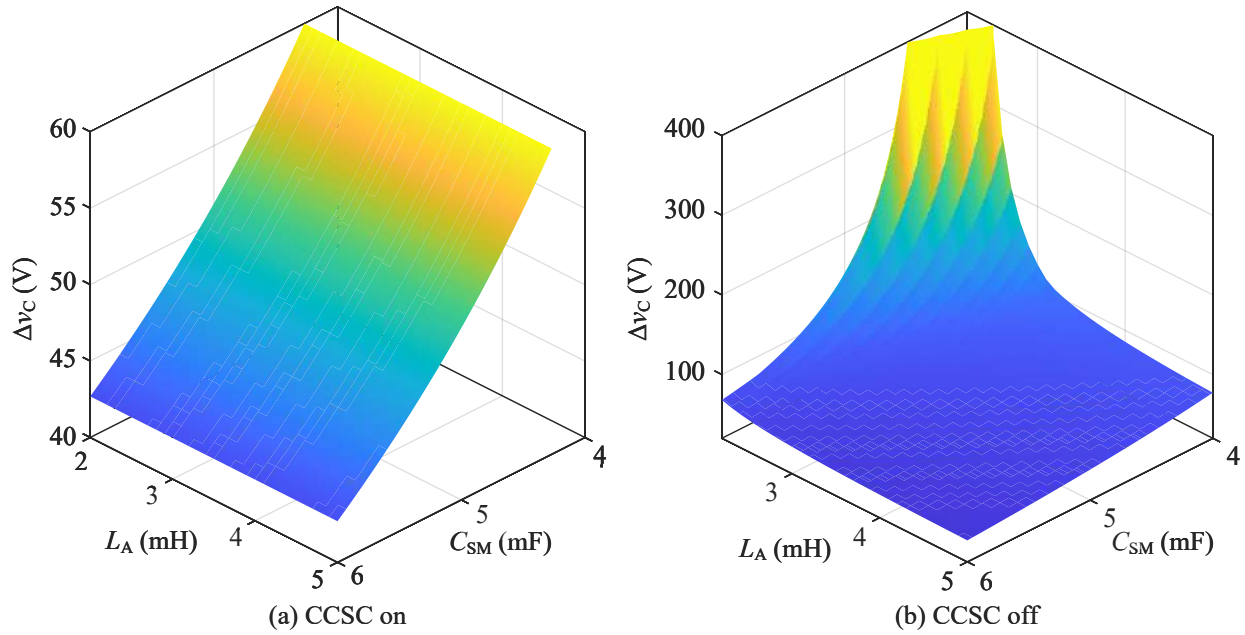


Figure 3.20: Variation of converter SOC.

### 3.5 Selection of Converter Parameters

For proper operation, converter parameters must be selected to reduce circulating currents and capacitor voltage ripple. Large circulating currents increase conduction losses and take up the current capacity of the switches. Equations (3.39)-(3.40), (3.50)-(3.51), and (3.57)-



**Figure 3.21:** Capacitor voltage ripple (a) CCSC on (b) CCSC off.

(3.58) describe the capacitor ripple and circulating current of the MMC-ES, and can be used to determine the SM capacitance and arm inductance. Figure 3.21 shows the variation of the capacitor voltage ripple with different  $L_A$  and  $C_{SM}$  values. The variation of second harmonic circulating current is shown in Figure 3.22. This evaluation has been done for the MMC-ES whose parameters are given in Table 3.1, but may be readily repeated for other parameter values.

Figures 3.21 and 3.22 show that for certain values of  $L_A$  and  $C_{SM}$  the second-order circulating current magnitude becomes excessively large, thereby also resulting in high capacitor voltage ripples. This occurs when the denominator of (3.50) approaches zero. It is observed that the denominator is a function of converter parameters ( $L_A$ ,  $C_{SM}$ ,  $N$ ) as well as operating point ( $m$  and  $\omega$ ). In power system applications  $m$  and  $\omega$  do not vary drastically. It cannot be guaranteed that use of a second-order harmonic suppression controller can avoid the reso-

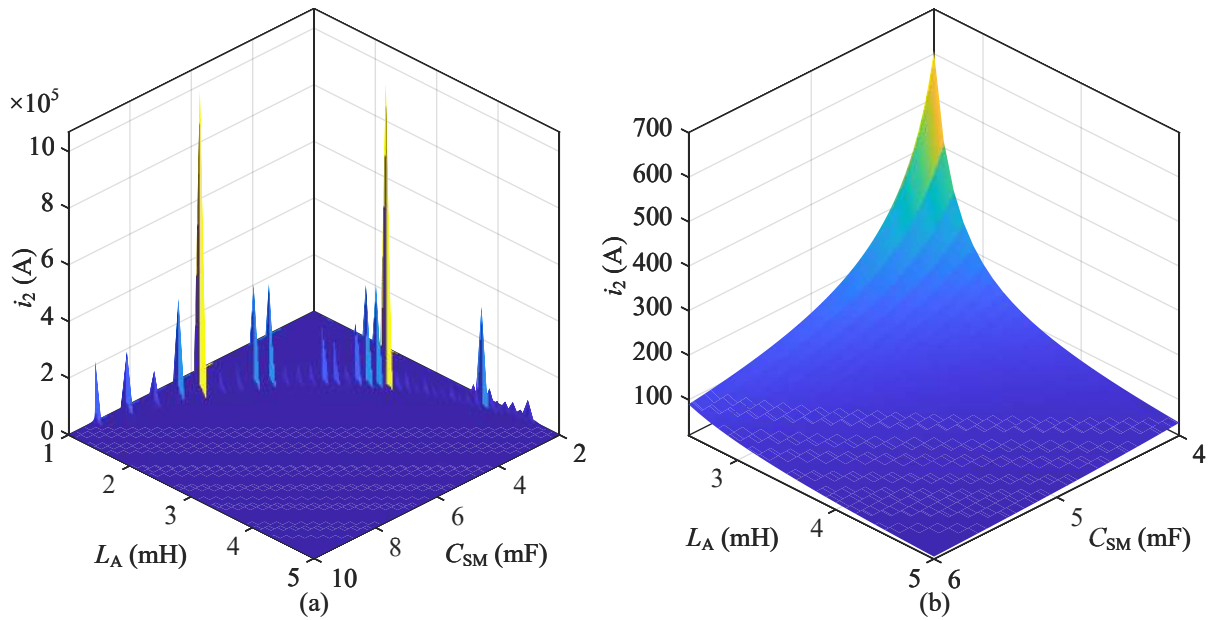


**Figure 3.22:** Second-order circulating current (a) large range (b) zoomed-in view.

nant conditions, due to small steady state errors and other harmonic contents available in the system. Selecting converter parameters adequately far from these resonant points provides safe margins and further attenuates higher order harmonics. However, large capacitors and inductors adversely affect the dynamic response of the converter, draw high inrush currents, and increase the cost. These trade-offs need to be considered when selecting components.

Figure 3.23 shows capacitor voltage ripple variations with respect to the modulation index, converter load, and arm inductance. The figure shows the voltage ripple for two capacitor values. Simulated converter ripple using AVM and detailed EMT models are also plotted against the theoretically calculated values with and without CCSC. Figures 3.23(a)-(b) show that the simulated capacitor ripple agrees well with the calculated values. As expected the ripple increases with the increase in modulation index. Figures 3.23(c)-(d) show that with increasing load on the converter, the ripple increases. This is expected as the arm

current increases and results in high charging and discharging of the SM capacitors. Variation of the ripple with the arm inductance is shown in Figures 3.23(e)-(f). It is observed that the theoretical ripple values slightly deviate from the simulated values at low arm inductance values. This is due to higher order circulating currents that are generated when the arm inductance is small but are ignored in the AVM. Theoretical calculation can be extended to include higher order harmonics when using particularly low arm inductance values.

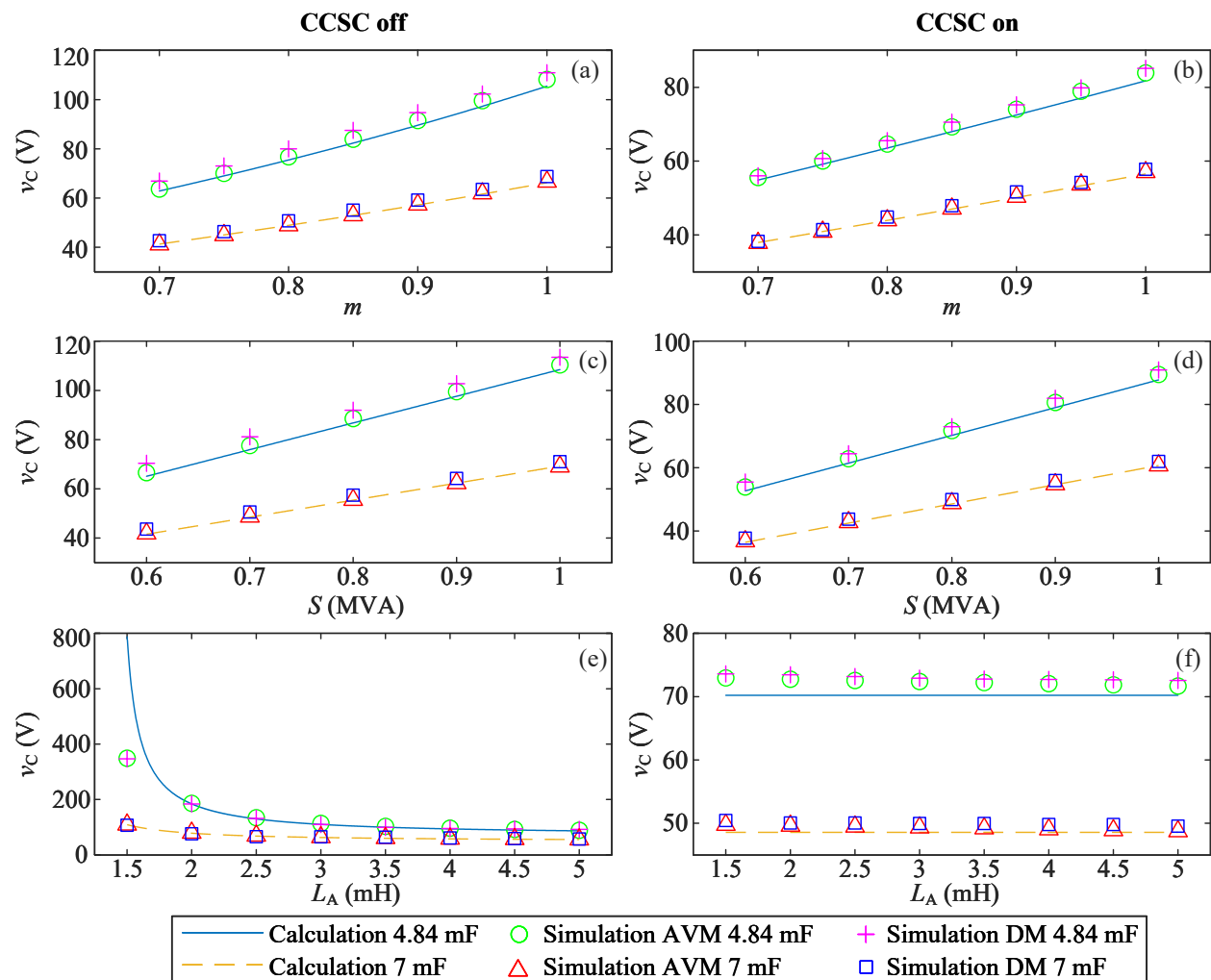


**Figure 3.23:** Variation of capacitor voltage ripple versus (a-b)  $m$ , (c-d) load magnitude (PF = 0.95 lag), (e-f) arm inductance.

## 3.6 Summary

This chapter developed a novel AVM for the multivalve of a modular multilevel converter with SM-level battery energy storage. The AVM considers low-frequency dynamics of the multivalve and ignores switching details. The chapter showed the application of the AVM as a replacement for a conventional detailed switching model for system-level studies, and its use as an analytical tool for the study of steady state behavior of the converter and for component sizing. The AVM was validated against detailed simulation results (which also confirmed its computational advantage), and results obtained on a laboratory-scale converter prototype. The work presented in this chapter are published in [62].

## Chapter 4

# Improvements on EMT Simulation Models of MMC-ES

### 4.1 Introduction

Electromagnetic transient (EMT) simulations are conducted to study MMC-ES systems under normal and faulted conditions. The large number of passive and switching elements in an MMC-ES results in extremely large admittance matrices that the EMT solver needs to invert every time a switching occurs [36]. This results in prohibitive levels of computational complexity rendering conventional EMT modeling and solution methods impractical for systems that include MMC-ES. Alternative approaches have been developed to reduce the simulation complexity of MMC systems. Most existing simulation models consider regular MMCs, i.e., with no embedded storage, with half-bridge or full-bridge SMs. The model proposed in [35] suggests an averaged-value model for a regular MMC with voltage sources at each arm. This model has been proved to be sufficient in simulating steady state operations and



limited types of faults. Converter blocking is not properly modeled and, hence, converter startup and blocking during faults are not possible to be studied. An improvement for this model is proposed in [38] where converter blocking and dc faults can be accurately modeled. However in both these models the converter capacitors' dynamics are modeled using a single equivalent capacitor in the dc link, which necessitate special topological changes (i.e., changes in the current flow paths using router switches). There are other models for regular MMCs at the phase level with much simplicity [33, 63] where each phase is modeled by a single voltage source. These models are not flexible to use with different depths of details as the control system needs to be updated or modified from a conventional approach. Detailed equivalent models have been introduced for regular MMCs [37] to overcome these issues and to efficiently simulate regular MMCs in full detail similar to the accuracy of a bona-fide EMT model.

The MMC-ES distributes energy storage within SMs of the converter. Thus converter-level averaged capacitor dynamics and phase-level averaged dynamic implementations are insufficient in fully studying the converter's operation. The energy balancing controllers [15] require arm-level details in order to accurately balance the state-of-charge (SOC) within the converter using circulating currents. Thus modeling with arm-level quantities or SM-level quantities is required in MMC-ES studies. Therefore, solutions such as averaged-value models (AVMs) and detailed equivalent models (DEMs) have been proposed for MMC-ES as well. The AVM proposed in [62] uses time-averaged quantities (e.g., average SM capacitor voltage and battery current) and represents the multivalve using a variable voltage source. The DEM proposed in [58] uses a Thevenin equivalent of the switching multivalve; it calculates the Thevenin source and resistance based on the individual firing pulses and the individual SM quantities of the multivalve. The DEM does not lose any information, as

is the case in the averaging process in an AVM. Both the AVM and DEM yield significant computational efficiency gains by reducing the number of switching and static nodes that the converter's model introduces to the admittance matrix of the entire network.

The DEM in [58] is capable of simulating steady state and dynamic behavior of the converters, as well as the high-frequency transients in the ac network caused by solid three-phase faults. The AVM in [62] is capable of simulating, in an averaged sense, the steady state and dynamic behavior of the converter, as well as high impedance ac faults. None of these models, however, is able to simulate dc faults and the converter's blocked state, during which negative arm currents flow through the anti-parallel diodes of the SMs' bypassed switches. Identification of the arm current's zero-crossings is crucial for accurate modeling of the bypassing diode, as inaccuracies in doing so yield erroneous voltage and current chatter in the simulation results. Conventional solution for the chatter problem is to interpolate the nodal voltage solution to identify current zero-crossings. However, in the case of an MMC-ES, interpolation by solving for all the nodal voltages defeats the core purpose of both the DEM and AVM (the diodes are not even directly modeled in an AVM). Thus a novel approach for modeling the diodes of the bypassed switches of SMs of the MMC-ES is required. In this chapter, a solution to overcome this issue is presented; the solution retains the core advantages of both the DEM and AVM, and augments them using a small number of conventional diode and switch models with interpolation capability [64] in the context of an EMT solver. These models are capable of accurately modeling the converter's blocked state, thus enabling their use in the study of dc faults.

The chapter continues in section 4.2 with an overview of the converter and its controls. The augmentations to AVM and DEM are developed in section 4.3. Extensive model validations are given in section 4.4.

## 4.2 Control Systems Associated with MMC-ES

### 4.2.1 Basic Control Systems

The basic control systems associated with the MMC-ES is reviewed in depth in section 2.2. Positive sequence and negative sequence line current control using decoupled synchronous frame, circulating current control, dc-dc current control and battery state-of-charge (SOC) controls are basic control systems associated with MMC-ES. Additional outer loop controls can be implemented to control the converter active power output to ac network or control dc bus voltage, control output reactive power and support ac network and control dc power transmitted from the MMC-ES.

### 4.2.2 Startup Sequence for MMC-ES DC Transmission System

An MMC-ES consists of a large number of SMs with large capacitance, which is presented to the external network, particularly during startup. Upon starting a de-energized converter, and without special provisions for energization, high inrush currents may be drawn that could result in ac network voltage collapse. The authors in [65] propose a startup sequence for regular MMCs in HVDC transmission and [66] proposes a startup sequence for an MMC-ES operating as an inverter.

The proposed startup sequence is shown in Figure 4.1. Initially the converter is disconnected from the ac network, and is blocked, and its batteries are disconnected using contactors; converter controllers are also disabled. Disabling controllers prior to converter energization is essential, as the measurements before closing the ac breaker and converter deblocking could result in controller saturation and large transients after de-blocking. The ac breakers are closed first with pre-insertion resistors. Once the SM capacitors are partially

charged and ac current is reduced, the pre-insertion resistor is bypassed.

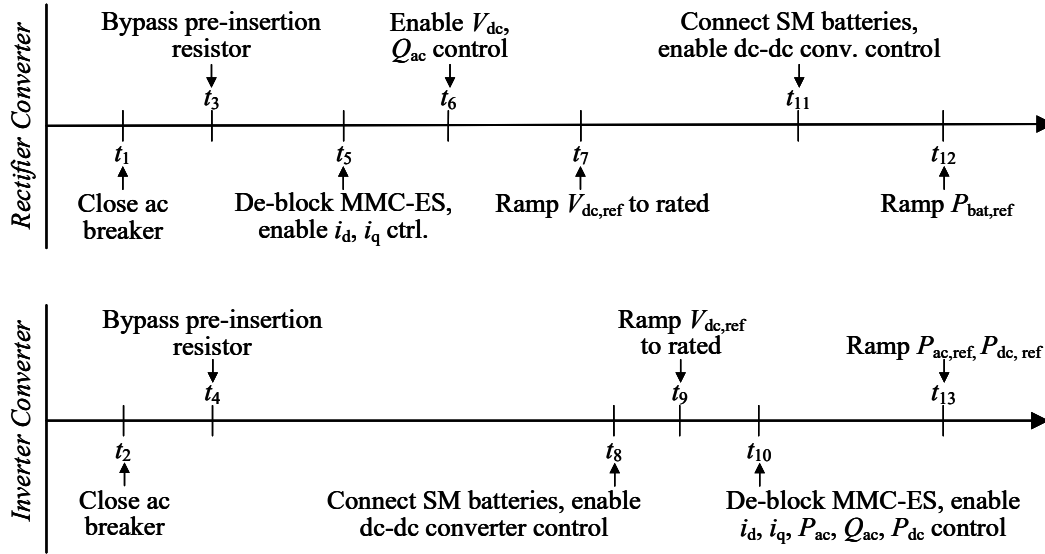


Figure 4.1: Startup sequence for MMC-ES HVDC link.

The rectifier is then de-blocked and decoupled current controllers, and DC voltage and reactive power controllers are activated in sequence as shown in Figure 4.1. The PI controllers are initialized and controllers are given reference set-point values that result in the smallest transients. Once the system stabilizes, the dc voltage reference is gradually ramped to the rated value. Then the inverter's batteries are connected and the dc-dc converter controllers are enabled keeping the SM voltage reference low to match the capacitor voltage already attained (e.g., 0.9 pu). Next the SM voltage reference is ramped up to the rated value. Then the inverter is de-blocked while enabling decoupled current controllers, ac power controllers, reactive power controllers, and dc power controller keeping the respective set point values at zero. Then the rectifier's batteries are connected with enabling dc-dc converter current controllers keeping the battery power reference at zero. Finally, and after all the transients settle, the power reference set points are ramped up.

### 4.2.3 Control Objectives of MMC-ES in an HVDC System

When MMC-ES are used in the context of an HVDC system, dc voltage control is normally assigned to the rectifier, while the inverter controls power flow. The dc voltage and the active power are directly related to one other and thus the current component responsible for active power may be used to control and maintain the dc link voltage by the rectifier. The embedded dc-dc converters in the inverter are controlled to maintain the SM average capacitor voltage, and dc power controllers in inverter(s) are activated to absorb desired amount of power from the dc network into the inverter. Any difference between the ac power ( $P_{ac}$ ) and dc power ( $P_{dc}$ ) set-points is taken in/out of the embedded batteries ( $P_{bat}$ ) while the dc-dc converter controller maintains SM average capacitor voltage.

As mentioned earlier, the rectifier maintains the dc link voltage. It provides power to the dc network to match the demand of the inverter and the losses in dc line. The dc-dc converters of the rectifier control battery currents to provide the desired amount of battery power to the system. Therefore the ac-side active power absorption or injection is determined by the difference between the dc power, battery power, and the losses of the MMC-ES. The rectifier, therefore, can also be used to support the ac network in providing services such as fast frequency response (FFR), or primary and secondary responses.

## 4.3 Development of Blocking-Enabled DEM and AVM Models

This section describes the development of the blocking-enabled DEM and AVM models, starting with a review of switch operations within a multivalve. An overview of the derivation of the DEM and AVM is given, followed by the proposed upgrades that enable simulation of

the blocked conditions.

### 4.3.1 Switching States of a MMC-ES Multivalve

Figure 4.2 shows current conduction paths during normal and blocked states in an MMC-ES multivalve with  $N$  SMs. During normal operation, inserted SMs are indexed  $i = 1 : p$  and bypassed SMs are indexed  $(p + 1) : N$ . When the converter is blocked, all  $N$  SMs are blocked. The dc-dc converter in each SM is assumed to be providing a constant current to the capacitor during these states and is not of concern.

It is observed that under normal conditions, when the arm current ( $i_j^k$  arm current of phase  $j = \{a,b,c\}$  and arm  $k = \{\text{up,low}\}$ ) is positive (charging SM capacitor),  $i_j^k$  passes through  $p$  diodes in  $Q_3$  and  $N - p$  IGBTs in  $Q_4$ . Similarly when  $i_j^k$  is negative,  $i_j^k$  passes through  $p$  IGBTs in  $Q_3$  and  $N - p$  diodes in  $Q_4$ . When the converter is blocked,  $i_j^k$  conducts through  $N$  diodes in  $Q_3$  and  $Q_4$  when the arm current direction is positive and negative, respectively. Power semiconductor switches show a low resistance ( $\approx$  short circuit) when on ( $R_{\text{on}}$ ) and a high resistance ( $\approx$  open circuit) when off ( $R_{\text{off}}$ ). Assuming that both IGBTs and diodes display similar resistance values for these two states, it is concluded that arm current effectively conducts through a resistance of  $NR_{\text{on}}$  irrespective of the operating condition.

Switching events are frequent during normal operation as the control system continuously inserts and bypasses SMs. Additionally, MMC-ES consists of a large number of active and passive elements, which contribute to the massive size of the admittance matrix. Due to these reasons, conventional EMT-grade detailed switching model implementations are inadequate and impractical. Computationally efficient models are required to study the operating behaviour of MMC-ES.

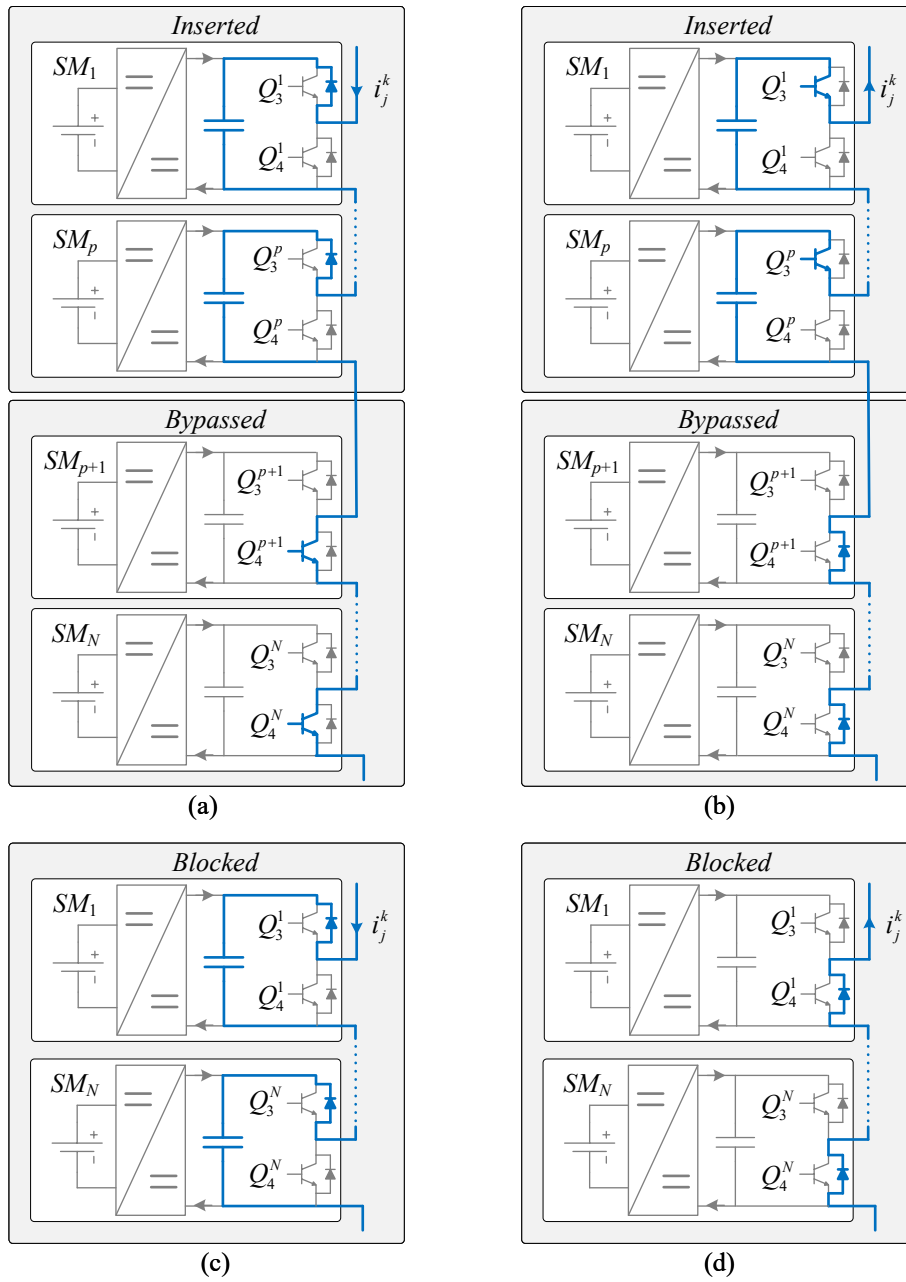


**Figure 4.2:** Arm current conduction paths in MMC-ES (a) normal operation, positive current (b) normal operation, negative current (c) blocked with positive current (d) blocked with negative current.

### 4.3.2 Developing Computationally Efficient EMT Models

#### Detailed Equivalent Model (DEM)

A schematic diagram of an MMC-ES SM is shown in Figure 4.3(a). Passive elements ( $L_{SM}$  and  $C_{SM}$ ) are discretized using Dommel's method and represented as Thevenin equivalents, and switches are replaced with switching-state-dependent resistances as shown in Figure 4.3(b). In this figure,  $R_{Q,x}$ ,  $R_C$ ,  $R_L$ ,  $V_{C,h}$ ,  $V_{C,L}$  and  $v_{bat}$  represent the instantaneous resistance of switch  $x$  ( $x = 1 : 4$ ), EMT equivalent capacitor resistance, EMT equivalent inductor resistance, EMT history voltage source of capacitor, EMT history voltage source of inductor, and battery voltage [36], respectively. Battery voltage is estimated based on the Shepherd's model [67] as done in [58]. The circuit in Figure 4.3(b) can now be simplified to a single Thevenin equivalent with a source voltage of  $V_{SM, thev, i}$  and resistance of  $R_{SM, thev, i}$  as in Figure 4.3(c). It should be noted that the switch resistances depend on the firing pulses ( $FP$ ) issued to the corresponding switch. The entire multivalve at this point is a collection of series connected SM Thevenin equivalents (Figure 4.3(d)), and can be further simplified to a single Thevenin equivalent as shown in Figure 4.3(e) with parameters as given in (4.1) and (4.2). Details of the implementation and validation of this model can be found in [58].

$$V_{MV, thev} = \sum_{i=1}^N V_{SM, thev, i} \quad (4.1)$$

$$R_{MV, thev} = \sum_{i=1}^N R_{SM, thev, i} \quad (4.2)$$



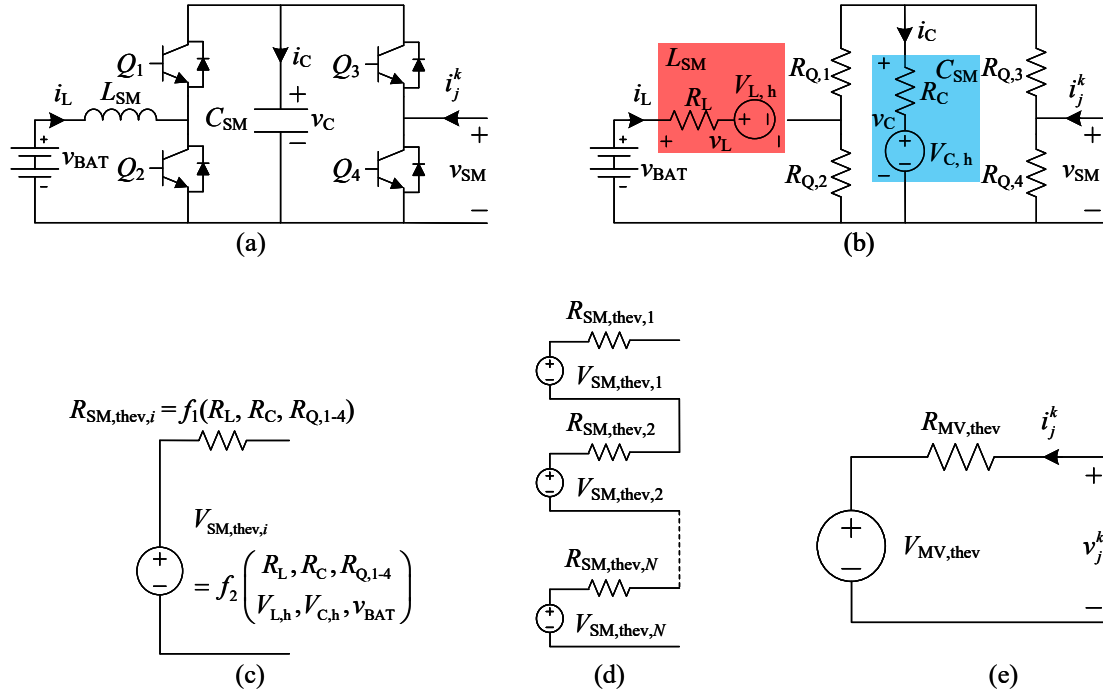


**Figure 4.3:** Development of DEM (a) SM schematic (b) EMT equivalent (c) Thevenin equivalentnet of a SM (d) multivalve representation (e) Thevenin equivalentnet of a multi-valve.

### Averaged-Value Model (AVM)

The AVM of the MMC-ES has been developed in section 3.1 and validated for steady state operation with extensive simulation and experimental setup comparison. Figure 4.4 provides an overview of the AVM.

#### 4.3.3 Inclusion of the Blocked State in DEM and AVM

Figures 4.2(c-d) show that the arm current does not participate in SM capacitor voltage dynamics when  $i_j^k < 0$  and only participates when  $i_j^k > 0$ . Thus when a multivalve is blocked, a suitable path must be created around the DEM and AVM to account for this

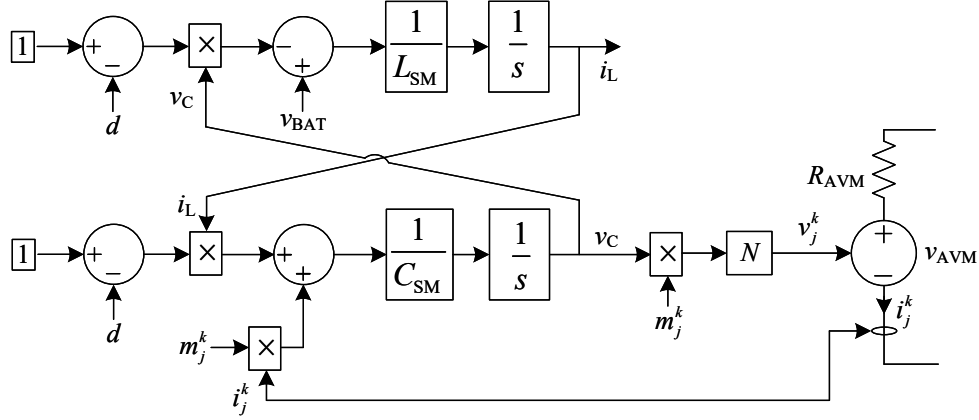


**Figure 4.4:** Overview of AVM.

change in the path of the arm current. It must be noted that a positive arm current passes through all the SM capacitors in the multivalve.

### Upgrade to DEM

The DEM can be upgraded as shown in Figure 4.5. The original DEM, in the form of a Thevenin equivalent shown in the grey box in Figure 4.5, is augmented with additional circuitry to account for the path of the arm current during the blocked state. The newly added IGBT ( $T$ ) receives a high gate-signal ( $FP_{IGBT}$ ) during normal operation. The on-state resistances of  $T$  and  $D_1$  are selected to be very small to minimize their impact relative to  $R_{MV, thev}$ . The diode  $D_2$  is reverse biased and off during normal operation, and  $i_{arm} = i_j^k$  for both polarities of the current. When the converter is blocked, the gate signal to  $T$  is set to low, turning it off. During this condition, positive arm current flows via  $D_1$  and  $i_{arm} = i_j^k$ . Negative arm current, however, flows through  $D_2$  and  $i_{arm} = 0$ . From Figure 4.2 it is observed that  $N$  diodes conduct the arm current in blocked condition for both current directions. Therefore, the on-state resistance of  $D_2$  is set to  $NR_{on}$ .

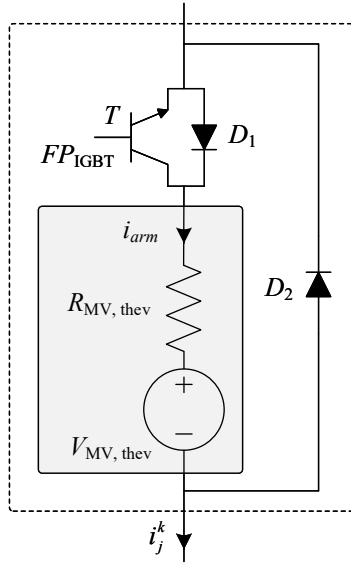


**Figure 4.5:** Upgraded DEM model to simulate blocking.

When the converter is blocked, the control system could set the firing pulses to low for both  $Q_3$  and  $Q_4$  switches. However, this conflicts the SM capacitor insertion. Hence a modification is made to the control system to set  $Q_3$  high and  $Q_4$  low in all SMs when the converter is blocked.

### Upgrade to AVM

Different modulation techniques, e.g., NLC or PWM methods, can be used to determine the number of SMs inserted at a given moment [38]. During a fault, the modulation waveform could exceed the converter's operating limits. For example, in a control system designed to generate modulation waveforms between -1 and +1 (where -1 represents no SMs inserted and +1 represents  $N$  SMs inserted), modulation waveform values above +1 and below -1 result in SM counts more than  $N$  and less than 0 to be inserted. This is theoretically impossible. Thus a modification as shown in Figure 4.6 is proposed. In this figure  $m_{\text{ref},j}(t)$ ,  $m_j^{\text{circ}}(t)$ ,  $n_j^{\text{up}}(t)$ ,

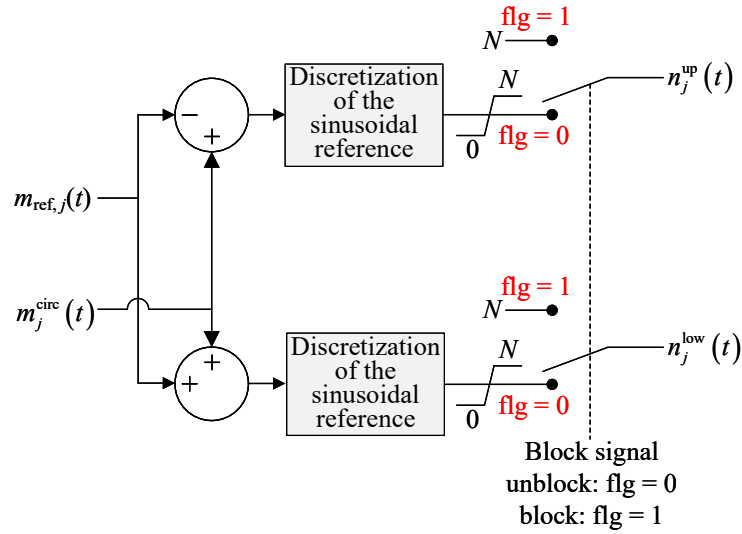


**Figure 4.6:** Upgrade to the AVM modulation scheme to simulate blocked state

and  $n_j^{\text{low}}(t)$  denote the modulation waveform created by line current controllers, accumulated modulation waveforms from circulating current controllers, and instantaneous number of SMs to be inserted to upper and lower arms respectively. The output of the discretization module is hard-limited between 0 and  $N$ . A selector switch controlled by the blocking signal is also placed at the output to ensure that during blocking all  $N$  SMs are inserted. Additionally, the same augmenting circuitry (see Figure 4.7) used for a DEM to block negative arm currents entering the capacitor is required. The modified AVM continues to be built around the same model (shown within the grey box in Figure 4.7) derived in section 3.1. With this implementation  $i_j^k$  in Figure 4.4 is replaced with  $i_{arm}$ .

#### 4.3.4 Numerical Chatter Elimination in Upgraded Models

During the operation of the converter, the arm current changes direction and switches are turned on and off continuously. As a result, the current conduction path continuously al-

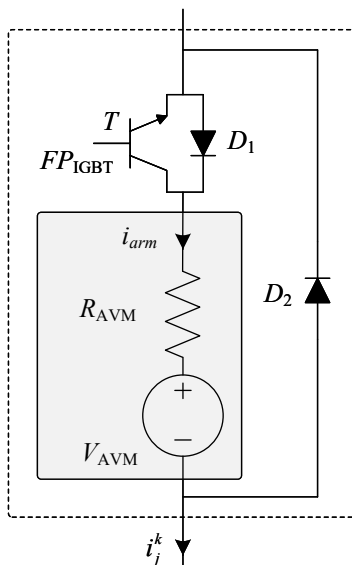


**Figure 4.7:** Upgraded AVM model to simulate blocking.

ternates between the IGBT or its anti-parallel diode. EMT simulations are conducted using discrete time steps ( $\Delta t$ ), usually in the order of a few microseconds. Neither the DEM nor the AVM explicitly models the anti-parallel diode and IGBT. The DEM models a switch with a firing-pulse-dependent resistance. The AVM creates the voltage waveform based on the modulation waveform. This does not have an adverse effect during normal operation and at relatively small time steps (e.g., 20  $\mu\text{s}$ ) as the firing pulses and modulation waveforms are issued with high accuracy. However, when the converter is blocked, this causes adverse effects, as discussed in the following example.

Figure 4.8 shows a blocked multivalve. In this figure  $V_{MV}$  and  $R_{MV}$  represent the equivalent voltage source and resistance introduced either by DEM or AVM. Current conduction paths are in bold. At the simulation time  $t = t_0$  the arm current conducts via  $D_1$  ( $i_j^k(t = t_0) = I_1 > 0$ ). At this instant, the EMT solver solves for node voltages of the network and evaluates  $i_j^k(t = t_0 + \Delta t) = -I_2$  where  $I_2 > 0$ . This current can only flow through

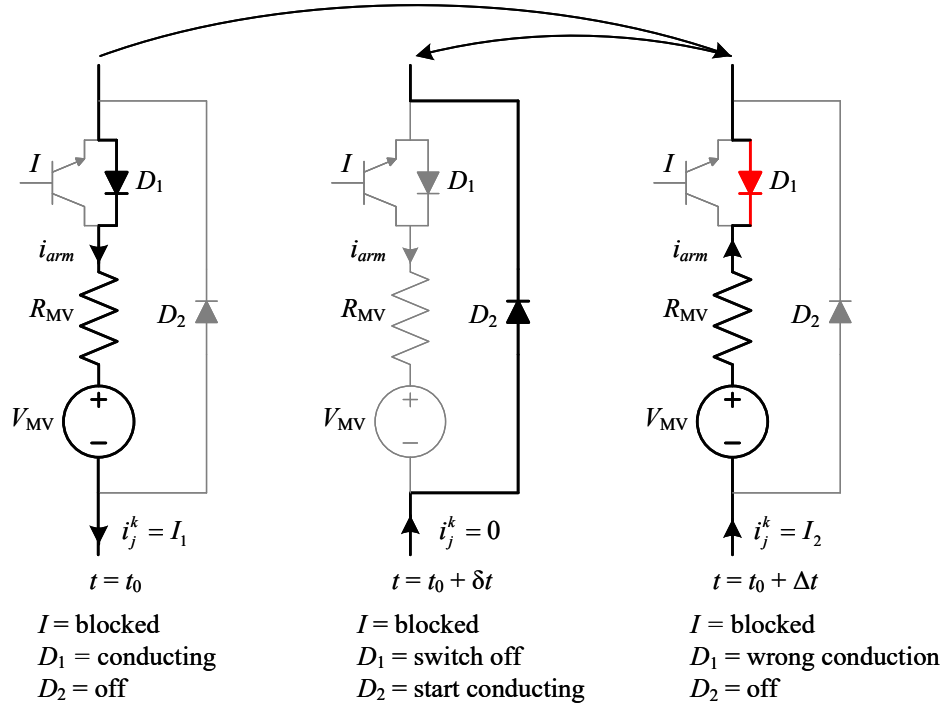


**Figure 4.8:** Mechanisms of interpolation to avoid numerical chatter.

$D_2$ ; this sudden change in the current direction within a time step results in a large voltage across the arm inductor ( $v_{L_A}$ ) as shown by (4.3).

$$v_{L_A} = L_A \frac{di_j^k}{dt} \tag{4.3}$$

By using interpolation-enabled IGBTs and diodes to build the circuitry around the DEM and AVM shown in Figures 4.5 and 4.7, the EMT solver is forced to re-evaluate the network solution at the instant of current's zero-crossing ( $t = t_0 + \delta t$ , where  $\delta t < \Delta t$ ) using linear interpolation [68]. This process ensures that  $D_1$  is turned off and  $D_2$  is turned on at the instant of zero-crossing of the current, thus eliminating the voltage chatter.

## 4.4 Simulation Validation

This section presents several studies using models with and without provisions for blocking to demonstrate the accuracy of the models proposed in this chapter. Existing work on DEM and AVM for MMC-ES [58,62] includes both simulation-based and experimental verification of these models in their original form for conditions when the converter is not blocked. The results in this section demonstrate the accuracy of the models presented in this chapter for the conditions when the converter is blocked, as well as for other conditions when blocking does not occur. Although an experimental MMC-ES is available to the authors [22, 58, 62], experimental results for faulted conditions are not obtained due to safety, liability, and warranty restrictions.

### 4.4.1 Description of the Test System

The test system used to validate models developed in this chapter is shown in Figure 4.9, and its parameters are given in Table 4.1. Frequency-dependent transmission line models are used to represent the dc lines. Faults are applied at the middle of the dc line and at the ac-side PCC as marked on Figure 4.9. The direction of the dc current measurements, positive and negative poles, and the inverter and rectifier are clearly marked on Figure 4.9. For modeling convenience, positive DC current is assumed to be flowing into the converter; this has no other implication on the applicability of the model. Simulations are conducted in the PSCAD/EMTDC transient simulator, and include the following five models: (i) detailed switching model (DSM), (ii) original detailed equivalent model in [58] without blocking provisions (DEM wo/blk), (iii) detailed equivalent model with the proposed provisions for blocking (DEM w/blk), (iv) original averaged-value model in [62] without blocking provisions

(AVM wo/blk), and (v) averaged-value model with the proposed provisions for blocking (AVM w/blk). The simulation results show phase-a quantities for the ac voltage and current, and phase-a upper arm's averaged quantities for the average capacitor voltage and average battery current in Sections 4.4.2 to 4.4.5. All simulations are carried out with a  $5 \mu\text{s}$  time-step, unless otherwise noted. Simulation results from the DSM are used as the benchmark for validations of those of the other four models.

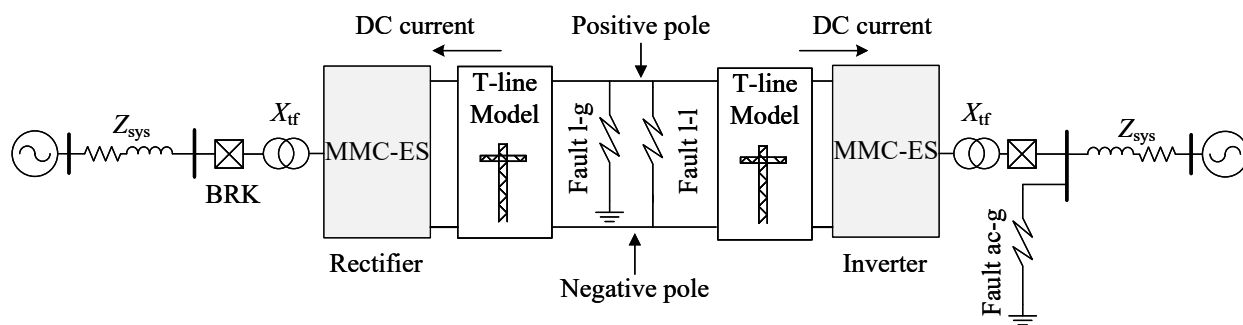


**Figure 4.9:** Schematic diagram of the test system.

#### 4.4.2 Power Set Point Change

After reaching steady state, the power set-points for battery power ( $P_{\text{bat, ref}}$ ) of the rectifier, and ac power ( $P_{\text{ac, ref}}$ ), and dc power ( $P_{\text{dc, ref}}$ ) of the inverter are changed as shown in Table 4.2. Simulation results are shown in Figure 4.10 with magnification around the transients. Results from all models agree well with each other and with the benchmark DSM traces. The average capacitor voltage and average battery current in Figure 4.10(j) and (k) shows some minor discrepancy. The DSM and DEM models agree well with each other, but the AVM models slightly deviate from the detailed models. Detailed models show the inductor current ripple due to switching, which is not simulated in AVM. The ripple causes additional



**Table 4.1:** Simulated System Data

<b>MMC-ES Parameters</b>			
SM capacitance ( $C_{SM}$ )	20 mF	SM inductance ( $L_{SM}$ )	5 mH
Arm inductance ( $L_A$ )	2 mH	Number of SMs per arm	10
DC link voltage ( $V_{dc}$ )	10 kV	AC voltage ( $V_{rms,conv}$ )	5.6 kV
Transformer reactance ( $X_{tf}$ )	0.168 pu	Power rating ( $S_{MMC-ES}$ )	3.5 MVA
Battery voltage ( $v_{bat}$ )	0.5 kV		
<b>Network Parameters</b>			
AC voltage ( $V_{grid,rms}$ )	10 kV	Network impedance ( $Z_{sys}$ )	$2.1 + 8.0j \Omega$
<b>DC Line Parameters</b>			
Line length ( $l$ )	100 km	Height of conductors ( $h$ )	30 m
Conductor spacing ( $d$ )	10 m		
<b>EMT Environment Parameters</b>			
Switch on resistance ( $R_{on}$ )	0.01 $\Omega$	Switch off resistance ( $R_{off}$ )	100 k $\Omega$
Simulation time step ( $\Delta t$ )	5 $\mu s$		

power losses in the dc-dc converter, which are reflected as a dc offset in the rectifier's average capacitor voltage and a lower average battery current in the inverter. Figure 4.11 shows that all the models accurately predict power distribution within each converter.

### 4.4.3 AC Three-phase Fault

A symmetrical three-phase-to-ground fault is applied at the PCC at  $t = 5.0$  s. The converters are blocked 2 ms after the inception of the fault, and the trip signal to open ac-side breakers is issued 18 ms afterwards. The fault is cleared after 50 ms. The power set-points of the

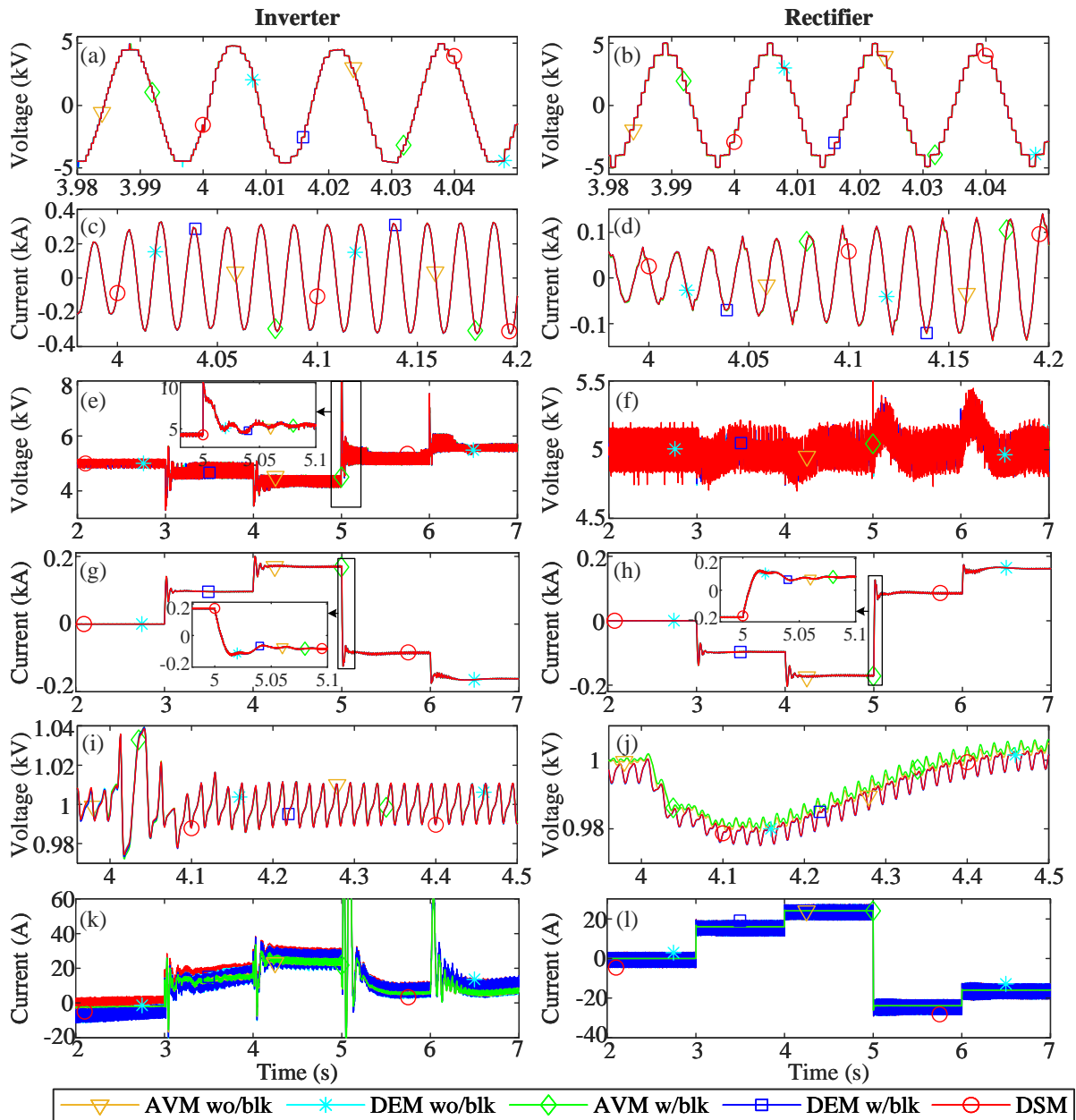


**Figure 4.10:** Responses to power set-point changes at inverter and rectifier end (a,b) ac voltage, (c,d) ac current, (e,f) positive pole dc voltage, (g,h) positive pole dc current, (i,j) average SM capacitor voltage, (k,l) average battery current.

**Table 4.2:** Power set point change with time

Time (s)	$P_{\text{bat, ref}}$ (pu)	$P_{\text{ac, ref}}$ (pu)	$P_{\text{dc, ref}}$ (pu)
0.0	0	0	0
3.0	0.2	0.5	0.3
4.0	0.3	0.8	0.5
5.0	-0.3	-0.2	-0.3
6.0	-0.2	-0.5	-0.6

inverter are kept as  $P_{\text{ac, ref}} = 0.8$  pu and  $P_{\text{dc, ref}} = 0.5$  pu and at the rectifier  $P_{\text{bat, ref}} = 0.3$  pu. At this operating point, the inverter injects 0.8 pu of active power to the ac grid while absorbing 0.5 pu power from the dc side. Batteries at the inverter give around 0.3 pu power while also making up for the converter losses. The rectifier discharges 0.3 pu of battery power and provides dc power output around 0.5 pu, thus absorbing around 0.2 pu from its ac system while making up for the losses. Simulation results are compared in Figure 4.12. All the models represent the response of the system accurately but only up to the blocking instant, after which the models without blocking provisions show clear deviation, while the models proposed in this chapter continue to correctly predict the system's response.

#### 4.4.4 DC Line-to-Ground Fault

A solid line-to-ground fault is applied at  $t = 5.0$  s at the mid-point of the dc line, and lasts 50 ms. The inverter and rectifier are blocked after 2 ms and the trip signal to open ac breakers is issued after 20 ms. Simulation results are shown in Figure 4.13.

It is readily observed that the proposed blocking-enabled models accurately capture the converter's behaviour during the fault and after it is blocked. Existing DEM and AVM (i.e.,

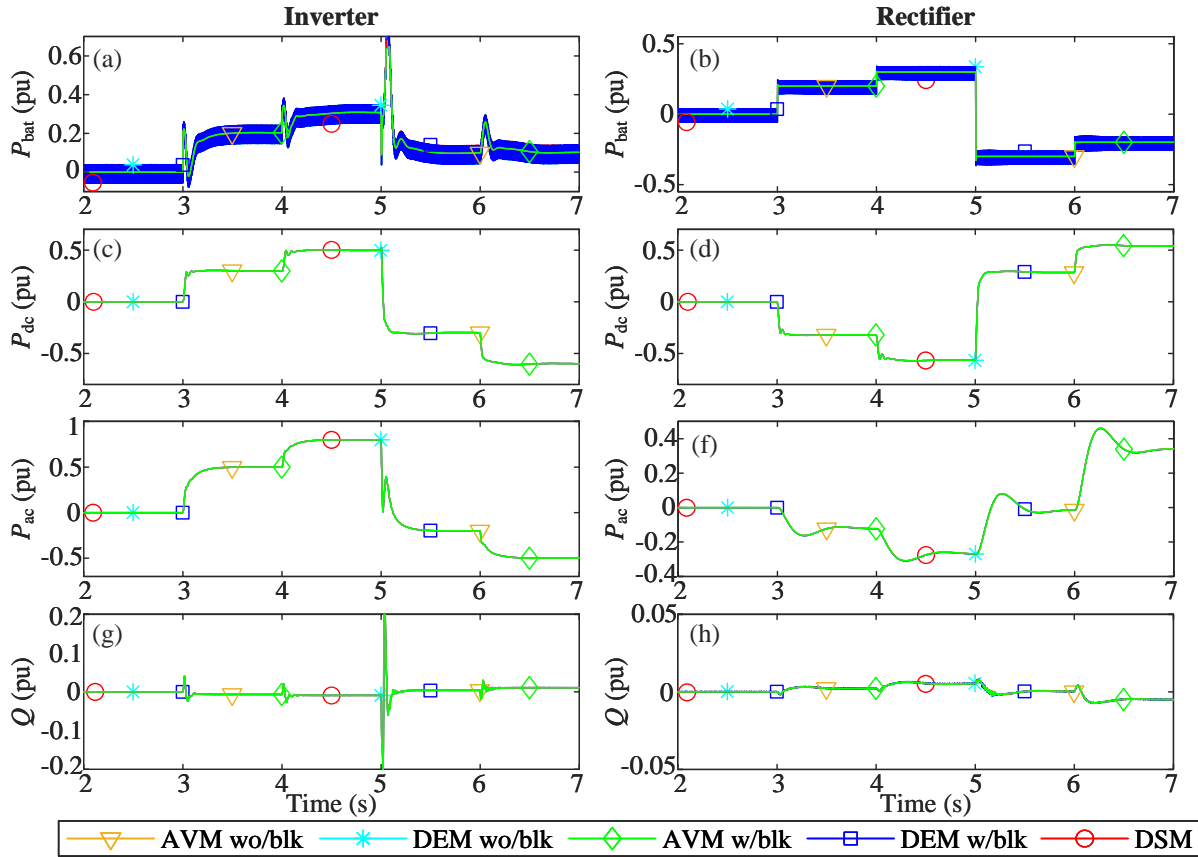


**Figure 4.11:** Power distribution within the two converters.(a,b) battery power, (c,d) dc link power, (e,f) ac active power, (g,h) reactive power.

DEM wo/blk and AVM wo/blk) capture the initial response to the dc fault but fully diverge after the converters are blocked.

#### 4.4.5 DC Line-to-Line Fault

A solid line-to-line fault is applied at  $t = 5.0$  s at the mid-point of the dc line, and lasts 50 ms. The inverter and rectifier are blocked after 2 ms and the trip signal to open ac breakers is issued after 20 ms. Simulation results are shown in Figure 4.14. As expected the half-bridge MMC topology cannot arrest a dc fault current.

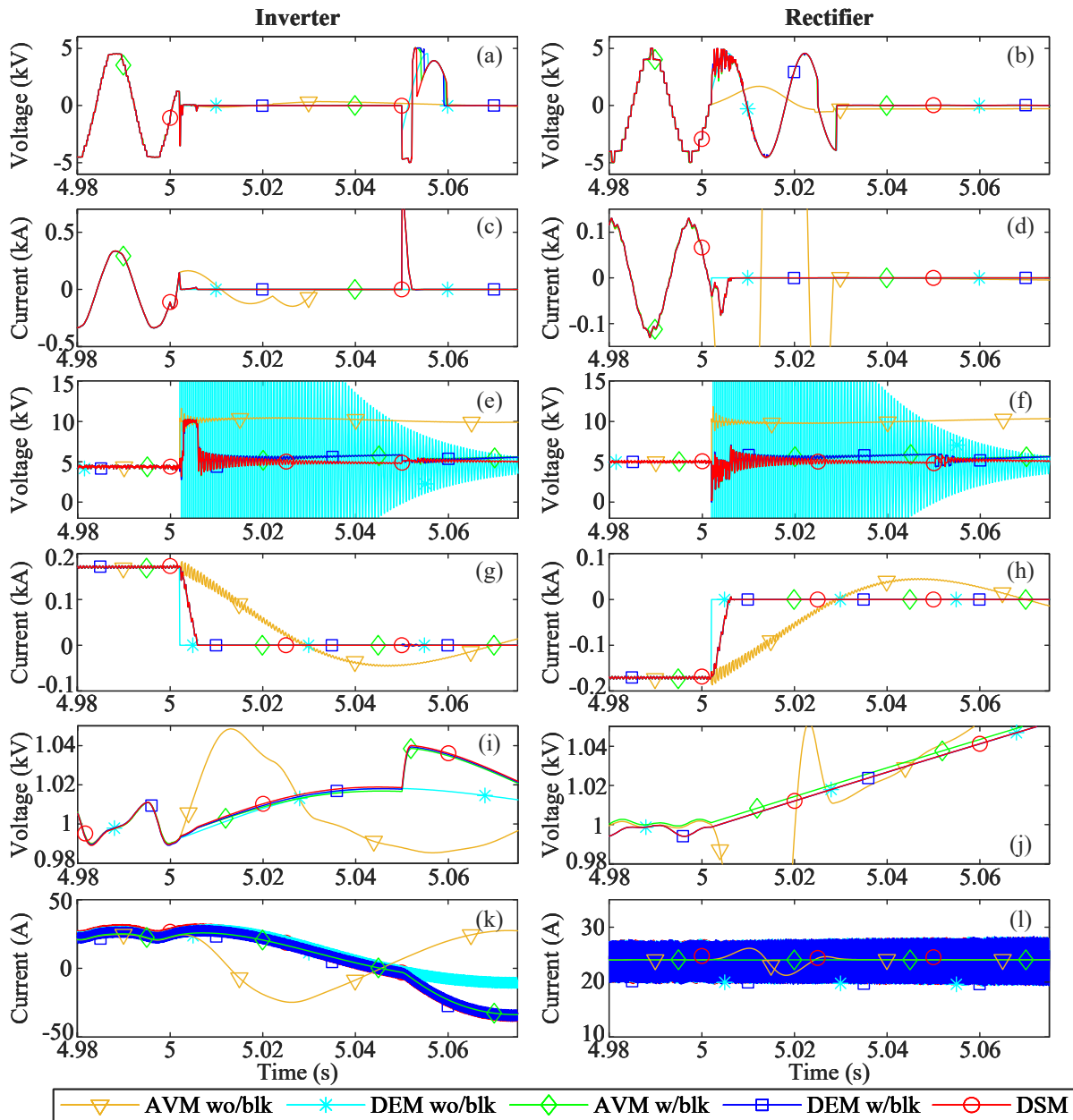


**Figure 4.12:** AC three phase fault at inverter’s PCC.(a,b) ac voltage, (c,d) ac current, (e,f) positive pole dc voltage, (g,h) positive pole dc current, (i,j) average SM capacitor voltage, (k,l) average battery current.

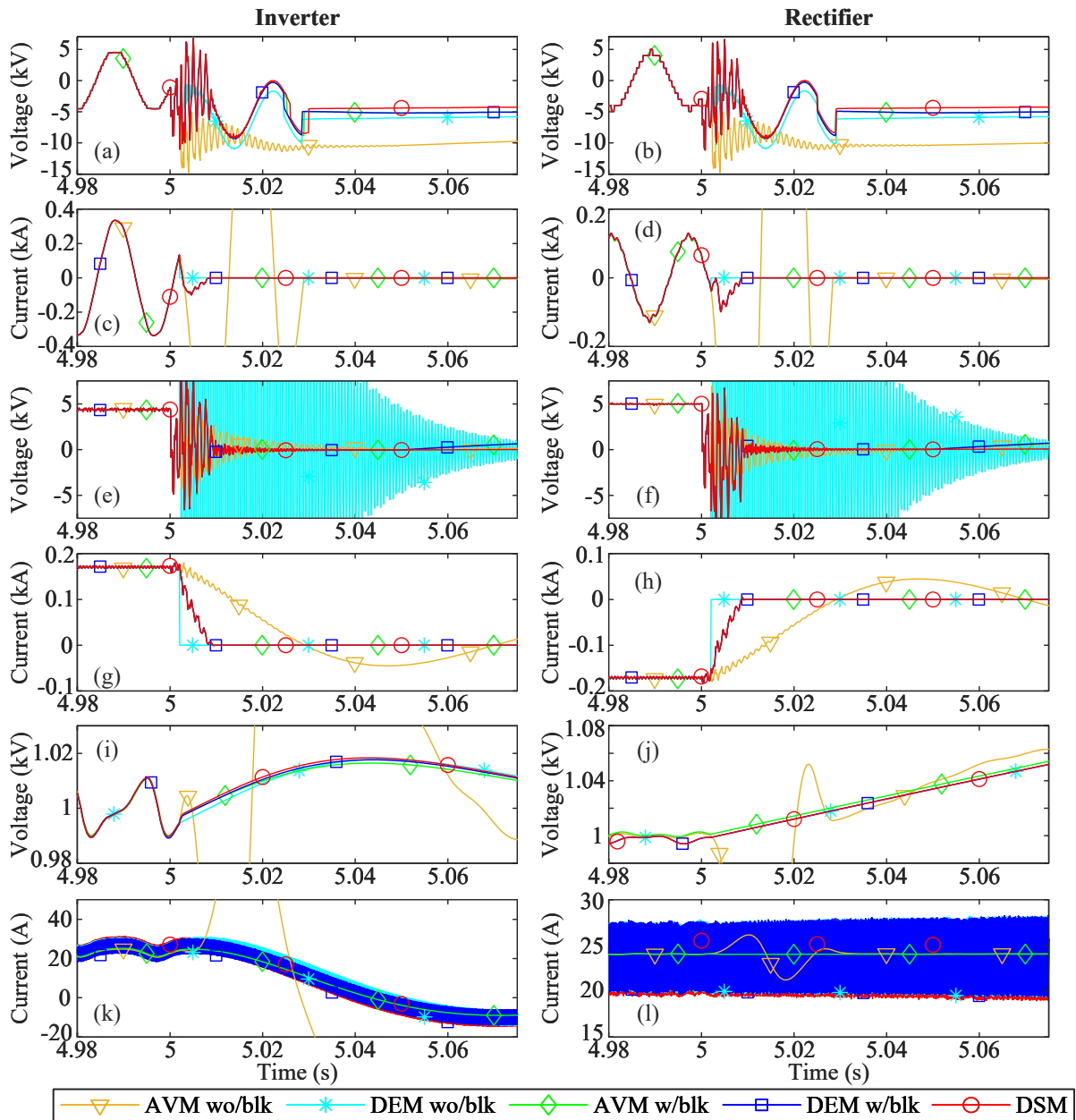


**Figure 4.13:** Response to a dc line-to-ground fault.(a,b) ac voltage, (c,d) ac current, (e,f) positive pole dc voltage, (g,h) positive pole dc current, (i,j) average SM capacitor voltage, (k,l) average battery current.

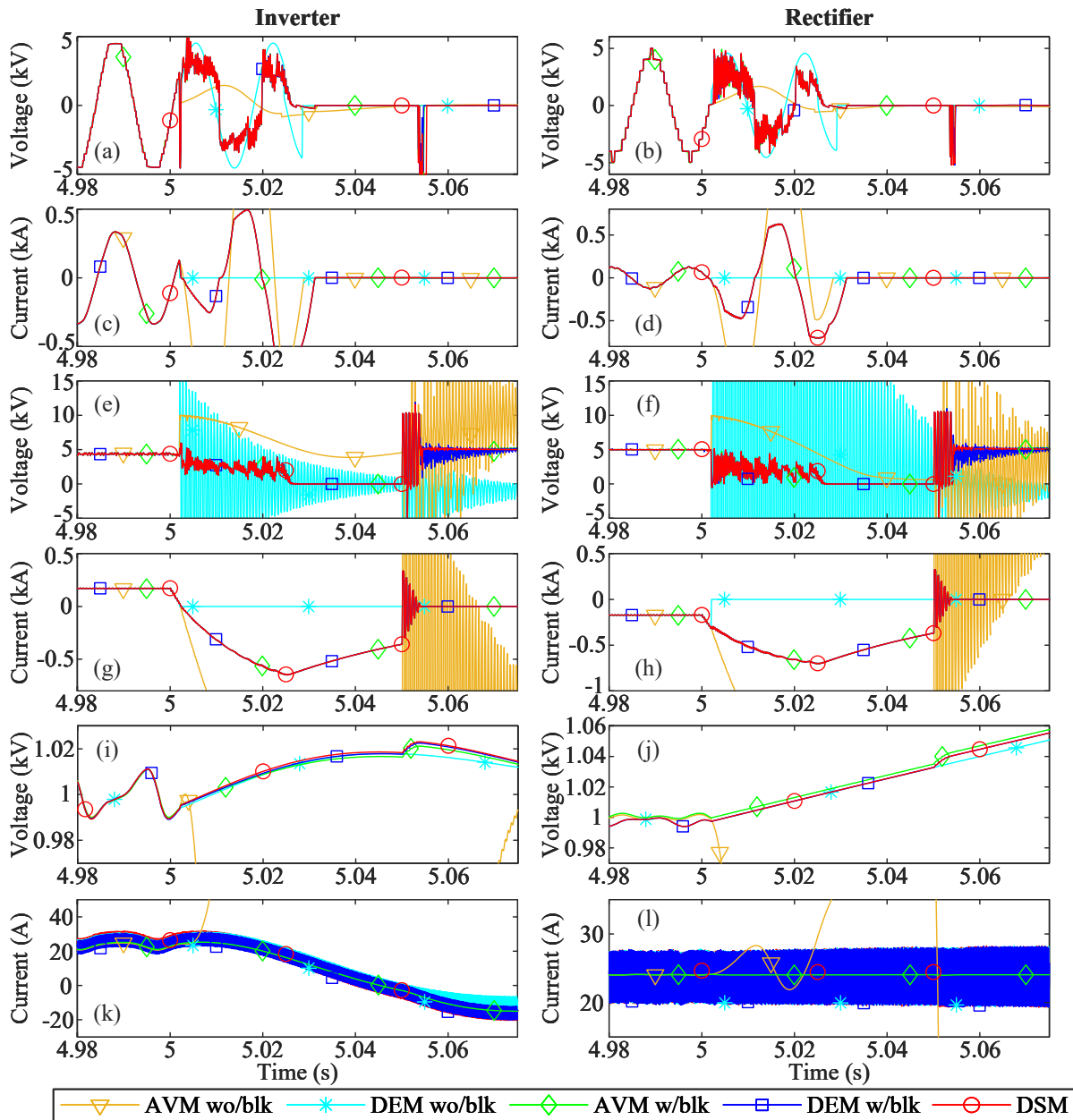


**Figure 4.14:** Response to a dc line-to-line fault.(a,b) ac voltage, (c,d) ac current, (e,f) positive pole dc voltage, (g,h) positive pole dc current, (i,j) average SM capacitor voltage, (k,l) average battery current.

The initial duration of converters' operation after the fault and before blocking is captured correctly by all models. The models without blocking provisions (AVM wo/blk and DEM wo/blk) fail to accurately capture the response after the converter is blocked, while the blocking-enabled models proposed in this chapter correctly capture the entire behavior.

#### 4.4.6 Startup Sequence

The startup sequence of the converter is tested with a pre-insertion resistor value of  $100\ \Omega$  and for the operation times shown in Table 4.3 (see Figure 4.1 for the sequences). The ac current, capacitor voltage, and battery current are observed for only the DSM, DEM w/blk and AVM w/blk models as the previous validations clearly proved that DEM wo/blk and AVM wo/blk fail in simulating converter blocking scenarios. It is observed from Figure 4.15 that both DEM w/blk and AVM w/blk are able to fully and accurately capture the startup transients. Additionally, the proposed startup sequence slowly charges the SM capacitors, so lower inrush currents appear in the system, which help to avoid voltage collapse and controller saturation. A slight difference is observed in the AVM inverter average battery current, which is due to the high frequency ripple not present in this model.

#### 4.4.7 Impact of Simulation Time-Step

Both the DSM and DEM represent the switchings within the MMC-ES and thus require a small simulation time-step. A heuristic rule is to select a time-step that is at least 10 times smaller than the smallest period of the transients expected to be observed in the system. AVM models, however, simulate the averaged behaviour of the converter and include relatively low frequency components. Thus considerably larger time-steps could be used in simulations with AVMs. Figure 4.16 shows the performance of the proposed AVM w/blk



**Table 4.3:** Startup sequence timing parameters

Rectifier		Inverter	
Symbol	Time (s)	Symbol	Time (s)
$t_1$	0.05	$t_2$	0.05
$t_3$	2.5	$t_4$	2.5
$t_5$	3.0	$t_8$	5.0
$t_6$	3.2	$t_9$	5.1
$t_7$	3.6	$t_{10}$	5.6
$t_{11}$	6.0	$t_{13}$	7.0
$t_{12}$	7.0		

against the DSM and DEM w/blk during a dc line-to-line fault. It is observed that at larger time-steps DSM and DEM show deviations, while the AVM maintains high accuracy (in an averaged sense) even at larger simulation time-steps. The deviations in the DSM and DEM models at large time-steps is due to the overly coarse granularity of the data points that leads to a large number of switching instants to be left out.

#### 4.4.8 Computational Efficiency

Both AVMs and DEMs reduce drastically the number of nodes and branches in the system model compared to the DSM. This reduces the number of nodal matrix switchings and matrix inversions, and results in high computational efficiency. DEMs do not lose any information about the multivalve, and as such require large amounts of data storage in their evaluation process to store the individual states of all the SMs in the converter. AVMs, on the other hand, only store data for the representative (averaged) capacitor and inductor per

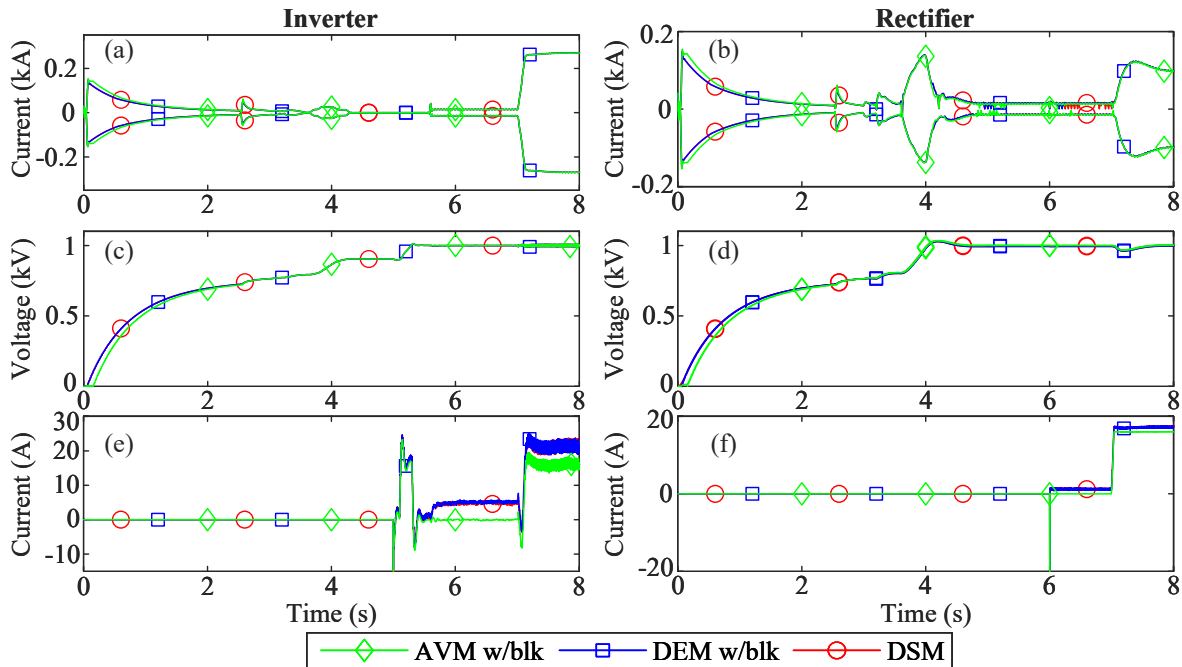


**Figure 4.15:** MMC-ES during startup (a,b) envelope of the ac line current, (c,d) average capacitor voltage, (e,f) average battery current.

multivalve. As a result, considerable computing-time advantages can be achieved by using AVMs to simulate converters with a large number of SMs.

To gain the ability to represent converter blocking, as developed in this chapter, one additional IGBT and two diodes are added to both the DEM and AVM of each multivalve. This slightly increases the number of nodes in the system's admittance matrix compared with the original DEM and AVM; it also adds very slightly to the computational burden of these models, but it is significantly outweighed by the ability to correctly represent the converter's full operating modes, including when it is blocked. Table 4.4 shows a comparison of models with simulation time-step and matrix switching count. Each simulation is carried out in three subsystems (SS1 to SS3), which are separated by transmission line segments. SS1 and SS2 consist of MMC-ES with ac networks, and SS3 consists of the mid-point of

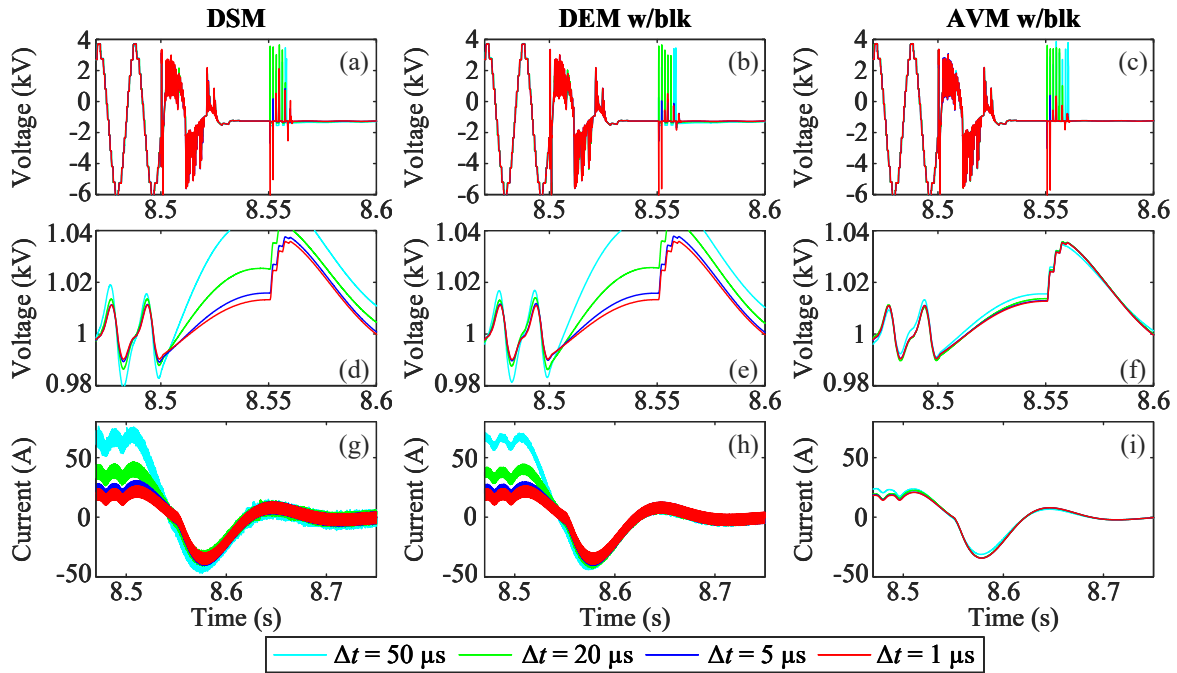


**Figure 4.16:** Effect of simulation time-step (a-c) ac voltage, (d-f) average capacitor voltage, (g-i) average battery current.

dc transmission line expanded to simulate dc faults. From Table 4.4 it is observed that all DEM and AVM models offer greatly reduced computational times compared to the DSM. As expected the two proposed simulation models only have slightly more computational time compared with their counterparts without blocking provisions.

## 4.5 Summary

This chapter proposed a major improvement to detailed equivalent and averaged-value models for an MMC with embedded storage that enables simulation of converter blocking. Each converter multivalve was augmented with additional interpolation-enabled IGBT and diodes to accurately capture current zero-crossings without compromising the core benefits of sim-

**Table 4.4:** Simulation time for different models (run time: 1 s)

Model	Time step ( $\mu\text{s}$ )	Comp. time (s)	No. of matrix switchings (SS1, SS2, SS3)
DSM	10	507.750	433670, 176312, 1
	2	585.625	266655, 77177, 1
DEM wo/blk	10	5.953	20375, 21298, 1
	2	26.453	22143, 22146, 1
AVM wo/blk	10	2.984	1, 1, 1
	2	16.203	1, 1, 1
DEM w/blk	10	7.265	21810, 23091, 1
	2	30.500	24060, 24199, 1
AVM w/blk	10	3.797	1907, 1909, 1
	2	16.187	1990, 1728, 1

plicity and computational efficiency of the detailed equivalent and averaged-value models. The performance of the new models was compared, in depth, against a detailed switching model developed in the PSCAD/EMTDC simulator in a number of cases within a dc transmission system. Simulation results fully confirmed the anticipated accuracy of the proposed models in capturing the blocked state of the converter, which is critical in simulating the converter's behavior in response to a dc fault. The results also confirmed that the new models do not undermine the computational advantages of the underlying models, thus retaining their applicability in the study of large, converter-intensive systems. The findings of this chapter are published in [69] (IEEE Early access).

## Chapter 5

# Frequency Support and other Ancillary Services Using MMC-ES

### 5.1 Case Study 1: Increasing Dispatchability of a PV Power Plant through MMC-ES

#### 5.1.1 Introduction

The power output of a solar PV plant is dependent on solar irradiance and the temperature of the PV panels. Throughout the day, the received solar irradiance is subject to change due to cloud movement, accumulation of dust, etc. [70]. Sudden irradiance variations could result in large changes in the output power of a PV power plant where a large number of PV panels are used. This could lead to undesired outcomes on the power system with respect to frequency, voltage and power quality. Therefore it is vital to make necessary arrangements to reduce these power fluctuations as much as possible.

Many researchers around the world are working on the power intermittency and dispatchability issues related to PV power plants. Irradiance prediction based on highly complex computer-based environmental models has become popular, but has proven to be expensive and of low accuracy [70, 71]. De-rating the PV power output [72, 73] has also become a popular research topic where the power output from the PV plant is curtailed at a given operating point that is lower than the maximum available power to leave some energy reservoir to support frequency variations as well as to enable dispatchability of the PV power plant. This control procedure provides a low-cost solution with regards to hardware requirements, but is clearly undesirable due to its low utilization factor. As an alternative approach to the above methods, energy storage can be installed with PV plants for improving dispatchability and countering intermittency [47, 74, 75].

In current installations, commercial BESS have been implemented mainly based on two- or three-level converters with large battery banks formed with several parallel connected battery strings (e.g., Hitachi's DynaPeaQ<sup>®</sup> system). These systems have known issues with uniformly charging and discharging batteries. The low number of converter levels at the ac interconnection requires filtering to reduce harmonic distortions introduced to the connected network. Fairly low voltages are required in the converter due to limitations of power electronic switches. To address these problems, an MMC-ES is considered. This converter disperses the battery units among converter submodules and generates an output voltage with good harmonic qualities. Additionally, the converter provides a medium voltage dc (MVDC) link, which can be further used for MVDC transmission. Individual battery currents can be controlled for uniform charging and discharging. Therefore, this converter has attracted the attention of many researchers as a means of introducing battery energy storage to the grid.

In this section, a study has been conducted to assess the applicability of using an MMC-ES with a PV power plant to smooth out the power transmitted from the PV power plant. The power order for the ac power output of the MMC-ES is determined by a moving average calculation of the PV power plant's output along with a droop function.

### 5.1.2 PV Plant Power Smoothing with Moving Average Window

As indicated in the introduction, solar insolation on a land area varies throughout the day due to cloud movement and, as a result, the power output of the PV plant fluctuates. In large PV installations, these variations could translate into high power variations injected to the power system, resulting in large frequency deviations unless compensated.

As a solution, this thesis proposes a moving averaging (MA) window-based control system to smooth out the power fluctuations caused by variations in solar insolation. The MA window samples PV plant's power output at a certain sampling rate (e.g., 2 Hz) and stores the sample values. The output of this block is the average of the samples and is held constant until a new sample is available. Upon arrival of a new sample, the oldest sample is discarded and the remaining samples shift in the averaging window queue. The power data samples from the PV plant are sent to the MMC-ES through a communication channel.

The power order from the moving average power smoother ( $P_{ac,ref1}$ ) is augmented with a droop controller. The droop controller measures the frequency of the system obtained from the phase locked loop (PLL) and generates a reference power order ( $P_{ac,ref2}$ ), which aims to minimize the deviation of power system frequency due to fluctuations in generation. The ac power order reference setting ( $P_{ac,ref, set}$ ) provides the reference level for power to be dispatched from the PV plant at the point of connection. The control block diagram associated with the moving average and the droop controller is shown in Figure 5.1.

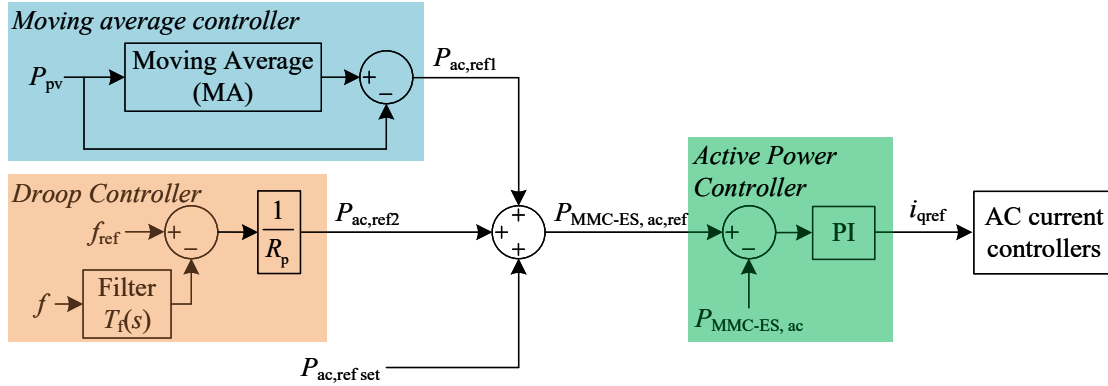


**Figure 5.1:** Power smoothing controller.

### 5.1.3 Verification of Controller

#### Studied System

A schematic diagram of the studied system is shown in Figure 5.2. The MMC-ES is modelled as shown in section 4.3.2 [58] for efficient simulation. The dc link of the MMC-ES is formed with a dc voltage source. The main ac grid is simulated using a synchronous machine with relatively low inertia to observe the variations of frequency. The PV power plant is simulated as three two-stage inverters operating in parallel. The PV plant is connected to the main grid via a transmission line, which is modeled as a  $\pi$ - section. The parameters of the MMC-ES, PV system, and synchronous machine are shown in Table 5.1.

#### Simulation Results

A test is performed with real solar insolation data over a period of 300 s (Figure 5.3). The solar irradiance data is obtained from [76]. The impact of the solar irradiance variation on power system frequency and synchronous machine's speed is observed. The test is performed without any ancillary support from MMC-ES (constant 0.5 pu power supplied), with moving



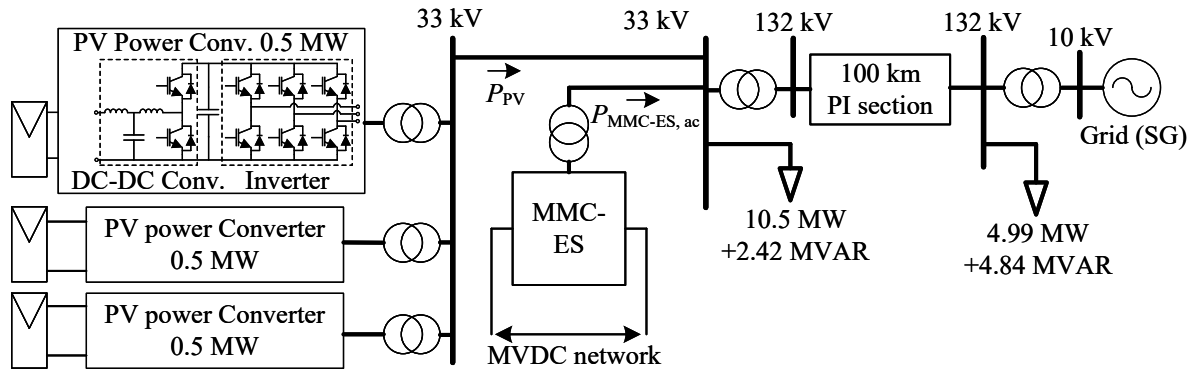


**Figure 5.2:** Schematic diagram of the studied system.

**Table 5.1:** System parameters - Case study 1.

<b>MMC-ES Parameters</b>			
Power rating	10 MW	Number of SMs per arm	15
SM capacitance	15 mF	Pole-to-pole dc link voltage	15 kV
Battery voltage	500 V	Arm inductance	0.5 mH
Converter ac voltage	$8 \text{ kV}_{\text{ll,rms}}$		
<b>PV System Parameters</b>			
PV module	KU330-8BCA	Number of modules in a string	15
Number of strings in parallel	100	PV inverter power rating	0.5 MW
Inverter dc link voltage	1 kV	Inverter ac voltage	480 V
Total rated PV power	1.5 MW		
<b>Synchronous Machine Parameters</b>			
Inertia	5 s	Governor droop	5 %
Power rating	20 MVA	Rated frequency	60 Hz

average (MA) power smoothing controller only, droop controller only, and finally with both MA and droop controllers. The MMC-ES exports 0.2 pu of power to the MVDC link as well. Figure 5.4 shows the power distribution among different sources under different control schemes. It is observed that enabling the MA controller allows to rapidly smooth out the variations in the solar PV power. The droop controller further allows for smoothing of the power injection into the system. The variations in the PV power or the ancillary support provided by the MMC-ES for the ac network do not affect the power export to the dc network. Thus the converter is able to operate as a three-port converter that independently controls power using the energy reserve in its embedded batteries. The impact of the controllers is better visualized by observing the network frequency captured by the PLL and the synchronous machine speed. Figure 5.5 shows the power system frequency and machine speed variations with different control systems enabled. As expected, the average frequency is different due to the droop function. Large and rapid variations in the frequency are observed without any support actions. The MA controller reduces the frequency spikes partially and smooths out the frequency change. With only the droop function, the frequency spikes are reduced, although sudden changes still happen. When both the MA and droop controller are enabled, highly smooth frequency and machine speed are observed.

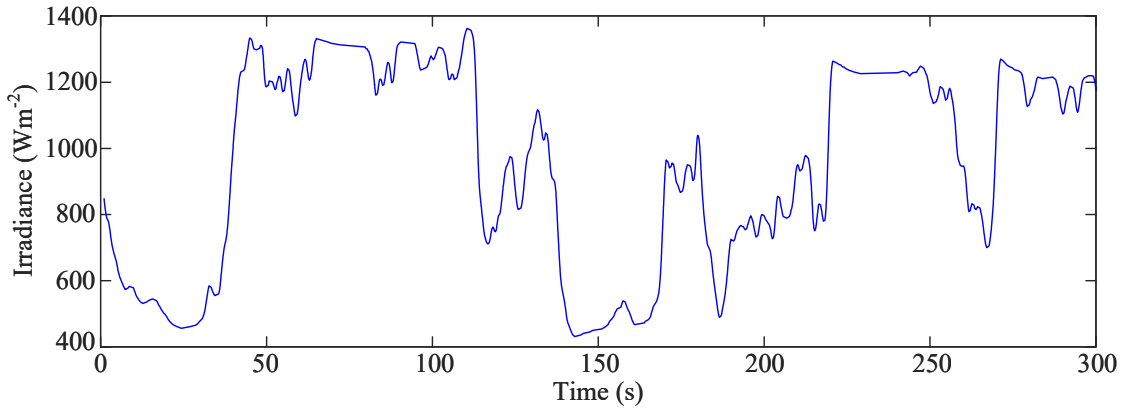


**Figure 5.3:** Considered irradiance profile - Case study 1 [76].

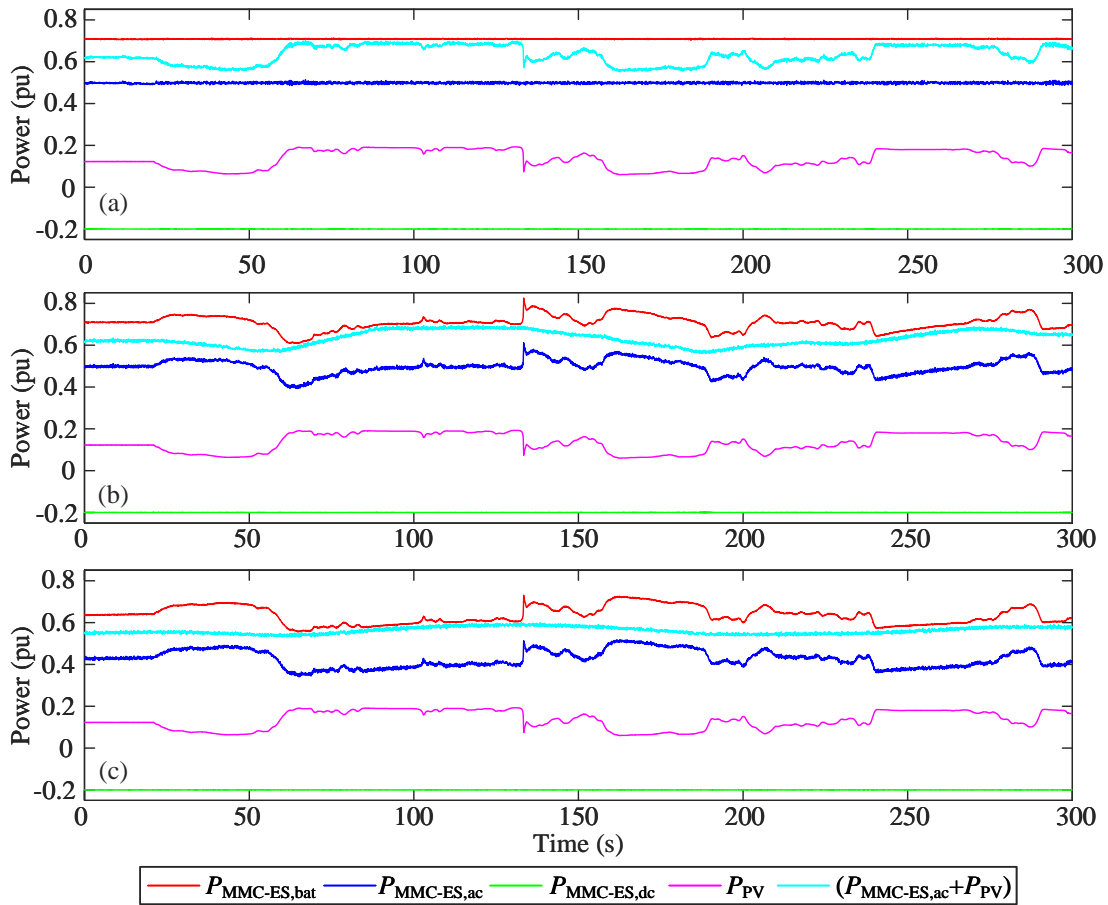


**Figure 5.4:** Power distribution in MMC-ES - Case study 1 (a) no ancillary service from MMC-ES (b) Only enable MA controller ( $P_{ac,ref2} = 0$ ) (c) enable both MA controller and droop controller.

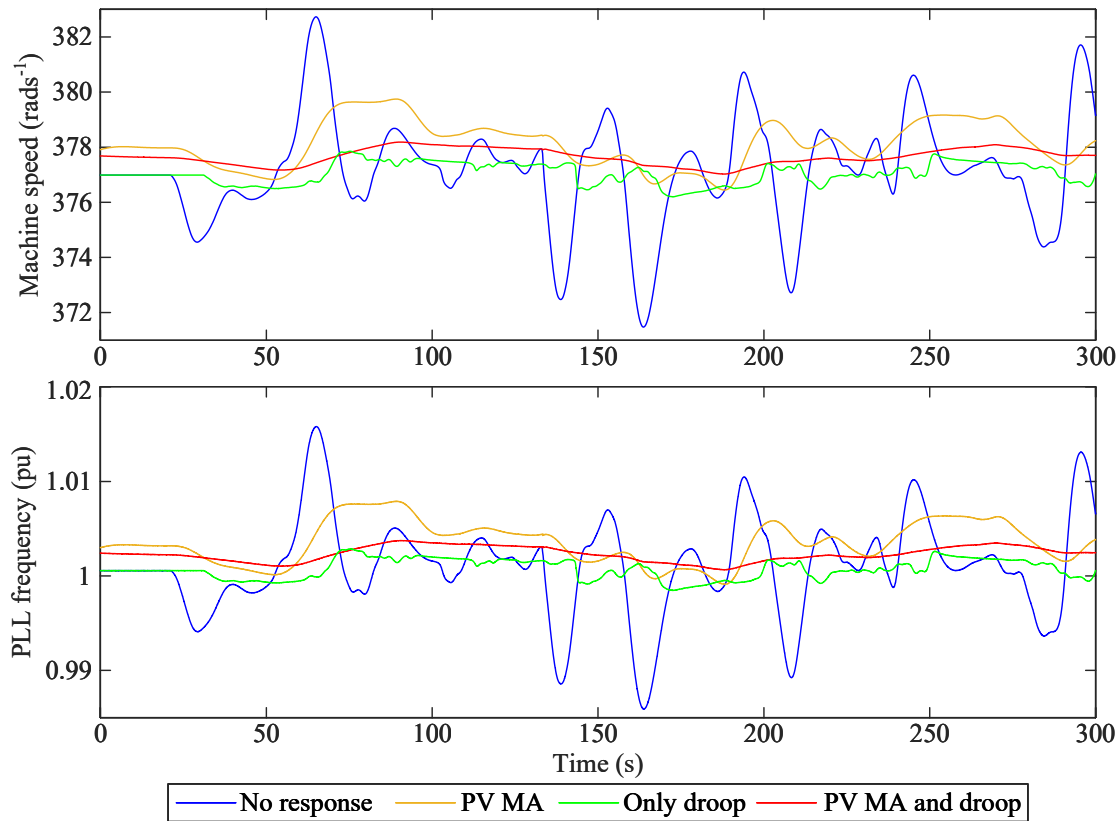


**Figure 5.5:** Frequency under different control systems - Case study 1 (a) machine speed (b) PLL frequency.

### 5.1.4 Summary of Case Study 1

In this case study, an MMC-ES is used to smooth out power output fluctuation in a PV plant due to variations in solar insolation. The MMC-ES has been able to rapidly control ac power and also transfer power into a MVDC network. EMT simulations validated that the MMC-ES is able to operate as a three-port converter, interchanging power between a MVDC network, an ac network, and the battery units. Further simulations based on the MA power smoothing controller and droop controller showed the ability of the proposed control system in damping the frequency deviations due to variations in solar irradiance in a power system

with high penetration of PV power. The findings of this section are presented in [77].

## **5.2 Case Study 2: Use of MMC-ES in HVDC Bi-pole to Increase Redundancy and Provide Frequency Support**

In this study, an HVDC link formed with two MMC-ES converter stations is considered. One MMC-ES station is operated to maintain the HVDC pole voltage (inverter) and the other station controls the ac active power and dc power injected into the HVDC system (rectifier). Both stations have embedded battery energy storage. The rectifier is connected to an ac system with low short-circuit capability and relatively low inertia, while the inverter end is connected to a strong ac system with relatively high inertia. A solar PV power plant is connected to the weak ac network (rectifier end) with an ac transmission line. The schematic diagram of the test system is shown in Figure 5.6. System parameters are shown in Table 5.2

### **5.2.1 Solar PV Plant**

Utility-scale solar PV integration can be done in different topologies such as central inverters or string inverter topology [78]. String topology directly connects small inverters to PV panel strings and feed power to the ac feeder. The central topology collects the power from PV panels in dc form and uses a central inverter to invert power to ac. Due to the large number of inverters in the system, string topology is highly redundant, and has greater performance during partial shading, but incurs large capital cost as well as operating cost (labour intensive

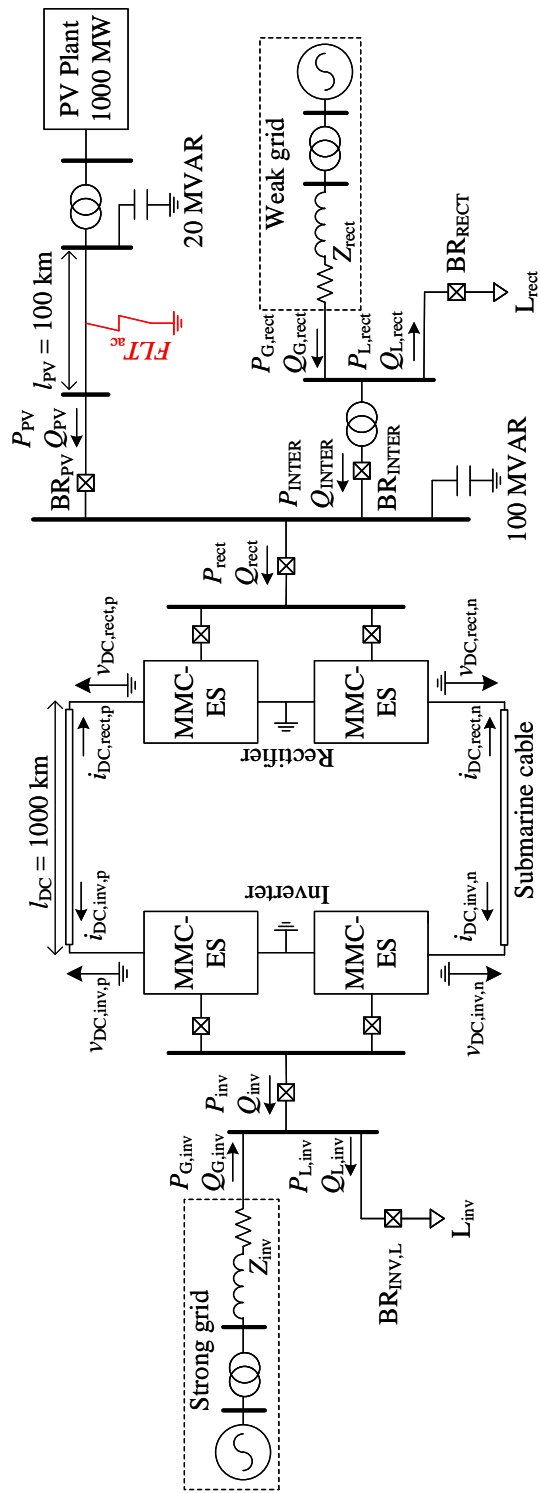


Figure 5.6: Schematic diagram of studied HVDC with MMC-ES system

**Table 5.2:** System parameters - Case study 2.

<b>MMC-ES Parameters</b>			
Power rating per pole	500 MW	Number of SMs per arm	300
SM capacitance	8.062 mF	DC voltage	$\pm 525$ kV
Battery voltage	1 kV	Arm inductance	64.4 mH
Converter ac voltage	300 kV <sub>ll,rms</sub>		
<b>PV Plant Parameters</b>			
PV module	KU330-8BCA	Single inverter power rating	5 MW
DC capacitance ( $C_{PV}$ )	6 mF	Filter inductance ( $L_f$ )	25.25 $\mu$ H
Filter capacitance ( $C_f$ )	4.012 mF	Filter damping inductance ( $L_d$ )	0.126 mH
Filter damping capacitance ( $C_d$ )	2 mF	Filter damping resistance ( $R_d$ )	0.25 $\Omega$
Inverter dc link voltage	1.2 kV	Inverter ac voltage	690 V
Total rated PV power	1.0 GW	Transmission line length	100 km
<b>Rectifier AC System Parameters</b>			
Inertia	3.5 s	Governor droop	5 %
Short circuit ratio	4 $\angle$ 75 $^\circ$	Rated frequency	60 Hz
<b>Inverter AC System Parameters</b>			
Inertia	4 s	Governor droop	5 %
Short circuit ratio	8.21 $\angle$ 76.3 $^\circ$	Rated frequency	60 Hz
<b>DC Cable Parameters</b>			
Length	1000 km	Depth below sea floor	1.5 m
Cable horizontal displacement	0.2 m	Insulation	XLPE

to repair or replace inverters in a large power plant). Central inverters reduce redundancy, and face some limitations during partial shading, but have lower operating and maintenance costs. Thus, in this case study, central inverters are selected as the topology of choice.

### **EMT Simulation Model**

A single-stage 5 MVA central inverter from FIMER (PVS980-58 5.0 MVA-5000kVA-L) [79] was selected as a guide for the inverter design. The product specifications were extracted and used in designing the solar PV inverter. The ac filter was designed as shown in [80]. A perturbation and observation maximum power point tracking algorithm is used in the PV inverter to track for the maximum power point.

A power plant of 1000 MVA is implemented by parallel connection of 200 of such converters. However, this drastically increases the number of nodes in the admittance matrix of the circuit resulting in prohibitively slow simulations. Modelling inverters as controllable voltage sources could reduce the switching events of the converter and model the average response of the converter. However, the high number of averaged value models still adversely affects the simulation.

One approach to overcome this issue is to rate the solar PV inverter to a larger value and design the quantities appropriately. This causes converter and filter parameters to be impractical values and a re-evaluation of the measured quantities is required to compare with an actual converter. Another approach is to use a current-dependent current source scaling component to scale the current output of a 5 MVA converter. This approach reduces the number of nodes and components in the simulation, while allowing the use of practical converter parameters. It also allows the user to observe the parameters of a 5 MVA inverter without any conversion. This method is used in this case study.



Figure 5.7 shows the schematic diagram of the 1 GW PV plant. The transformer  $TF_2$  is rated for a 5 MVA PV inverter (0.69 kV/33 kV, 5 MVA, 5%), while transformer  $TF_1$  is rated for a 1 GW PV plant (33 kV/132 kV, 1275 MVA, 1%). The scaling is done with  $n = 200$ .

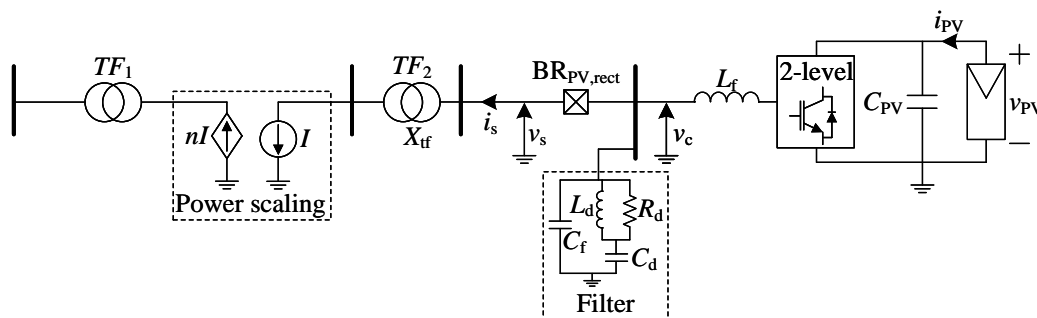


**Figure 5.7:** Schematic diagram of the PV plant.

## Control System

The control system associated with the PV inverter is shown in Figure 5.8. A decoupled current controller is used to control the inverter current. Outer control loops are designed to control the PV panel voltage ( $v_{PV}$ ) and reactive power, which drive the current references  $i_{sq,ref}$  and  $i_{sd,ref}$ , respectively. An MPPT tracker calculates the PV panel voltage reference. The breaker  $BR_{PV,inv}$  is initially open and needs to be closed for the PV plant to be made operational. Until the breaker closing signal is issued, the current controllers are disabled and the synchronizer module attempts to match the voltage on the two sides of the breaker ( $v_s$  and  $v_c$ ) using PI controllers by directly creating modulation waveforms. After a delay following the breaker closing signal (around 200 ms) the current controllers are enabled and the synchronizer is bypassed. The current references are kept at zero. After allowing some time for the small transients to die out, the  $v_{PV}$  controller and reactive power controller are enabled and current references are switched on to these controllers. In Figure 5.8,  $\theta_{PLL}$  is

the phase angle of  $v_s$  derived from a phase locked loop (PLL). Figure 5.9 shows simulation waveforms of the PV plant’s startup. The breaker is closed at  $t = 0.5$  s and “Delay 1” and “Delay 2” are, respectively, 0.2 s and 1.05 s. It is observed that the PV plant can be connected to the system without any large transients.

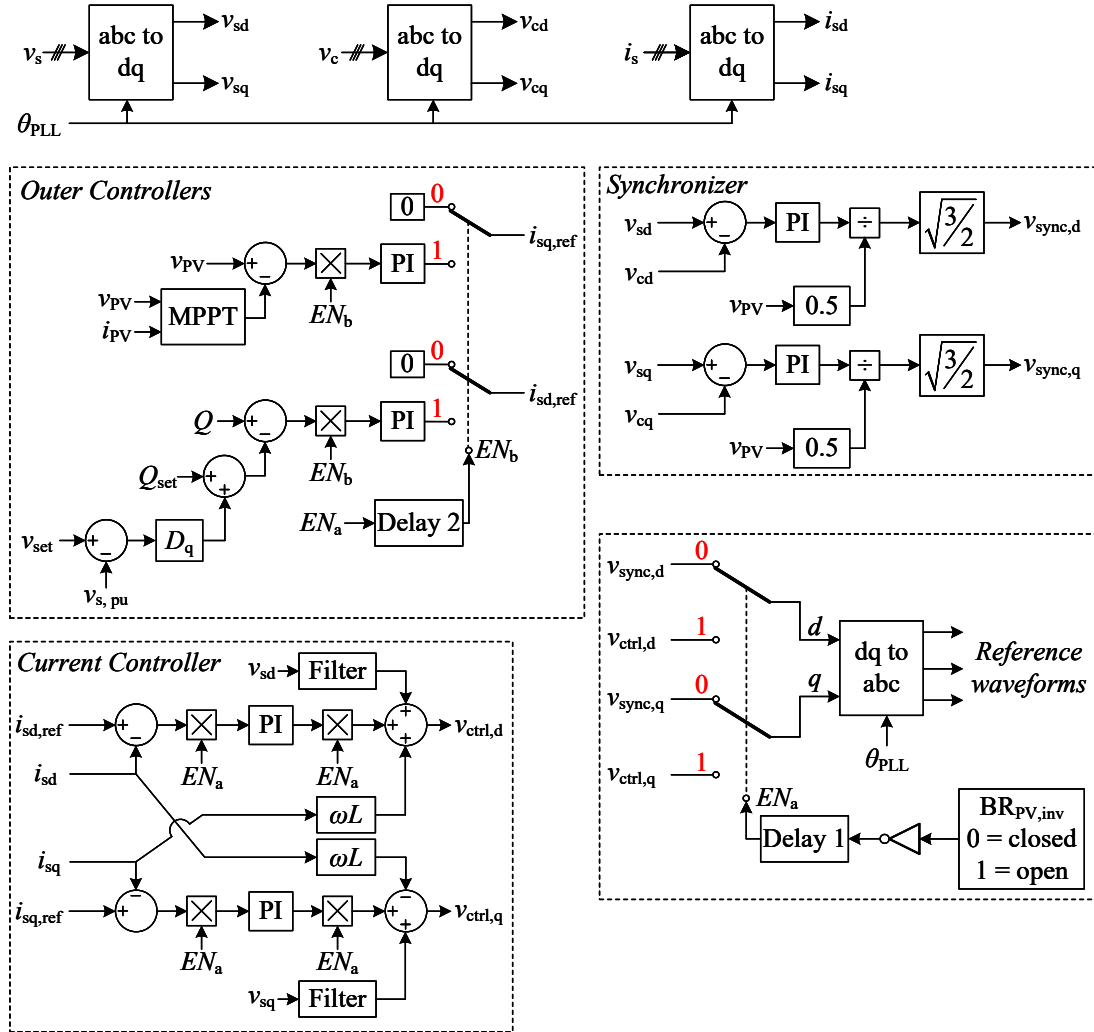
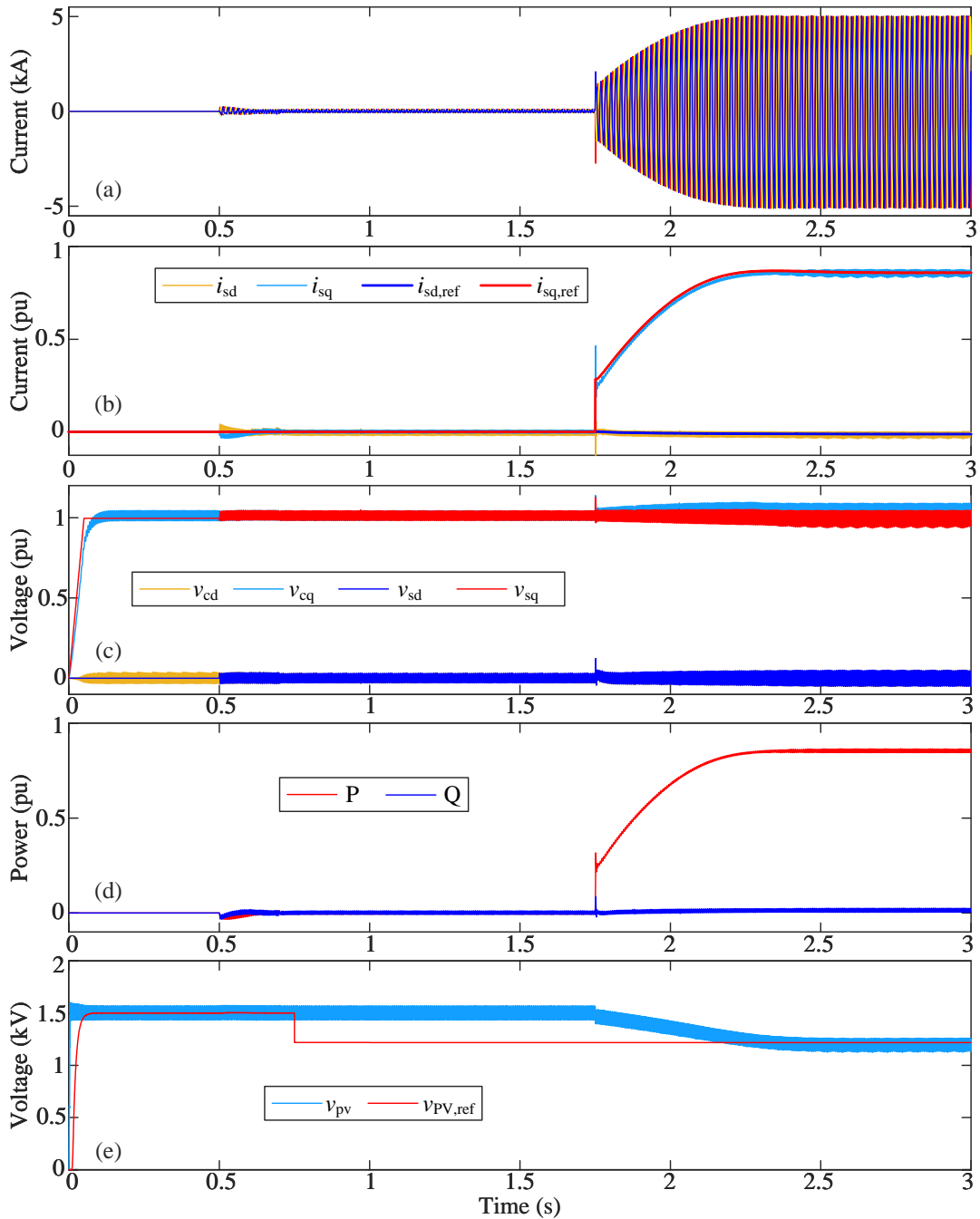


Figure 5.8: PV inverter controller and synchronizer - Case Study 2.



**Figure 5.9:** Simulation results of PV inverter synchronizing - Case Study 2.(a) inverter current, (b) inverter current in  $dq$  domain, (c) PCC bus voltage in  $dq$  domain, (d) inverter active and reactive power, (e) PV panel voltage against MPPT voltage reference.

### 5.2.2 DC System

The power generated by the PV plant is exported to a large power system using an HVDC transmission system. MMC-ES converters are used at both ends of the HVDC system. Two MMC-ES converters are used at each end to construct the bi-pole. Different control objectives as shown in Table 5.3 are assigned to each converter end.

**Table 5.3:** Control objectives of different parameters of MMC-ES.

Control Parameter	Rectifier	Inverter
Decoupled $q$ axis current reference ( $i_{q,ref}$ )	Control ac power ( $P_{ac}$ )	Control dc pole voltage ( $v_{DC,inv}$ )
Decoupled $d$ axis current reference ( $i_{d,ref}$ )	Control reactive power ( $Q$ ) and support ac voltage ( $v_{ac}$ )	Control reactive power ( $Q$ ) and support ac voltage ( $v_{ac}$ )
DC component of circulating current ( $i_0^{circ}$ )	DC power injected to the inverter ( $P_{dc}$ )	Not controlled
SM dc-dc converters	Control the average SM capacitor voltage ( $v_{C,avg}$ ) with a feedforward term to inject SM power reference	Control dc-dc converter inductor current to obtain desired amount of power from batteries.

For long distance submarine power transmission, HVDC has been the method of choice due to its ability in addressing system stability issues, cable charging concerns, etc. The power system studied in this case study was inspired by the Sun Cable project [81]. The power rating of the HVDC system requires the use of high dc voltages above 300 kV per pole. The long transmission distance of 1000 km requires the reduction of dc transmission losses; thus a dc voltage of 525 kV per pole is selected. This design keeps in line with the Viking Link transmission system of 1400 MW spanning approximately 760 km between Denmark and Great Britain, which uses 525 kV per pole [82]. SAPEI HVDC cable between mainland

Italy and Sardinia has a power rating of 1000 MW with a bipolar voltage configuration of  $\pm 500$  kV. Its total length is 420 km.

There are two types of dc cables used for HVDC projects in this scale: cross-linked polyethylene (XLPE) and mass impregnated insulation, non-draining compound (MIND). The SAPEI project has used MIND cables while the study done in [83] has suggested using XLPE cables for the Viking Links project. The same cable with dimensions used in Viking Links project has been used in this case study where the cable is modeled with a frequency-dependent representation in PSCAD/EMTDC. The parameters of the cable are extracted from [83] and are reported in Table 5.4.

**Table 5.4:** XLPE cable parameters.

<b>Cable Parameter</b>	<b>Value</b>
Stranded conductor	Cross sectional area = 2500 mm <sup>2</sup> Diameter = 59.5 mm
Thickness of inner conductive layer	1.8 mm
Insulation thickness (XLPE)	26.0 mm
Thickness of outer conductive layer	2.0 mm
Tape	0.5 mm
Lead sheath	5.0 mm
Inner PE jacket	5.0 mm
Tape	0.5 mm
Armour	7.0 mm
Outer jacket	5.0 mm

### 5.2.3 MMC-ES Ancillary Services Control System

The main objective of the MMC-ES for transmission of solar PV power (instead of regular MMC) is the use of embedded storage to provide ancillary services. This is achieved by manipulating the power references. Depending on the control objectives of the inverter and rectifier, the power command is manipulated. The rectifier control objective is to control the active power and reactive power; thus active and reactive power commands to provide ancillary services can be directly appended to the original power controllers. However, the inverter's main objective is to maintain the dc link voltage and control reactive power, which requires an alternative path to control the active power support to the ac network. The reactive power support could be done as in the case of the rectifier; however, active power transfer is determined by the dc power received to the inverter from the rectifier end. The battery power can be controlled by changing the dc-dc converter's inductor current and this could be used to provide ancillary services to the ac network of the inverter.

The ancillary services implemented in this case study are shown in Figure 5.10. The  $P_{\text{ref,aux}}$  term in Figure 5.10(a) is used to add a power reference from additional controllers such as the moving average PV power smoother (Figure 5.1) .

### 5.2.4 MMC-ES Protection System

A simple protection system is implemented for the safe operation of the MMC-ES. This system relies on local voltage and current measurements of the MMC-ES. DC voltage fault detection, dc current fault detection and ac fault detection are implemented. Once a fault is detected the converter is blocked and the converter's ac breakers are signaled to open to reduce any damage to the MMC-ES.

A very large deviation in the dc voltage could result in discharge of SM capacitor voltages

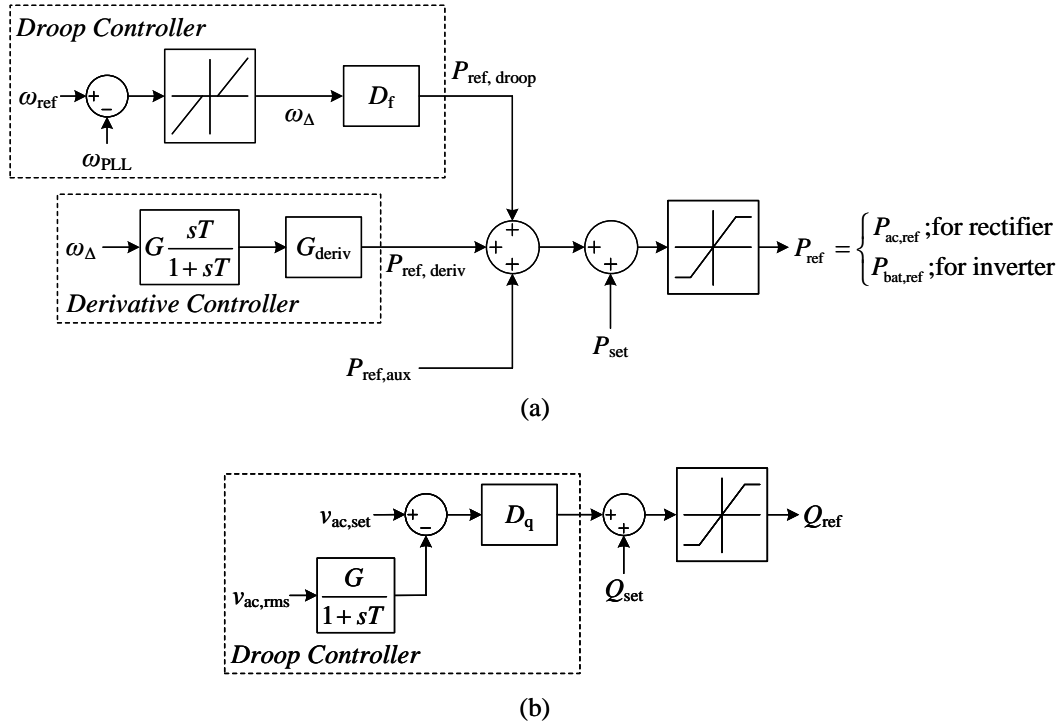


**Figure 5.10:** Ancillary support controllers - Case Study 2 (a) active power support, (b) reactive power support.

and currents in the system, which could lead to abnormal operation of the converter. Thus the normal operating dc voltage is set between 0.9 pu and 1.1 pu. If the pole voltage violates this region for more than 5.0 ms, the converter block signals are issued and converter breakers are opened.

Similarly, the magnitude of the dc current is observed at each converter station. If the magnitude of dc current exceeds 2.0 pu for more than 5.0 ms, the MMC-ES is blocked and signals are issued to open the ac breaker of the MMC-ES. This protective measure is taken mainly in order to safeguard the semiconductors of the MMC-ES.

Low voltages in the ac power system are caused by faults in the ac network. In synchronous machine-dominated power systems, inverters are allowed to be temporarily dis-

connected from the ac network, following a disturbance in ac voltage; and thus they are not required to ride through the fault. However, with increasing penetration of inverter-fed generation, disconnecting inverters from the network during an ac fault could lead to loss of large amounts of active power from the system, which could in turn result in frequency instability. This concern was highly relatable to distributed generation schemes such as solar PV and on-shore wind turbine interconnections. As a result, guidelines have been developed to specify the low voltage fault ride through requirements of the inverters connected to the system. IEEE 1547 [84] was introduced for interconnecting distributed resources upto 10 MVA. Standards were proposed by industry such as American Wind Energy Association (AWEA) and the Western Electricity Coordinating Council (WECC) for larger generators above 20 MW. The Federal Energy Regulatory Commission (FERC), regulated these proposals and created the guideline shown in Figure 5.11 for low voltage ride through (LVRT).

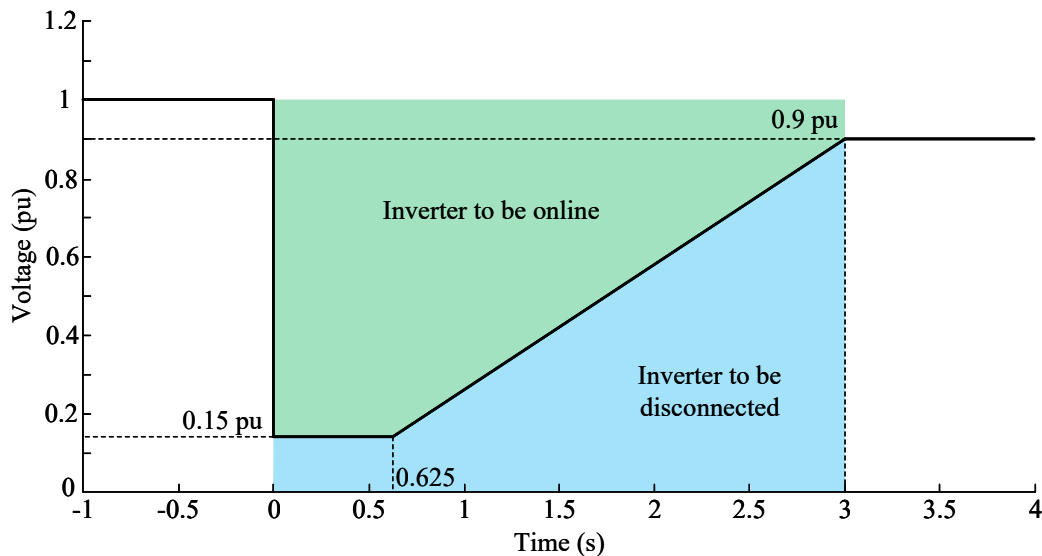


**Figure 5.11:** LVRT guideline developed by FERC.



### 5.2.5 Simulation Experiments

This section presents several simulation experiments to observe the operational behaviour of MMC-ES with large penetration of solar PV generation. The impact of the loss of PV generation is studied for cases with and without embedded storage in MMC. The impact of ancillary controllers are studied, and ancillary services with a dedicated communication line is studied. Studies are also conducted to find out the power quality improvement with the MMC-ES when solar PV plant is subjected to a highly variable solar irradiance profile.

#### Loss of Solar PV Transmission Line for MMC-ES vs Regular MMC

A solid three-phase-to-ground fault is simulated at the mid-point of the solar PV transmission line. The PV line is tripped manually 5 ms following the fault. The droop and derivative frequency support actions are enabled. Studies are conducted for cases using regular MMC (labelled as Reg. MMC) and MMC-ES for dc power transmission. The impact of the protection system on the loss of inverter generation is also observed. Figure 5.12 shows the system's response following the fault for both inverter and rectifier stations, and Figure 5.13 shows the active and reactive power variations. It is observed that the loss of PV generation causes a drastic change in the dc current in regular MMC and thus the dc power transmitted from rectifier (Figure 5.12(c,d)). The ancillary services gradually ramp the power and restore it to the original power setting in the rectifier end. However, this transient is slow and causes a considerable frequency change in the inverter-end systems as large amounts of power are lost from the dc link. On the other hand, MMC-ES is able to continuously provide dc power without any disturbance, which eliminates any disturbance in the inverter's ac grid frequency. The fault has caused a drop in the dc link voltage for the regular MMC option and this results in detection of dc link under voltage detection and blocking the MMC. These

responses immediately show the advantage of using a MMC-ES instead of regular MMC in transmitting power. The reliability of power export to the inverter end can be increased, even following a considerable loss of generation, with minimum disturbance. The embedded storage provides power until other forms of generation can be ramped up at the inverter end.

### Communication Link from PV Feeder to MMC-ES

The MMC-ES is used as a rectifier to transmit a large amount of renewable generation from the ac network. The HVDC link is not expected to provide power to the rectifier-side ac system as the local generation is expected to meet the local demand. Thus a controller can be made using a communication link between the MMC and PV transmission feeder to only absorb the power coming from the PV line. The rectifier will export dc power according to the operator's set point ( $P_{dc,set}$ ) and the difference between the moving averaged PV power production ( $P_{PV,MA}$ ). This ensures that there are no high variations in the rectifier-side ac network as variations from PV power are absorbed by the MMC-ES and the inverter side does not observe large variations in power. A battery power set-point calculation method is also implemented in the inverter side. This controller is implemented to detect any sudden changes in dc link power and boost the battery power in the inverter end until auxiliary generators are brought online. The power set point calculation methods for rectifier and inverter MMC-ES are shown in Figure 5.14(a) and (b), respectively.

The communication link is modeled using a sampler of constant frequency (20 kHz) and a time delay ( $T_1 = 1$  ms). In this controller  $T_2$  and  $\alpha$  are selected as 1 s and 0.8, respectively.

Figures 5.15 to 5.17 show the system response to a fault at  $t = 60$  s in the solar PV transmission line followed by a line trip after 50 ms. In these figures, a simulation case with communication line (With Com. link) and without communication line (Without Com. link)

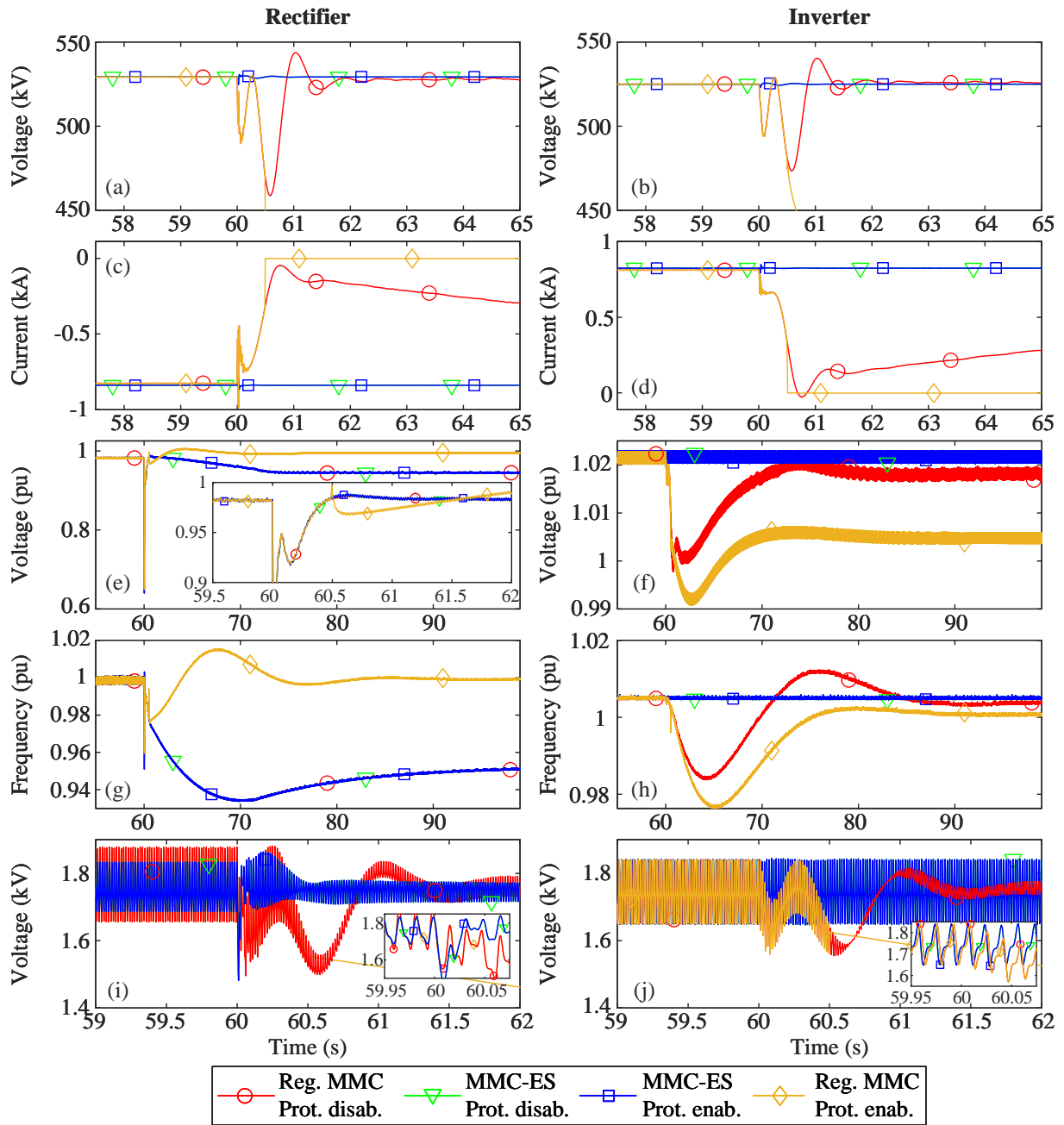


**Figure 5.12:** Response of the dc system for a fault on ac transmission line followed by line tripping - Case Study 2. (a,b) dc positive pole voltage, (c,d) dc positive pole current, (e,f) ac rms voltage at converter, (g,h) ac system frequency-from PLL, (i-j) SM capacitor voltage

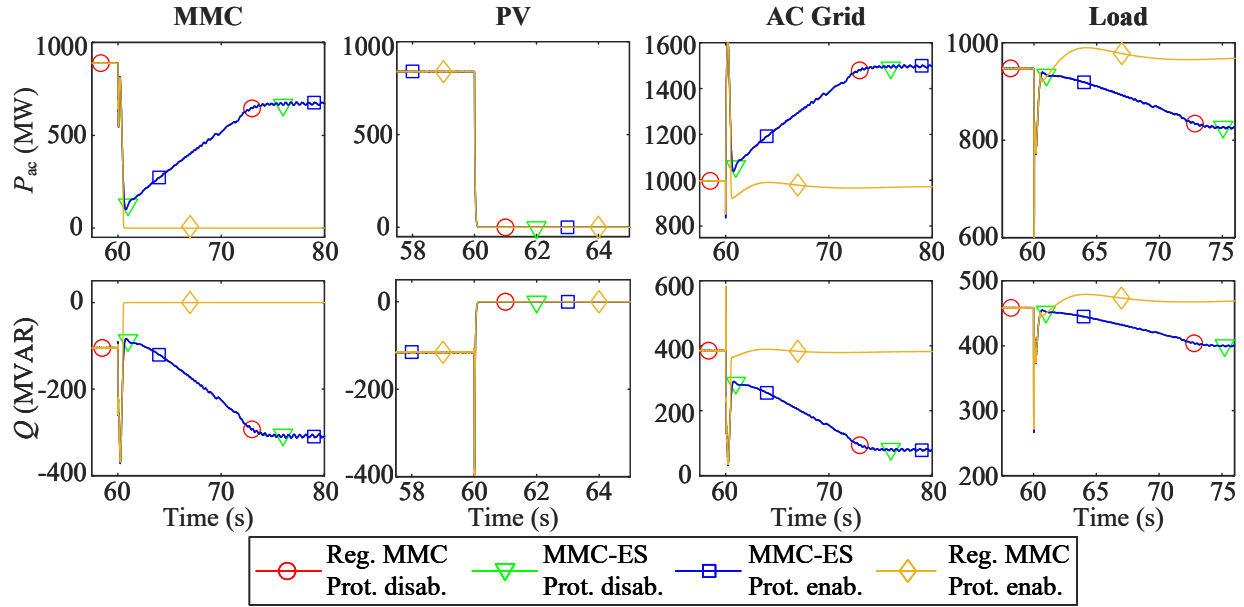


**Figure 5.13:** Rectifier end active and reactive power variation following the loss of generation - Case Study 2.

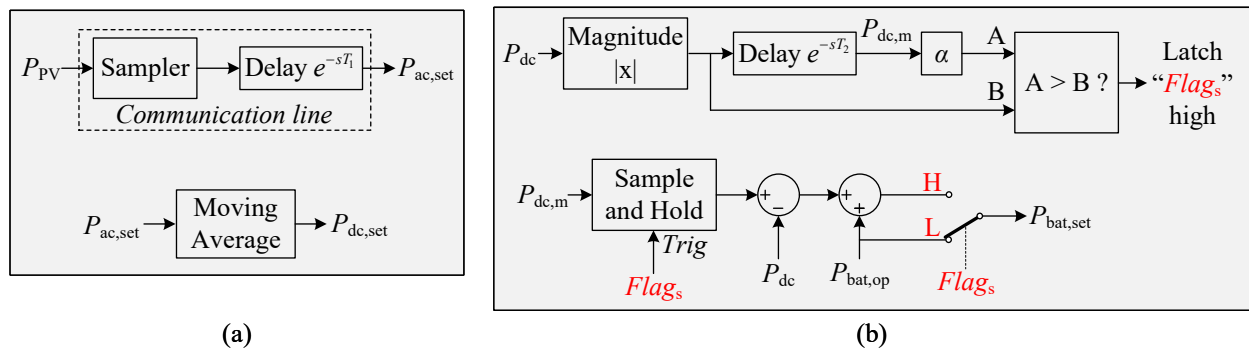


**Figure 5.14:** Power set point calculators with the communication link - Case Study 2 (a) rectifier end (b) inverter end

are compared. In the case without communication line, the power references for inverter and rectifier are set to the average values as with the case with the communication line.

It is observed that when the solar PV line is tripped following a fault, the communication link helps to reduce the MMC-ES power absorption from the ac system rapidly. This helps to reduce the rate-of-change-of-frequency (ROCOF) as well as the frequency change in the system. In the case without a communication link, the ancillary services act based on the measurement of system frequency using a PLL. This process is drastically slower than the communication link. Based on the proposed power set-point calculation method, although the PV power suddenly drops at 60 s, the batteries in the rectifier MMC-ES smoothly dampen the dc power reduction. Compared to the case without communication link, the new system rapidly ramps the battery currents and support both ac and dc networks. The large loss of PV power does not affect the system frequencies or ac voltages in both systems. No additional loading on the ac system generators in inverter end are also observed.

Next the impact of a solar irradiance profile on the power system is analyzed. A highly variable solar irradiance profile is obtained from [76] based on local measurements. With the irradiance profile, three different case studies are conducted and compared. Cases 1 and 2 use regular MMC to form the solar power transmission HVDC system and case 3 uses MMC-ES. Cases 1 and 3 use the power set-point calculators shown in Figure 5.14; but the dc power controller for rectifier is disabled and battery power set-point calculator is disabled for cases 1 and 2 (as they are for regular MMC). For case 2, the ac power set-point ( $P_{ac,set}$ ) is calculated directly by taking the moving average of the measured PV power injection. The response of the system for the irradiance profile is shown in Figure 5.18.

It is seen that for cases 1 and 3, the rectifier end synchronous machine speed remain quite constant compared to case 2 as the instantaneous PV power fluctuations are exported

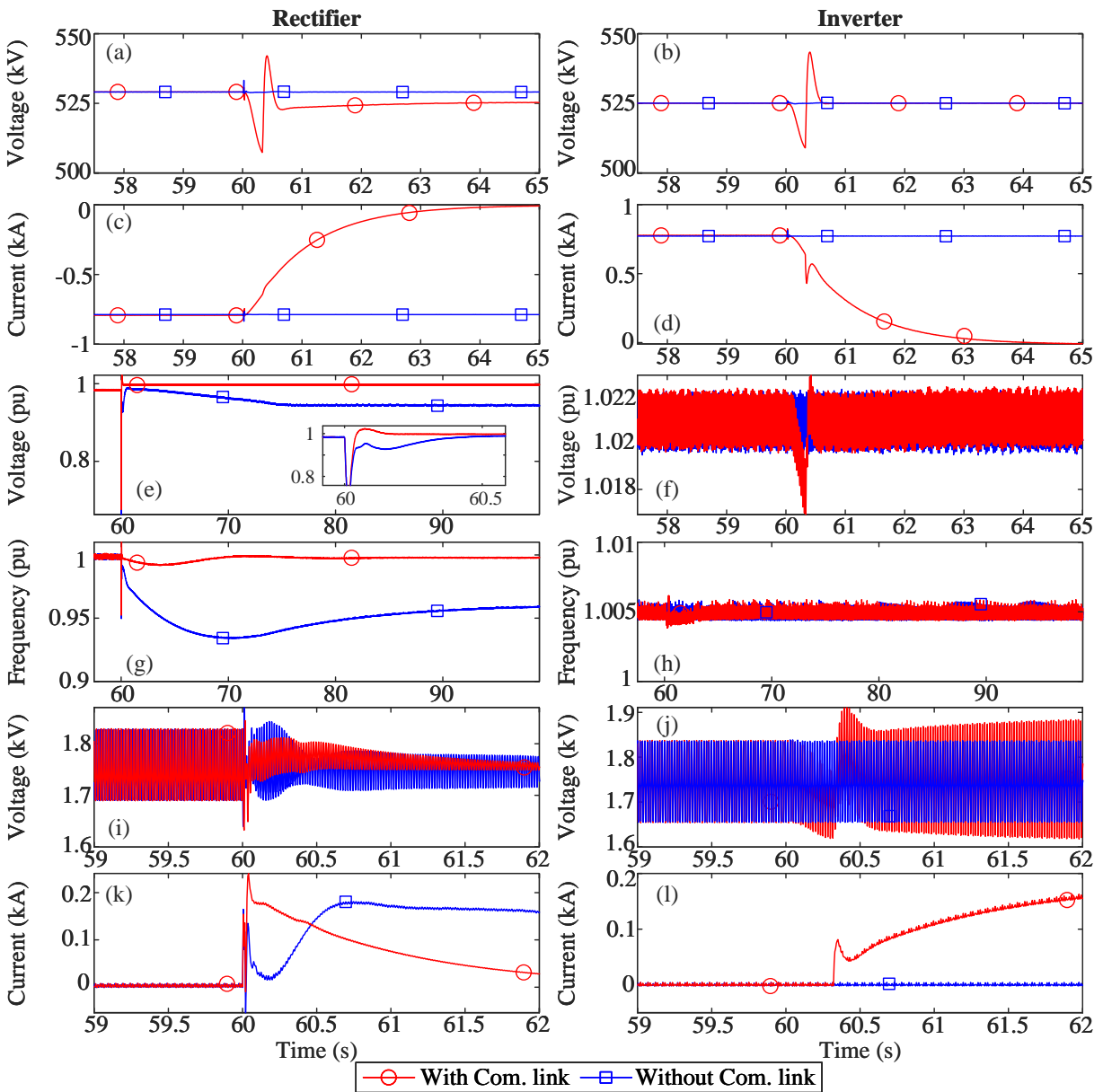


**Figure 5.15:** Comparison of simulation data with and without a communication line - Case Study 2. (a,b) dc +ve pole voltage (c,d) dc +ve pole current (e,f) MMC-ES ac bus voltage (g,h) ac network frequency captured by PLL (i,j) average SM capacitor voltage (k,l) SM average battery current

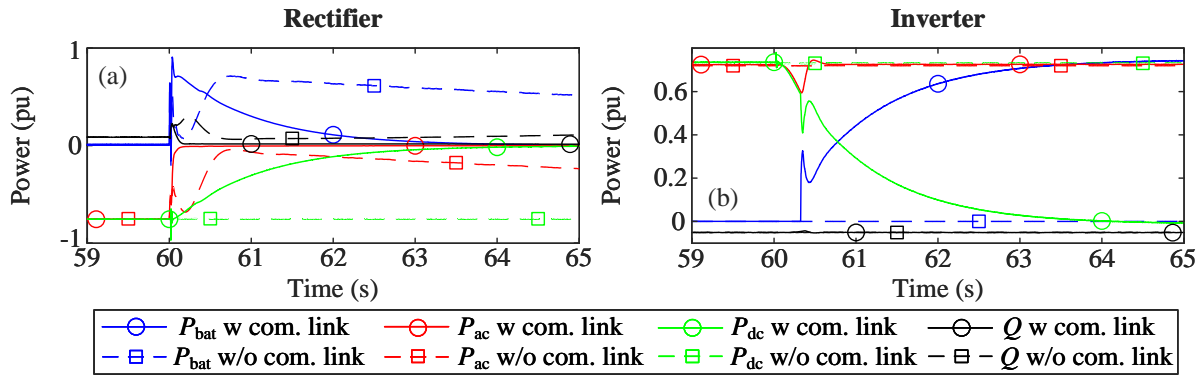


Figure 5.16: MMC-ES power distribution with and without a communication line - Case Study 2. (a) inverter MMC-ES (c,d) rectifier MMC-ES

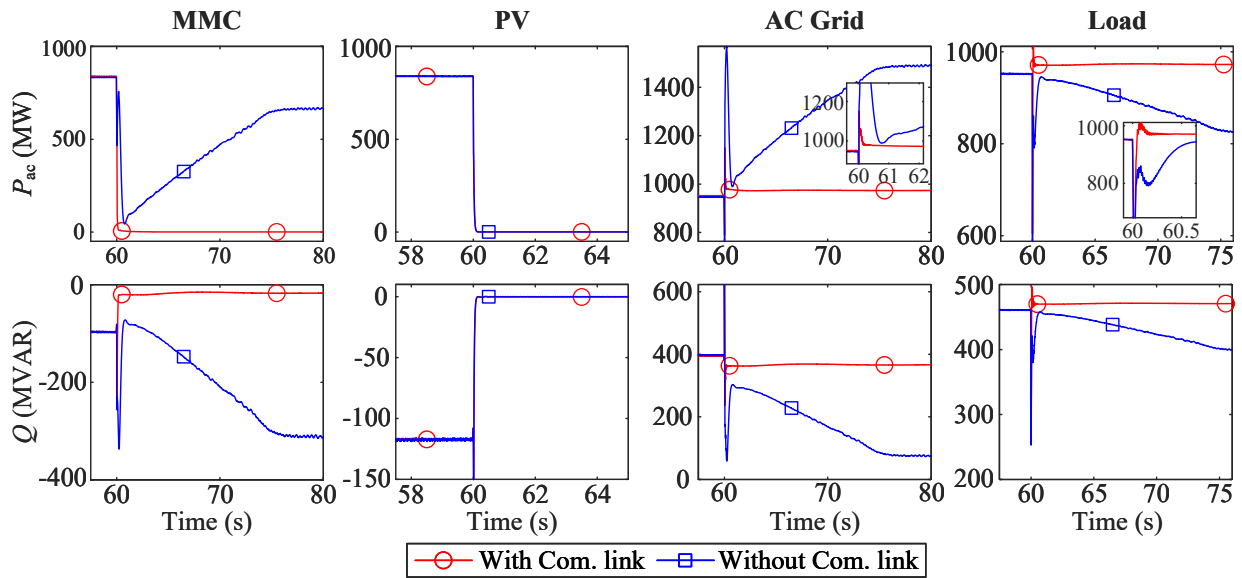
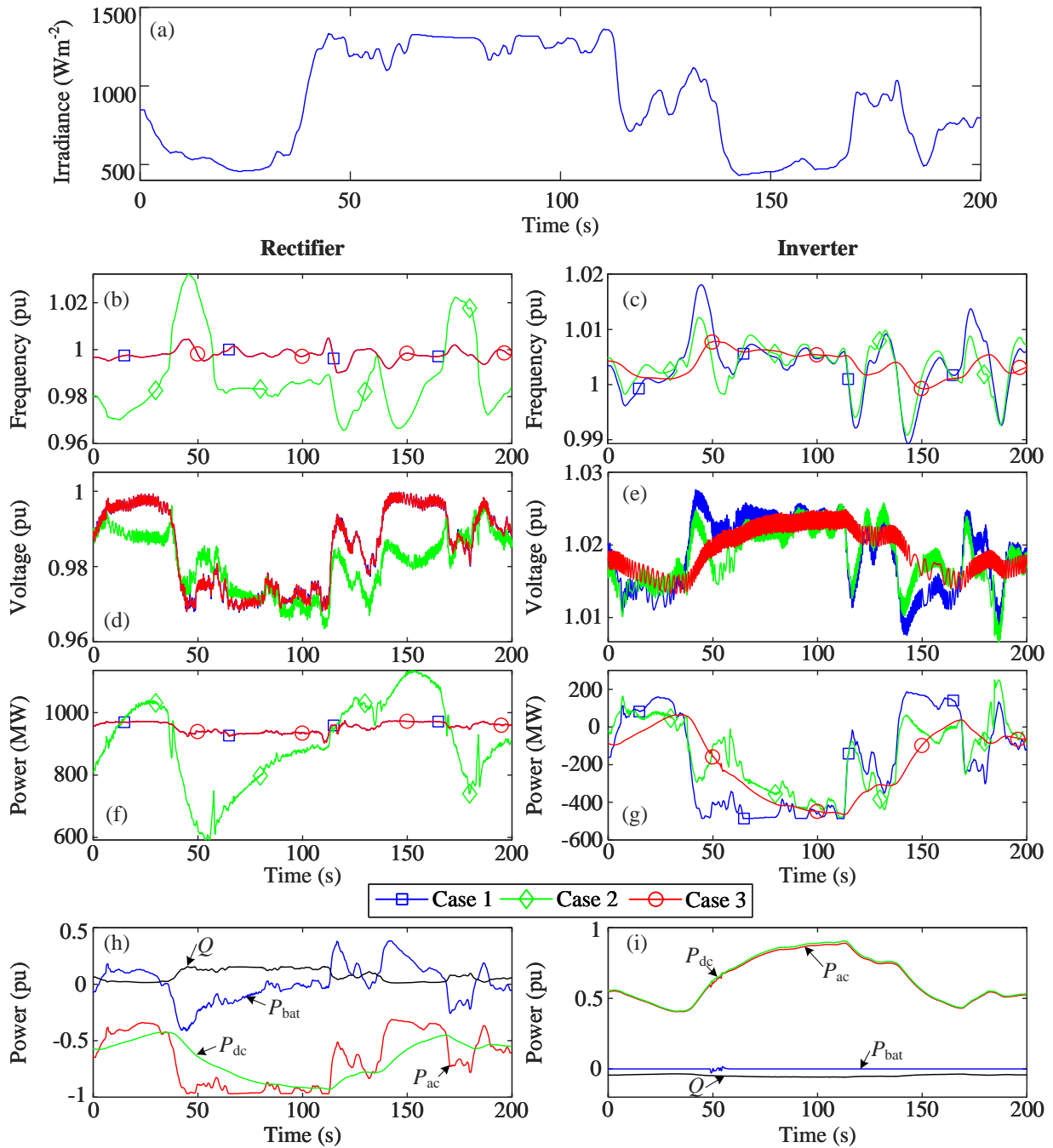


Figure 5.17: Power distribution in busses in rectifier end - Case Study 2.



**Figure 5.18:** System response to an irradiance profile - Case Study 2. (a) tested irradiance profile (b,c) grid synchronous machine speed (d,e) converter ac bus voltage (f,g) power output of equivalent grid (h,i) power distribution in MMC-ES for case study 3.



by the dc system. The average PV power export in case 2 results in larger speed fluctuations in the rectifier end. The inverter end observes large speed variations for case 1 since the PV power variations are now directly reflected in the inverter end. Since the inertia of the inverter end is comparatively high, speed variations are somewhat lower than those in the rectifier end. Case 3 with energy storage has been able to maintain low speed variations in both ac systems. The voltage profile follows identically for cases 1 and 3 for rectifier end, but case 2 observes lower voltage variation in rectifier end. The inverter end observes large voltage variations in case 1 and 2 due to the highly variable power injection from the HVDC link. The slowly-varying dc power output of the rectifier has caused low variations in the ac voltage profile for case 3.

The variation of active power from the equivalent ac network for the rectifier end is quite low for cases 1 and 3 due to the nature of PV power exported. However, since the moving average of PV power is exported in case 2, large power variations to make up for the lost power due to irradiance variation is taking place in case 2. The inverter-end ac network's power variation has been low for case 3 but cases 1 and 2 observe highly variable power outputs/adsorptions due to the variable nature of the power in the dc network. However, since most of the PV power fluctuations are reflected on the rectifier network, the power variation for case 2 is low compared to case 1.

Figure 5.18 (h,i) show the power distributions with the MMC-ES for case 3. In this figures it can be observed that the high fluctuations of the rectifier ac power due to PV power injection are not directly reflected on the dc power; the average of the ac power input is exported in the dc link. The remainder of the active power is supported by the rectifier's embedded battery storage. The inverter-side dc power and ac power remains the same and no power is provided by the batteries. The droop controller and the derivative controller

determined the battery power reference in inverter end ancillary services, but the network frequency changes are not high to enable the droop and derivative controllers.

### 5.2.6 Summary on Case Study 2

This case study shows that both regular MMC and MMC-ES can be used for renewable energy power transmission over long distances, and specially through submarine cables. It shows that the loss of a large generation in-feed (loss of PV transmission line) is handled best with high reliability using the MMC-ES. The MMC-ES was able to reduce frequency deviations, ROCOF as well as the possibility of HVDC link tripping (blocking) due to fault identification.

For large-scale transmission projects, construction of communication lines to relay information on instantaneous active power in-feeds in dominant links can prove beneficial. Ancillary services based on frequency of the system (droop and derivative support) are relatively slow and depend highly on the network frequency measurement system. The communication line could help adjust the ancillary response of the MMC-ES more accurately and rapidly to overcome large transients. It was observed that the energy storage elements could be ramped up faster and provide better overall response to the network with the use of a communication line.

Finally it was observed that the energy storage at the converter terminal could help remove the power fluctuations caused in PV power production due to the solar irradiance profile. This has been also studied in case study 1. In this study, a comparison against using regular MMC vs MMC-ES for HVDC transmission has been done.

## 5.3 Summary

In this chapter two case studies were conducted to observe the use of the MMC-ES in renewable generation grid integration. Case study 1 focused on a system with solar PV integration to an ac network and a MMC-ES was used as an independent battery energy storage unit. The study proved that the MMC-ES could operate to improve the power quality of the ac network with highly variable PV power outputs.

Case study 2 concentrated on using MMC-ES as a means of an element in HVDC transmission and ancillary service provider to the local ac network. The study was used to identify the response to a large generation loss, impact of high solar irradiance variation and impact of different control structures. The observations proved that the MMC-ES is capable of operating a HVDC link to transmit large amounts of renewable power over long distance while providing frequency support services to local networks. The final response was highly dependant on the control system and parameters. Thus for specific control objectives, the control parameters need to be selected appropriately.

## Chapter 6

# Contributions, Conclusions, and Future work

### 6.1 Contributions and Conclusions

MMC-ES has become an attractive research topic related to integration of utility-scale energy storage in both ac and dc systems. Being a relatively new converter topology, there has been a gap in appropriate simulation models and converter analysis tools in literature. The main aim of the thesis was to bridge this gap with appropriate simulation models.

This thesis developed a novel averaged-value model (AVM) for the multivalve of the MMC-ES, which simulates the converter in an EMT environment using averaged quantities of the multivalve. The model allows simulation of circulating currents, phase-level and phase arm-level SOC balancing, and general operation of the converter. Dynamic elements are simulated as mathematical operations and a multivalve is represented as a voltage source behind a resistance, thus allowing great reduction in the number of nodes in the EMT

simulation model. It was observed that the developed AVM achieved simulation speed gains exceeding 30 times those of conventional simulation techniques. The AVM simulates the averaged value low-frequency content of the MMC-ES, which does not include the dc-dc converter's switching ripple. This enables EMT simulations at much larger simulation time steps, thus allowing great simulation acceleration.

The equivalent voltage source representation of the multivalve using the AVM allowed to conduct converter analysis using mathematical tools. In-depth analysis of circulating currents and capacitor voltage ripple of the converter were done. This enabled the design of converter parameters analytically based on the operating points of the converter rather than using optimization tools on EMT simulations. Estimation of the capacitor voltage ripple based on analytical methods and EMT simulation methods were compared against experimental prototype observations, which showed great conformity.

The AVM and previously published detailed equivalent model (DEM) both lacked the capability of simulating the converter's blocking state. The blocked mode of operation is vital to the studies related to faults on the system and checking system response following converter protection actions. The thesis presented an upgrade to the existing DEM and AVM to simulate converter blocking with the addition of an IGBT and two diodes, which accurately capture the converter's response both during faults as well as during converter blocking. A slight reduction of simulation speed was observed in the upgraded DEM and AVM models compared to their original forms, but they still offered great simulation speed gains compared to the detailed switching model, which was, hitherto, the only model capable of conducting converter blocking state simulation.

The ability of simulating converter blocking allowed development of a startup sequence for an HVDC link with MMC-ES converters at both ends. Simulation studies proved that

the MMC-ES capacitor charging and controller activation can be done with minimum inrush currents and gradual loading of the system.

A key usage of energy storage in the power systems is for frequency support action and providing load levelling functions to renewable generation schemes. Two case studies were conducted to study the applicability of MMC-ES to provide the above ancillary services. Case study 1 connected the MMC-ES as an independent battery energy storage system close to a solar PV plant. The MMC-ES conditioned its output ac power depending on the PV plant measurements and local frequency measurements. The case study showed that frequency variations caused in a power system due to highly variable solar irradiance profile could be greatly reduced by the MMC-ES acting as an independent battery energy storage unit.

Case study 2 was conducted to study the use of MMC-ES in forming an HVDC link to transmit large-scale solar generation power. The solar PV plant and MMC-ES were physically located distantly apart and converters in both ends improved ac system frequency response. It was observed that MMC-ES could be used more effectively than regular MMC in such systems in handling irradiance variation as well as generation loss due to faults in the system.

The following publications resulted from the work presented in the thesis. The first publication is on the development of AVM and circulating current and capacitor voltage ripple analysis. The experimental prototype verification is also presented in this publication. The second publication presents the improvements to DEM and AVM to simulate converter blocking and converter startup sequence. The third publication presents case study 1, which uses the MMC-ES independently to provide frequency response to a solar PV power injected system.

- N. Herath and S. Filizadeh, “Average-Value Model for a Modular Multilevel Converter With Embedded Storage,” *IEEE Transactions on Energy Conversion*, vol. 36, no. 2, pp. 789–799, Jun. 2021.
- N. Herath and S. Filizadeh, “Improved Average-Value and Detailed Equivalent Models for Modular Multilevel Converters with Embedded Storage,” *IEEE Transactions on Energy Conversion*, pp. 1–1, 2022 (IEEE Early Access)
- N. Herath, S. Filizadeh, and V. Pathirana, “Increasing Dispatchability of a PV Power Plant through Modular Multilevel Converter-Based Embedded Battery Energy Storage (MMC-EBES),” in *Cigre Canada Conference 2020*, Toronto, Canada, Oct. 2020

## 6.2 Recommendations for Future Work

The MMC-ES will likely have a large footprint due to the integration of energy storage. An analysis is required to calculate or estimate the converter’s footprint, converter cost and energy storage amount, depending on the application. This will also allow feasibility studies on projects using MMC-ES over conventional energy storage topologies.

Calculation of the losses in the MMC-ES is one of the most important studies, which needs to be conducted. The DEM and AVM could predict the conduction losses of the converter, but are unable to model and/or simulate the switching losses in the converter. Switching losses account for a major fraction of the converter losses. Converter parameter selection guidelines will require an update with the analysis of the converter’s switching losses.

The dc-dc converter in the MMC-ES includes inductors, which operate at high frequencies while conducting large currents to discharge high amount of energy from the batteries.

The high frequency and the large current could saturate the inductor core. Thus special inductor design tools need to be developed to study on practical utility scale MMC-ES

The possibility of SM battery discharge to a dc fault on the HVDC link could result in semiconductor and battery destruction. The anti-parallel diodes of dc-dc converter conducts current even when the firing pulses are blocked. Detailed simulation and experimental studies need to be conducted to study this effect. Suitable over-current limiting technologies such as fast acting fuses with surge arrestors for dc-dc converter inductors should be studied.

Grid-forming converter controls are also becoming popular with inverter technology. Having the ability to stably connect to weak ac systems makes grid-forming controls increasingly desirable. Studies need to be conducted on HVDC links formed with MMC-ES along with grid-forming control to study the behaviour of the system in response to faults and loss of generation. The developed AVM and DEM could be readily used for such studies.



## References

- [1] A. Qazi, F. Hussain, N. A. Rahim, G. Hardaker, D. Alghazzawi, K. Shaban, and K. Haruna, "Towards Sustainable Energy: A Systematic Review of Renewable Energy Sources, Technologies, and Public Opinions," *IEEE Access*, vol. 7, pp. 63 837–63 851, 2019.
- [2] H. Gu, R. Yan, and T. Saha, "Review of system strength and inertia requirements for the national electricity market of Australia," *CSEE Journal of Power and Energy Systems*, vol. 5, no. 3, pp. 295–305, Sep. 2019.
- [3] S. Vazquez, S. M. Lukic, E. Galvan, L. G. Franquelo, and J. M. Carrasco, "Energy Storage Systems for Transport and Grid Applications," *IEEE Transactions on Industrial Electronics*, vol. 57, no. 12, pp. 3881–3895, Dec. 2010.
- [4] V. A. Boicea, "Energy Storage Technologies: The Past and the Present," *Proceedings of the IEEE*, vol. 102, no. 11, pp. 1777–1794, Nov. 2014.
- [5] N. Miller, D. Lew, and R. Piwko, "Technology capabilities for fast frequency response," GE Energy Consulting, Tech. Rep., Mar. 2017.
- [6] "PCS100 ESS." [Online]. Available: <https://new.abb.com/power-converters-inverters/power-converters-and-inverters/pcs100-ess>
- [7] O. E. Oni, I. E. Davidson, and K. N. Mbangula, "A review of LCC-HVDC and VSC-HVDC technologies and applications," in *2016 IEEE 16th International Conference on Environment and Electrical Engineering (EEEIC)*, Jun. 2016, pp. 1–7.
- [8] Kundur, *Power System Stability And Control*. McGraw-Hill, 1994.
- [9] A. Lesnicar and R. Marquardt, "An innovative modular multilevel converter topology suitable for a wide power range," in *2003 IEEE Bologna Power Tech Conference Proceedings*, vol. 3, Jun. 2003, pp. 6–11.

- 
- [10] I. Serban and C. Marinescu, “Control Strategy of Three-Phase Battery Energy Storage Systems for Frequency Support in Microgrids and with Uninterrupted Supply of Local Loads,” *IEEE Transactions on Power Electronics*, vol. 29, no. 9, pp. 5010–5020, Sep. 2014.
- [11] K. Divya and J. Østergaard, “Battery energy storage technology for power systems—An overview,” *Electric Power Systems Research*, vol. 79, no. 4, pp. 511–520, Apr. 2009.
- [12] J. Rocabert, R. Capó-Misut, R. S. Muñoz-Aguilar, J. I. Candela, and P. Rodriguez, “Control of Energy Storage System Integrating Electrochemical Batteries and Supercapacitors for Grid-Connected Applications,” *IEEE Transactions on Industry Applications*, vol. 55, no. 2, pp. 1853–1862, Mar. 2019.
- [13] S. Nomura, Y. Ohata, T. Hagita, H. Tsutsui, S. Tsuji-Iio, and R. Shimada, “Wind farms linked by SMES systems,” *IEEE Transactions on Applied Superconductivity*, vol. 15, no. 2, pp. 1951–1954, Jun. 2005.
- [14] M. Molina, P. Mercado, and E. Watanabe, “Dynamic Performance of a Static Synchronous Compensator with Superconducting Magnetic Energy Storage,” in *2005 IEEE 36th Power Electronics Specialists Conference*, Jun. 2005, pp. 224–230.
- [15] M. Vasiladiotis and A. Rufer, “Analysis and Control of Modular Multilevel Converters With Integrated Battery Energy Storage,” *IEEE Transactions on Power Electronics*, vol. 30, no. 1, pp. 163–175, Jan. 2015.
- [16] F. Guo, Y. Ye, and R. Sharma, “A modular multilevel converter based battery-ultracapacitor hybrid energy storage system for photovoltaic applications,” in *2015 Clemson University Power Systems Conference (PSC)*, Mar. 2015, pp. 1–6.
- [17] H. Bayat and A. Yazdani, “A Hybrid MMC-Based Photovoltaic and Battery Energy Storage System,” *IEEE Power and Energy Technology Systems Journal*, vol. 6, no. 1, pp. 32–40, Mar. 2019.
- [18] L. Zhang, Y. Tang, S. Yang, and F. Gao, “A modular multilevel converter-based grid-tied battery-supercapacitor hybrid energy storage system with decoupled power control,” in *2016 IEEE 8th International Power Electronics and Motion Control Conference (IPEMC-ECCE Asia)*, May 2016, pp. 2964–2971.
- [19] Q. Chen, R. Li, and X. Cai, “Analysis and Fault Control of Hybrid Modular Multilevel Converter With Integrated Battery Energy Storage System,” *IEEE Journal of Emerging and Selected Topics in Power Electronics*, vol. 5, no. 1, pp. 64–78, Mar. 2017.

- 
- [20] N. Kawakami, S. Ota, H. Kon, S. Konno, H. Akagi, H. Kobayashi, and N. Okada, "Development of a 500-kW Modular Multilevel Cascade Converter for Battery Energy Storage Systems," *IEEE Transactions on Industry Applications*, vol. 50, no. 6, pp. 3902–3910, Nov. 2014.
- [21] T. Soong and P. W. Lehn, "Assessment of Fault Tolerance in Modular Multilevel Converters With Integrated Energy Storage," *IEEE Transactions on Power Electronics*, vol. 31, no. 6, pp. 4085–4095, Jun. 2016.
- [22] N. Herath and S. Filizadeh, "Design and Implementation of a Laboratory Prototype of a Modular Multilevel Converter with Embedded Storage," in *2019 14th Conference on Industrial and Information Systems (ICIIS)*, Dec. 2019, pp. 234–238.
- [23] M. Saeedifard and R. Iravani, "Dynamic Performance of a Modular Multilevel Back-to-Back HVDC System," *IEEE Transactions on Power Delivery*, vol. 25, no. 4, pp. 2903–2912, Oct. 2010.
- [24] S. Debnath, J. Qin, B. Bahrani, M. Saeedifard, and P. Barbosa, "Operation, Control, and Applications of the Modular Multilevel Converter: A Review," *IEEE Transactions on Power Electronics*, vol. 30, no. 1, pp. 37–53, Jan. 2015.
- [25] T. Soong and P. W. Lehn, "Internal Power Flow of a Modular Multilevel Converter With Distributed Energy Resources," *IEEE Journal of Emerging and Selected Topics in Power Electronics*, vol. 2, no. 4, pp. 1127–1138, Dec. 2014.
- [26] R. Mo and H. Li, "Hybrid Energy Storage System With Active Filter Function for Shipboard MVDC System Applications Based on Isolated Modular Multilevel DC/DC Converter," *IEEE J. Emerg. Sel. Topics Power Electron.*, vol. 5, no. 1, pp. 79–87, Mar. 2017.
- [27] R. H. Park, "Two-reaction theory of synchronous machines generalized method of analysis-part I," *Transactions of the American Institute of Electrical Engineers*, vol. 48, no. 3, pp. 716–727, Jul. 1929.
- [28] H. Karimi, A. Yazdani, and R. Iravani, "Negative-Sequence Current Injection for Fast Islanding Detection of a Distributed Resource Unit," *IEEE Transactions on Power Electronics*, vol. 23, no. 1, pp. 298–307, Jan. 2008.
- [29] R. Chakraborty and A. Dey, "Circulating Current Control of Modular Multilevel Converter With Reduced Conduction Loss for Medium-Voltage Applications," *IEEE Transactions on Industrial Electronics*, vol. 68, no. 10, pp. 9014–9023, Oct. 2021.
-

- 
- [30] A. Marzoughi, R. Burgos, D. Boroyevich, and Y. Xue, "Analysis of capacitor voltage ripple minimization in modular multilevel converter based on average model," in *2015 IEEE 16th Workshop on Control and Modeling for Power Electronics (COMPEL)*, Jul. 2015, pp. 1–7.
- [31] Junhong Zhang, Jih-Sheng Lai, and Wensong Yu, "Bidirectional DC-DC converter modeling and unified controller with digital implementation," in *2008 Twenty-Third Annual IEEE Applied Power Electronics Conference and Exposition*, Feb. 2008, pp. 1747–1753.
- [32] N. Mohan, T. M. Undeland, and W. P. Robbins, *Power Electronics: Converters, Applications, and Design*. John Wiley & Sons, 2003.
- [33] H. Saad, S. Denetiere, J. Mahseredjian, P. Delarue, X. Guillaud, J. Peralta, and S. Nguefeu, "Modular Multilevel Converter Models for Electromagnetic Transients," *IEEE Transactions on Power Delivery*, vol. 29, no. 3, pp. 1481–1489, Jun. 2014.
- [34] H. Saad, J. Peralta, S. Denetiere, J. Mahseredjian, J. Jatskevich, J. A. Martinez, A. Davoudi, M. Saeedifard, V. Sood, X. Wang, J. Cano, and A. Mehrizi-Sani, "Dynamic Averaged and Simplified Models for MMC-Based HVDC Transmission Systems," *IEEE Transactions on Power Delivery*, vol. 28, no. 3, pp. 1723–1730, Jul. 2013.
- [35] J. Peralta, H. Saad, S. Denetiere, J. Mahseredjian, and S. Nguefeu, "Detailed and Averaged Models for a 401-Level MMC–HVDC System," *IEEE Transactions on Power Delivery*, vol. 27, no. 3, pp. 1501–1508, Jul. 2012.
- [36] H. W. Dommel, "Digital Computer Solution of Electromagnetic Transients in Single- and Multiphase Networks," *IEEE Transactions on Power Apparatus and Systems*, vol. PAS-88, no. 4, pp. 388–399, Apr. 1969.
- [37] U. N. Gnanarathna, A. M. Gole, and R. P. Jayasinghe, "Efficient Modeling of Modular Multilevel HVDC Converters (MMC) on Electromagnetic Transient Simulation Programs," *IEEE Transactions on Power Delivery*, vol. 26, no. 1, pp. 316–324, Jan. 2011.
- [38] J. Xu, A. M. Gole, and C. Zhao, "The Use of Averaged-Value Model of Modular Multilevel Converter in DC Grid," *IEEE Transactions on Power Delivery*, vol. 30, no. 2, pp. 519–528, Apr. 2015.
- [39] H. Ouquelle, L.-A. Dessaint, and S. Casoria, "An average value model-based design of a deadbeat controller for VSC-HVDC transmission link," in *2009 IEEE Power Energy Society General Meeting*, Jul. 2009, pp. 1–6.
- [40] S. Rodrigues, C. Restrepo, E. Kontos, R. Teixeira Pinto, and P. Bauer, "Trends of offshore wind projects," *Renewable and Sustainable Energy Reviews*, vol. 49, pp. 1114–1135, Sep. 2015.
-

- 
- [41] B. Novakovic and A. Nasiri, "Modular Multilevel Converter for Wind Energy Storage Applications," *IEEE Transactions on Industrial Electronics*, vol. 64, no. 11, pp. 8867–8876, Nov. 2017.
- [42] X. Y. Wang, D. Mahinda Vilathgamuwa, and S. S. Choi, "Determination of Battery Storage Capacity in Energy Buffer for Wind Farm," *IEEE Transactions on Energy Conversion*, vol. 23, no. 3, pp. 868–878, Sep. 2008.
- [43] Y. Liu, W. Du, L. Xiao, H. Wang, and S. Bu, "Sizing Energy Storage Based on a Life-Cycle Saving Dispatch Strategy to Support Frequency Stability of an Isolated System With Wind Farms," *IEEE Access*, vol. 7, pp. 166 329–166 336, 2019.
- [44] Y. V. Makarov, P. Du, M. C. W. Kintner-Meyer, C. Jin, and H. F. Illian, "Sizing Energy Storage to Accommodate High Penetration of Variable Energy Resources," *IEEE Transactions on Sustainable Energy*, vol. 3, no. 1, pp. 34–40, Jan. 2012.
- [45] L. Miao, J. Wen, H. Xie, C. Yue, and W. Lee, "Coordinated Control Strategy of Wind Turbine Generator and Energy Storage Equipment for Frequency Support," *IEEE Transactions on Industry Applications*, vol. 51, no. 4, pp. 2732–2742, Jul. 2015.
- [46] J. Dang, J. Seuss, L. Suneja, and R. G. Harley, "SoC Feedback Control for Wind and ESS Hybrid Power System Frequency Regulation," *IEEE Journal of Emerging and Selected Topics in Power Electronics*, vol. 2, no. 1, pp. 79–86, Mar. 2014.
- [47] G. Delille, B. Francois, and G. Malarange, "Dynamic Frequency Control Support by Energy Storage to Reduce the Impact of Wind and Solar Generation on Isolated Power System's Inertia," *IEEE Transactions on Sustainable Energy*, vol. 3, no. 4, pp. 931–939, Oct. 2012.
- [48] F. Daraiseh, "Frequency response of energy storage systems in grids with high level of wind power penetration – Gotland case study," *IET Renewable Power Generation*, vol. 14, no. 8, pp. 1282–1287, 2020.
- [49] Z. Q. Jiang, Y. Chen, X. Zhou, and J. X. Jin, "Investigation of solar thermal power technology," in *2011 International Conference on Applied Superconductivity and Electromagnetic Devices*, Dec. 2011, pp. 275–281.
- [50] V. Azevêdo, A. Candeias, and C. Tiba, "Location Study of Solar Thermal Power Plant in the State of Pernambuco Using Geoprocessing Technologies and Multiple-Criteria Analysis," *Energies*, vol. 10, no. 7, p. 1042, Jul. 2017.
- [51] H. Bayat and A. Yazdani, "A Power Mismatch Elimination Strategy for an MMC-Based Photovoltaic System," *IEEE Transactions on Energy Conversion*, vol. 33, no. 3, pp. 1519–1528, Sep. 2018.
-

- [52] S. Rivera, B. Wu, R. Lizana, S. Kouro, M. Perez, and J. Rodriguez, “Modular multilevel converter for large-scale multistring photovoltaic energy conversion system,” in *2013 IEEE Energy Conversion Congress and Exposition*, Sep. 2013, pp. 1941–1946.
- [53] M. A. Perez, D. Arancibia, S. Kouro, and J. Rodriguez, “Modular multilevel converter with integrated storage for solar photovoltaic applications,” in *IECON 2013 - 39th Annual Conference of the IEEE Industrial Electronics Society*, Nov. 2013, pp. 6993–6998.
- [54] F. Rong, X. Gong, and S. Huang, “A Novel Grid-Connected PV System Based on MMC to Get the Maximum Power Under Partial Shading Conditions,” *IEEE Transactions on Power Electronics*, vol. 32, no. 6, pp. 4320–4333, Jun. 2017.
- [55] J. Kraft, “On the Grounding and Bonding of Solar Photovoltaic Systems - IAEI Magazine,” Jan. 2021. [Online]. Available: <https://www.iaei.org/page/2021-01-grounding-and-bonding-solar-photovoltaic-systems>
- [56] J. A. del Cueto and S. R. Rummel, “Degradation of photovoltaic modules under high voltage stress in the field,” in *SPIE Solar Energy + Technology*, N. G. Dhere, J. H. Wohlgemuth, and K. Lynn, Eds., San Diego, California, Aug. 2010, p. 77730J.
- [57] R. H. Lasseter, Z. Chen, and D. Pattabiraman, “Grid-Forming Inverters: A Critical Asset for the Power Grid,” *IEEE J. Emerg. Sel. Topics Power Electron.*, vol. 8, no. 2, pp. 925–935, Jun. 2020.
- [58] N. Herath, S. Filizadeh, and M. S. Toulabi, “Modeling of a Modular Multilevel Converter With Embedded Energy Storage for Electromagnetic Transient Simulations,” *IEEE Transactions on Energy Conversion*, vol. 34, no. 4, pp. 2096–2105, Dec. 2019.
- [59] K. Ilves, A. Antonopoulos, S. Norrga, and H.-P. Nee, “Steady-State Analysis of Interaction Between Harmonic Components of Arm and Line Quantities of Modular Multilevel Converters,” *IEEE Transactions on Power Electronics*, vol. 27, no. 1, pp. 57–68, Jan. 2012.
- [60] S. Arunprasanth, U. D. Annakkage, C. Karawita, and R. Kuffel, “Generalized Frequency-Domain Controller Tuning Procedure for VSC Systems,” *IEEE Transactions on Power Delivery*, vol. 31, no. 2, pp. 732–742, Apr. 2016.
- [61] D. M. Rosewater, D. A. Copp, T. A. Nguyen, R. H. Byrne, and S. Santoso, “Battery Energy Storage Models for Optimal Control,” *IEEE Access*, vol. 7, pp. 178 357–178 391, 2019.

- 
- [62] N. Herath and S. Filizadeh, "Average-Value Model for a Modular Multilevel Converter With Embedded Storage," *IEEE Transactions on Energy Conversion*, vol. 36, no. 2, pp. 789–799, Jun. 2021.
- [63] K. Sharifabadi, L. Harnefors, H.-P. Nee, S. Norrga, and R. Teodorescu, *Design, Control, and Application of Modular Multilevel Converters for HVDC Transmission Systems*. Wiley-IEEE Press, 2016.
- [64] J. Alonso, S. Howell, and K. Abdel-Hadi, "Half-Bridge and H-Bridge Equivalent MMC Models for EMT Simulation," in *International Conference on Power Systems Transients (IPST 2019)*, Perpignan, France, Jun. 2019.
- [65] S. Howell, S. Filizadeh, and A. M. Gole, "Unidirectional HVdc Topology With DC Fault Ride-Through Capability," *Canadian Journal of Electrical and Computer Engineering*, vol. 40, no. 1, pp. 41–49, 2017.
- [66] N. Herath, M. Toulabi, and S. Filizadeh, "Control and operation of a modular multilevel converter with embedded battery energy storage," in *CIGRE Canada Conference 2018*, Calgary, AB, Canada, Oct. 2018.
- [67] O. Tremblay, L.-A. Dessaint, and A.-I. Dekkiche, "A Generic Battery Model for the Dynamic Simulation of Hybrid Electric Vehicles," in *2007 IEEE Vehicle Power and Propulsion Conference*, Sep. 2007, pp. 284–289.
- [68] H. Zhao, S. Fan, and A. M. Gole, "Stability Evaluation of Interpolation, Extrapolation, and Numerical Oscillation Damping Methods Applied in EMT Simulation of Power Networks with Switching Transients," *IEEE Transactions on Power Delivery*, pp. 1–1, 2020.
- [69] N. Herath and S. Filizadeh, "Improved Average-Value and Detailed Equivalent Models for Modular Multilevel Converters with Embedded Storage," *IEEE Transactions on Energy Conversion*, pp. 1–1, 2022.
- [70] H. Huang, J. Xu, Z. Peng, S. Yoo, D. Yu, D. Huang, and H. Qin, "Cloud motion estimation for short term solar irradiation prediction," in *2013 IEEE International Conference on Smart Grid Communications (SmartGridComm)*, Oct. 2013, pp. 696–701.
- [71] K. Y. Bae, H. S. Jang, and D. K. Sung, "Hourly Solar Irradiance Prediction Based on Support Vector Machine and Its Error Analysis," *IEEE Transactions on Power Systems*, vol. 32, no. 2, pp. 935–945, Mar. 2017.
- [72] H. Xin, Y. Liu, Z. Wang, D. Gan, and T. Yang, "A new frequency regulation strategy for photovoltaic systems without energy storage," *IEEE Trans. Sustain. Energy*, vol. 4, no. 4, pp. 985–993, Oct. 2013.

- [73] A. F. Hoke, M. Shirazi, S. Chakraborty, E. Muljadi, and D. Maksimovic, “Rapid Active Power Control of Photovoltaic Systems for Grid Frequency Support,” *IEEE Journal of Emerging and Selected Topics in Power Electronics*, vol. 5, no. 3, pp. 1154–1163, Sep. 2017.
- [74] G. Wang, M. Ciobotaru, and V. G. Agelidis, “Power Smoothing of Large Solar PV Plant Using Hybrid Energy Storage,” *IEEE Transactions on Sustainable Energy*, vol. 5, no. 3, pp. 834–842, Jul. 2014.
- [75] J. C. Hernández, P. G. Bueno, and F. Sanchez-Sutil, “Enhanced utility-scale photovoltaic units with frequency support functions and dynamic grid support for transmission systems,” *IET Renewable Power Generation*, vol. 11, no. 3, pp. 361–372, 2017.
- [76] “High-Resolution Solar Radiation Datasets — Natural Resources Canada.” [Online]. Available: <https://www.nrcan.gc.ca/energy/renewable-electricity/solar-photovoltaic/18409>
- [77] N. Herath, S. Filizadeh, and V. Pathirana, “Increasing Dispatchability of a PV Power Plant through Modular Multilevel Converter-Based Embedded Battery Energy Storage (MMC-EBES),” in *Cigre Canada Conference 2020*, Toronto, Canada, Oct. 2020.
- [78] I. Vairavasundaram, V. Varadarajan, P. J. Pavankumar, R. K. Kanagavel, L. Ravi, and S. Vairavasundaram, “A Review on Small Power Rating PV Inverter Topologies and Smart PV Inverters,” *Electronics*, vol. 10, no. 11, p. 1296, May 2021.
- [79] “Central Inverters — Fimer Spa.” [Online]. Available: <https://www.fimer.com/products-and-services/solar/central-inverters>
- [80] *Grid Integration of Wind Energy*, 1st ed. John Wiley & Sons, Ltd, 2014.
- [81] “Sun Cable — The World’s Largest Solar Energy Infrastructure Project.” [Online]. Available: <https://suncable.sg/>
- [82] “Viking Link Interconnector.” [Online]. Available: <https://viking-link.com/>
- [83] H. Brakelmann and J. Stammen, “Thermal Emissions of the Submarine Cable Installation Viking Link in the German AWZ,” Rheinberg und Neukirchen-Vluyn., Tech. Rep., Jan. 2017.
- [84] “IEEE Application Guide for IEEE Std 1547(TM), IEEE Standard for Interconnecting Distributed Resources with Electric Power Systems,” *IEEE Std 1547.2-2008*, pp. 1–217, Apr. 2009.